January 2019

Jet Geometry Engineering Via Di-Jet Imbalance Measurements At Rhic In Star

Nicholas Elsey
Wayne State University

JET GEOMETRY ENGINEERING VIA DI-JET IMBALANCE MEASUREMENTS AT RHIC IN STAR

by

NICHOLAS ELSEY

DISSERTATION

Submitted to the Graduate School

of Wayne State University,

Detroit, Michigan

in partial fulfillment of the requirements

for the degree of

DOCTOR OF PHILOSOPHY

2019

MAJOR: Physics

Approved By:

_____

Advisor Date

_____

_____

_____

DEDICATION

To my mother

You always believed I could touch the stars,

even when I couldn't look up from the ground.

I miss you, mom.

ACKNOWLEDGMENTS

We've been told it takes a village to raise a child, but I've also learned it takes a community to make a doctorate. There are far too many people who have helped along the way to name them all; but to all of my friends, members of the STAR collaboration, and Wayne State professors, post docs, and students, I thank you.

I would like to specially thank my advisor, Joern Putschke, for his patience, steady guidance and mentorship; I owe him a great deal of gratitude for working with me and helping me become a better scientist. I would also like to thank the members of my committee: Abhijit Majumder, Sergei Voloshin and Matthew Allen, all of whom have made significant impacts on my time at Wayne State, beyond being members of my committee. I would like to thank all of the current and past members of the heavy-ion group in the physics department, including Claude Pruneau, Bill Llope, Jinjin Pan, Moe Saleh, Ron Belmont, Prabhat Pujahari, Rosi Reed, Takafumi Niida, Ayeh Jowzaee, and especially Raghav Kunnawalkam Elayavalli, Isaac Mooney and Veronica Verkest. And I of course could never have done all of this without the support of my family, especially my parents, Patricia and Keith Elsey, and my sister Rachel Elsey.

Finally, there are two people who deserve a great deal of gratitude. First, Kolja Kauder; when I joined the group, I did not have a senior student to learn from. Kolja stepped in and taught me most of what I know about the STAR collaboration, how the physics community works, and quite a bit of how to enjoy the Ph.D. life. He is a great friend, and I consider myself lucky to have worked with him here at Wayne State. Lastly, I thank my girlfriend Danning Wang. We started dating the semester after I started the program, and she has been there supporting me for the full five years. Many parts of the program were lonely; but they were less lonely when I could share them with her. Many times I felt inadequate, but she lifted my spirits. I am extremely lucky to have you in my life, Dani, and I thank you from the bottom of my heart.

$\sim$ *Nick Elsey*

TABLE OF CONTENTS

LIST OF TABLES

LIST OF FIGURES

1 INTRODUCTION

"It's a dangerous business, Frodo, going out your door. You step onto the road, and if you don't keep your feet, there's no knowing where you might be swept off to."

– J.R.R Tolkien, *The Lord of the Rings*

Since before the ancient Greeks, philosophers and scientists have endeavored to understand the structure of the world around us. Our understanding has evolved from simple theories of matter, believing the world to be made of composites of fire, earth, wind, and water based on philosophical arguments, to the current state of the art - the Standard Model of particle physics, based on experimental evidence and the scientific method. In its current state, as shown in Figure 1.1, the Standard Model consists of only six quarks, six leptons, their anti-particles, the Higgs field, and the four forces. Each force is believed to be mediated by a boson: gravity by the still theoretical graviton, electromagnetism by the photon, the weak nuclear force by the W and Z bosons, and the strong nuclear force by the gluon. The model has been extremely successful at predicting the subatomic dynamics of the universe, including the existence of W and Z bosons, the gluon, and the top and charm quarks before their experimental discovery. However, the model may not be complete, with many questions, such as the existence of a graviton still unanswered. Furthermore, there is evidence that only five percent of the total mass/energy of the universe is described by the Standard Model - the rest has been labeled as dark energy and dark matter, which has never been directly measured and is not predicted by the Standard Model.

While the Higgs field gives mass to the quarks and leptons, over 99% of the mass of the proton and neutron (nucleons), and thus the majority of the mass of the observable universe, is derived from the kinetic energy of the quarks and the binding energy of the gluons inside the nucleon. The study of nuclear physics is the study of the structure and properties of the proton and neutron, the nuclei that they form, and of their constituents, the quarks and gluons (partons). In high-energy nuclear physics, we attempt to observe the properties

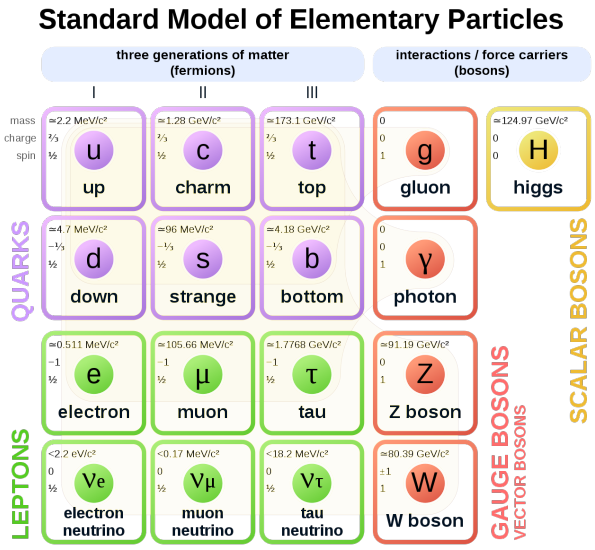

Figure 1.1: The Standard Model in its current form. Image from en.wikipedia.org/wiki/Standard_Model.

of the gluon in extremely high temperature and energy regimes in an effort to understand the force that binds the quarks into nucleons, and nucleons into nuclei. To produce the enormous temperatures and densities required to observe the dynamics of partons in the lab, ultra-relativistic heavy-ion collisions are produced at the largest particle accelerators on the planet. In every collision, the extreme energy and density produces a state of matter that has not existed naturally in the universe since a few milliseconds after the Big Bang: a plasma of quarks and gluons.

1.1 Quantum Chromodynamics (QCD)

The primary force of interest for this work is the strong nuclear interaction, mediated by the gluon, described theoretically by quantum chromodynamics (QCD). The gluon couples to color charge, but also carries color charge itself; it is because of this color charge that gluons are free to interact with other gluons as well as with quarks. This is the key feature that distinguishes QCD from the electroweak interactions, and makes it a non-abelian gauge theory. QCD, due to its non-abelian nature, has a negative β function - meaning its coupling constant (α_s), which is a measure of the strength of the interaction, runs from large values

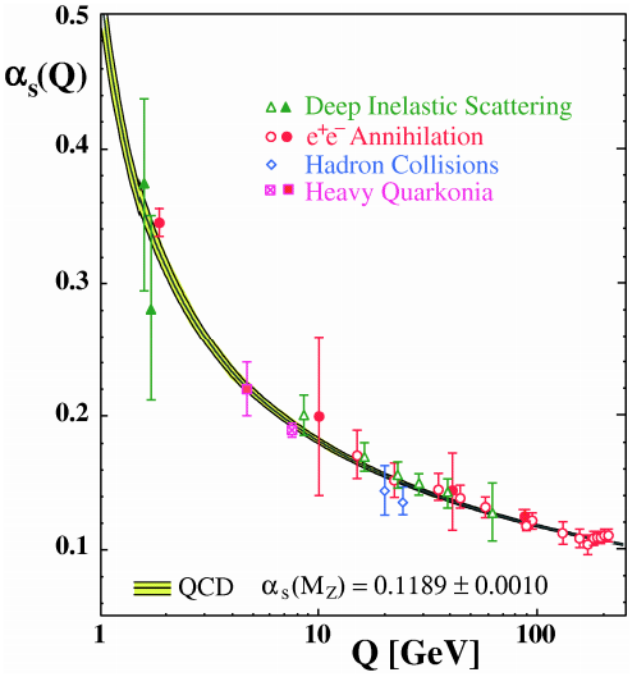

Figure 1.2: Experimental evidence of the running coupling of α_s, as measured by multiple experimental setups [1].

at low energies, to small values at high energies, as shown in Figure 1.2 [1].

Due to its self-interacting mediators and running coupling, QCD has two properties not seen in the other forces - confinement and asymptotic freedom [2, 3].

Asymptotic freedom: In the high-Q^2 (momentum transfer) regime (probing small length scales), α_s becomes small, and quarks and gluons interact very weakly, behaving as free particles [4].

Confinement: The force between quarks does not diminish as they are separated in space, due to the polarized vacuum. In other words, when probing colored objects with low-Q^2 probes, α_s appears large. Thus, it is impossible to separate and stabilize a single color charge. Because of this, all stable QCD states found in nature are color singlets such as mesons ($q\bar{q}$) or baryons (qqq or $\bar{q}\bar{q}\bar{q}$).

Due to its non-abelian nature and strong coupling, QCD can be hard or impossible to solve analytically using the same techniques developed for the electroweak theory in

many regimes. For instance, perturbative methods cannot be used to study the dynamics of hadronic matter at room temperature and density, because $\alpha_s > 1$. In these non-perturbative regimes, it has been shown that discretization of space and time onto a lattice naturally regularizes the theory, and allows physically meaningful quantities to be extracted by extrapolating the result to an infinitely large and dense lattice. This technique is called lattice QCD (LQCD) and has been shown to accurately predict, amongst other observables, the masses of many hadronic bound states [5, 6].

1.1.1 The Quark-Gluon Plasma

Much like how normal (atomic) matter can exist in multiple states (liquid, solid, etc) depending on temperature or pressure, it was proposed that hadronic matter in systems with sufficiently high temperature and baryonic density would no longer be bound into colorless mesons and baryons, as shown in Figure 1.3. In such a regime, the density of color charges would be so great that they shield any long-range interactions, producing a plasma of quasi-free partons where the coupling of the strong nuclear force is suppressed, known as the quark-gluon plasma (QGP). We know now that at temperatures and densities achieved by current experiments, the partons still have significant strong force interactions. While signatures of deconfinement, and thus the QGP are present, the produced plasma appears to behave more like an ideal liquid than an ideal gas, as discussed in Chapter 2.

The phase transition between hadronic and partonic matter happens in the low-Q^2, non-perturbative regime, and is studied using methods such as LQCD. Lattice calculations have shown the existence of a critical temperature T_c, above which the energy density divided by temperature to the fourth power (ϵ/T^4) increases significantly [8], as seen in Figure 1.4. This sharp change in the energy density implies a large increase in the relevant degrees of freedom of the system. This has been interpreted as the threshold at which the relevant degrees of freedom are no longer bound hadronic states, but are instead the free partons. However, it is seen in these lattice calculations that the values of ϵ/T^4 are still significantly below the Stefan-Boltzmann limit of the ideal gas. Therefore, at temperatures accessible to

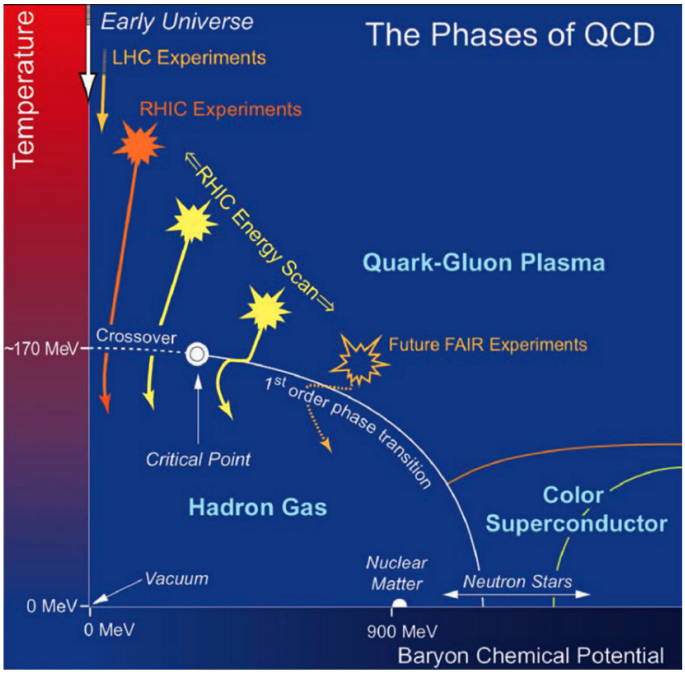

Figure 1.3: Sketch of the QCD phase diagram, predicting some of the complexity of hadronic matter [7].

current experiments, the lattice predicts quasi-free partons but with sizable non-perturbative interactions.

1.1.2 Jets and Perturbative QCD

Low-Q^2 processes can be numerically estimated via techniques such as LQCD. Processes with a sufficiently high momentum transfer, and thus a small α_s, such as high energy hard scatterings between partons, however, are calculable using traditional field theory techniques - namely, perturbative expansions. These hard scatterings produce back-to-back pairs of high energy partons, which recoil, fragment, and hadronize into collimated sprays of energetic hadrons, called jets. Perturbative QCD (pQCD) allows the analytical calculation of these purely short-range (high energy) processes.

The majority of measured observables, however, are not purely short-range processes, but are convolutions of physical processes that occur at many different energy scales. This would lead to the loss of any applicability of pQCD for the calculation of these processes, if the short-range and long-range processes had any significant interference. Intuitively, it

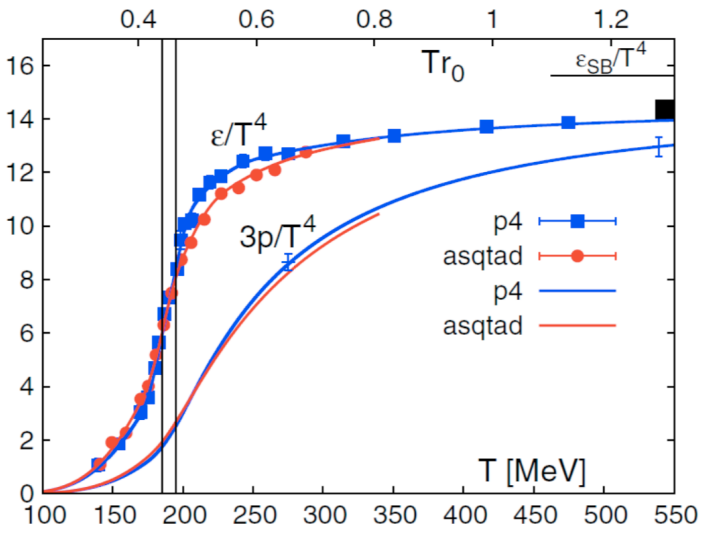

Figure 1.4: ϵ/T^4 as a function of temperature for hadronic matter from lattice calculations. The large inflection point shows the critical temperature of QCD [8].

would seem that processes on very different scales would not interfere - much like quantum mechanics and Newtonian mechanics - if the length-scales of interest were separated enough. This separation of scales would allow the calculation to be *factorized* into the product of short-range processes amenable to pQCD and long-range processes that would have to be extracted from experiment or calculated some other way.

The ability to perform this factorization has only been proven rigorously for a handful of processes, but comparison to experiment shows that calculations involving factorization are applicable in many cases where such proofs do not yet exist. For instance, calculations are found to describe the jet production cross section in both e^+e^- and $p+p$ collisions with high accuracy over many orders of magnitude [9], as shown in Figure 1.5, along with many other jet and high-Q^2 observables, over a large range of collision energies.

The calculation of the jet cross section in $p+p$ collisions relies on the factorization of the jet production into the parton distribution function (PDF) and the hard scattering. The PDF is a probability distribution of finding a specific parton species within a nucleon with a given fraction of the proton's longitudinal momentum (denoted $x = \frac{Q^2}{2P\cdot q}$, where Q

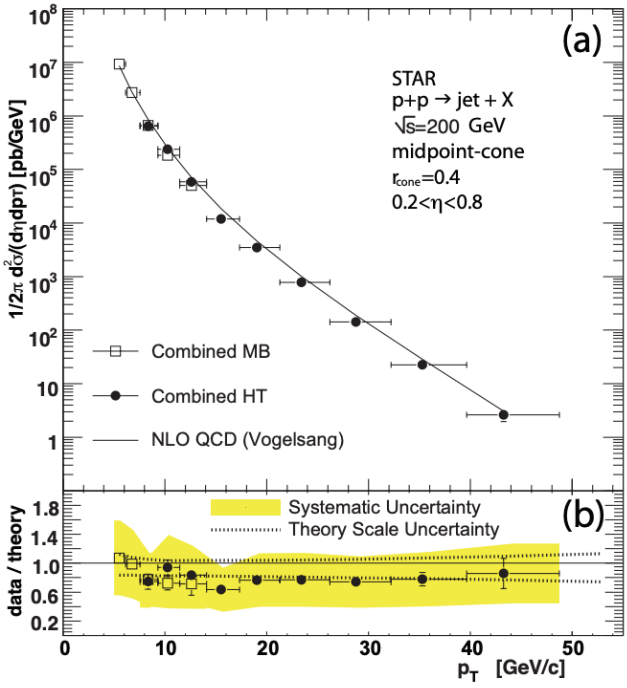

Figure 1.5: Inclusive jet cross section measured at STAR (data points) compared to model calculation. Agreement within systematic uncertainties over seven orders of magnitude [9].

is the energy scale of the interaction, P is the proton's momentum and q is the parton's momentum). Because of factorization, these PDFs are *universal* - they do not depend on the process being measured. PDFs measured in deep inelastic scattering (DIS) work equally well for $p+p$ and Au+Au collisions. Furthermore, these PDFs can be evolved from one Q^2 to another using DGLAP evolution equations [10–12]:

$$\mu \frac{d}{d\mu} f_i(x,\mu) = \frac{\alpha_s}{\pi} \int_x^1 \frac{d\xi}{\xi} f(\xi,\mu) P_{qq}(\frac{x}{\xi}) \tag{1.1}$$

$$P_{qq}(z) = C_F \left[(1+z^2) \left[\frac{1}{1-z} \right]_+ + \frac{3}{2} \delta(1-z) \right], \tag{1.2}$$

where equation 1.1 is the DGLAP evolution equation and equation 1.2 is the DGLAP splitting function.

By combining these universal PDFs and pQCD calculations, hard processes such as jet

production that are well understood in $p+p$ and $e^+ + e^-$ collisions can be used as probes to measure the properties of the QGP. How such measurements can be made will be explored in Chapters 2 & 3.

1.2 Overview

In this thesis, we will discuss two analyses of jets in heavy-ion collisions: di-jet hadron correlations and differential di-jet imbalance measurements. Chapter 2 will introduce relevant information about heavy-ion collisions, and how jets can be used to probe the structure and properties of the QGP. An introduction to jetfinding is given in Chapter 3, and the experimental facilities will be introduced in Chapter 4. Chapter 5 will introduce the analyzed data. The di-jet hadron correlations and differential di-jet imbalance measurements will be presented in Chapters 6 and 7, respectively. Finally, conclusions and a summary will be presented in chapter 8.

2 HEAVY-ION COLLISIONS

"He that breaks a thing to find out what it is has left the path of wisdom."

– J.R.R. Tolkien, *The Lord of the Rings*

As alluded to in Chapter 1, a current state-of-the-art experimental method for studying the properties of systems of deconfined partons is heavy-ion collisions. These collisions are produced at accelerator complexes such as the Relativistic Heavy Ion Collider (RHIC) located at Brookhaven National Laboratory (BNL), and the Large Hadron Collider (LHC), located at CERN. While the actual temperature and density at which deconfinement occurs is still not known, predictions have been made from lattice calculations, estimating the critical temperature around 170 MeV, for example, assuming $\mu_B \approx 0$ [13]. There is compelling evidence that we have reached high enough temperatures, possibly as early as the 1980s with the Super Proton Synchrotron (SPS) [14], and almost certainly with the advent of RHIC [15–18].

We will begin with an overview of the most important bulk properties in a heavy-ion collision, such as system size and evolution. Using this knowledge, we will then introduce jets as calibrated probes of the medium, and highlight some classic jet observables that have allowed us to quantify the properties of the QGP.

2.1 Bulk anatomy of a heavy-ion collision

Ultra-relativistic heavy-ion collisions evolve through several distinct phases. Pre-collision, the nuclei are traveling near the speed of light, and are heavily Lorentz-contracted. For instance, at the top energy for nuclei at RHIC (100 GeV per nucleon), each ion is circling the ring at 99.995% the speed of light, which leads to a gamma factor of approximately 100.

We will first discuss the effect of the initial state geometry on the collision, before giving an overview of the evolution of the collision from initial interaction to the final-state, which is then detected in the various experiments.

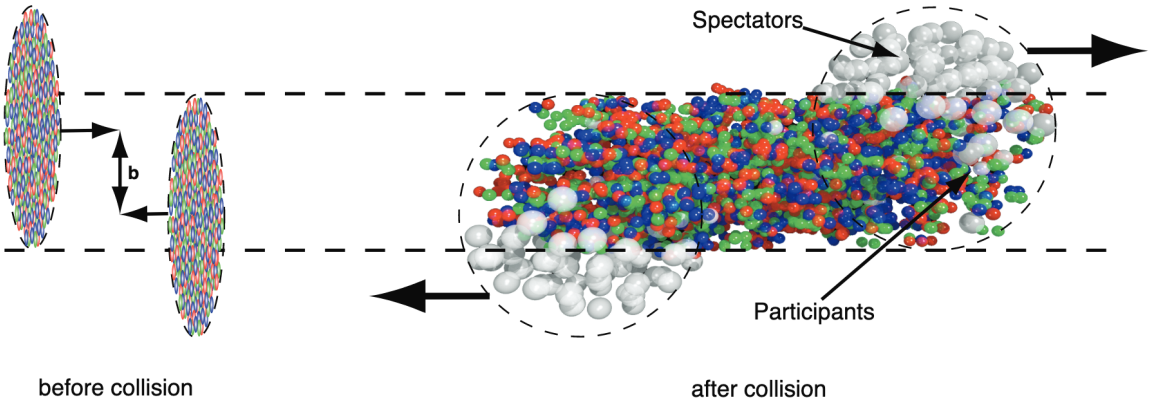

Figure 2.1: Illustration of the impact parameter of a collision [19].

2.1.1 Centrality

Due to the extended size of a large nucleus, collisions between ions can vary significantly based on the impact parameter (b), the transverse distance between the centers of the two nuclei along their relative trajectory, as shown in Figure 2.1. In a head-on collision, $b \approx 0$, whereas for a grazing collision $b \approx r_{\mathrm{A}} + r_{\mathrm{B}}$, where r is the radius of the respective nucleus. Because the properties of collisions such as shape, size, and energy density are quantitively different between small and large b collisions, events are categorized by their "centrality", where collisions with small b are "central" collisions and collisions with large b are called "peripheral". The centrality is generally defined by fractions of the total cross section, where "0-10% most central" collisions correspond to the 10% of events with the smallest impact parameter, and so on. The impact parameter, however, cannot be measured experimentally. Instead, the centrality of a collision is inferred via secondary observables that are monotonically correlated with the impact parameter, such as the multiplicity of produced final-state particles measured in a detector.

2.1.2 Geometry

Many observables of interest in heavy-ion collisions are sensitive to the shape and density of the QGP, which are determined by the geometry of the nucleons which interact during the

collision, called the "participants", or "wounded nucleons" as shown in Figure 2.1. Those nucleons that do not participate are called spectators. Both the average shape and energy density of heavy-ion collisions both change as a function of the impact parameter. The participant distribution of the most central events tends to be spherical, and also leads to the highest initial energy density, as the number of nucleon-nucleon interactions per unit area is highest. More peripheral collisions, however, tend to have a more elliptical participant distribution (imagine the overlap region of a Venn diagram), and the initial energy density tends to be lower.

Due to the non-trivial fluctuations in the initial state of the collision driven by the random distribution of nucleons inside each nucleus on an event-by-event basis, knowledge of the impact parameter (or centrality) alone is not sufficient to infer quantities such as $N_{\text{participants}}$, $N_{\text{binary collisions}}$, or the energy density ϵ. Instead, so-called Glauber models are used to predict these quantities [20,21]. These models were pioneered by Roy Glauber [22,23], and rely on the assumption that at high energies, participant nucleons are undeflected as they pass through the target nucleus, and thus interact with each target nucleon on their straight-line trajectory. This simplifying assumption allows for fast analytical calculation or Monte Carlo simulation of quantities such as $N_{\text{participants}}$ using only two inputs: the inelastic nucleon-nucleon cross section, and the nucleon density distribution. A discussion of Glauber models can be found in Appendix D, and a more thorough review can be found in the references [24].

Heavy ion collisions can further be characterized with a "reaction plane", which is the plane defined by $\vec{b}$ (now a vector in the transverse plane of the collision) and the relative incident trajectory (the beam line in a collider). However, due to the initial state fluctuations of the incident nuclei described above, the reaction plane and the impact parameter do not fully specify the initial state geometry of a particular collision. For this reason, "participant planes" are defined [25, 26], where the n^{th} order participant plane is defined by the n^{th} order axis of symmetry of the participant distribution in the transverse plane. For instance, in a

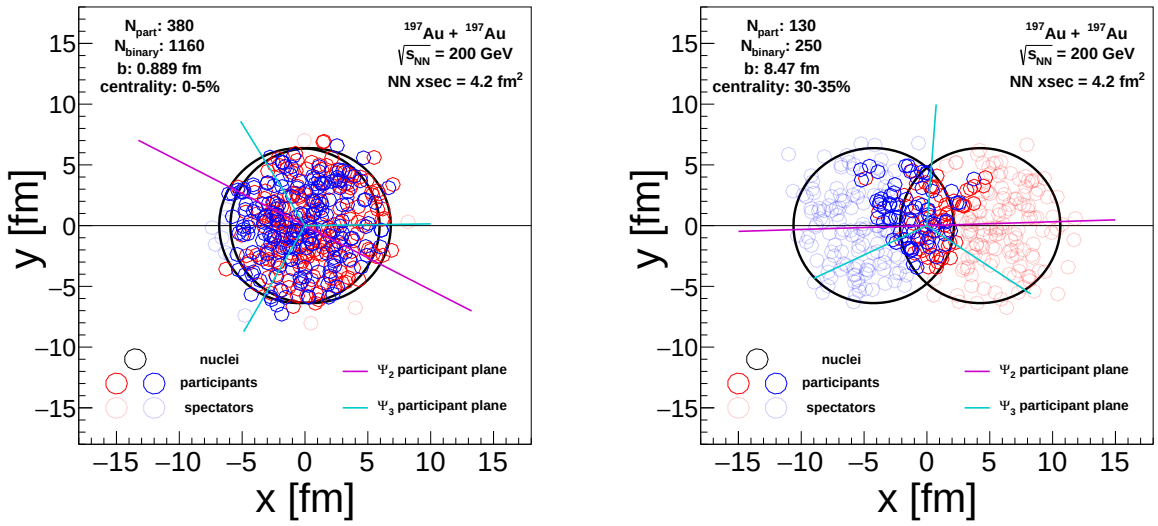

Figure 2.2: Illustration of the collision geometry for single Au+Au events based on a Monte Carlo Glauber model for varying centralities. Left: A very central event. The overlap region is approximately spherical. Right: A mid-central event. The overlap region is approximately elliptical with a significant triangular shape due to fluctuations in the nucleon distributions in each nucleus.

mid-central collision, where the overlap region is elliptical on average, the minor axis of the ellipse defines the 2$^{\text{nd}}$-order participant plane, which is tightly correlated with the reaction plane. The 3$^{\text{rd}}$-order participant plane, however, is generated from fluctuations in the nucleon distribution, and is uncorrelated with either the reaction plane or the 2$^{\text{nd}}$-order participant plane [27]. Because the reaction and participant planes are defined by the incident nuclei and the participant distribution and are thus unmeasurable, the correlated observables called the n^{th}-order "event planes" are reconstructed from the final-state particles measured in an experiment, which are important in the measurement of anisotropic flow, as discussed in Section 2.1.4.

2.1.3 Collision and energy deposition

In heavy-ion collisions in the ultra-relativistic regime, the inter-penetration time (the amount of time the nuclei spend interacting with each other), is only on the order of $2Rc/\gamma \approx 0.1$ fm/c, where R is the nuclear radius. At RHIC energies, this is approximately 10^{-25} s,

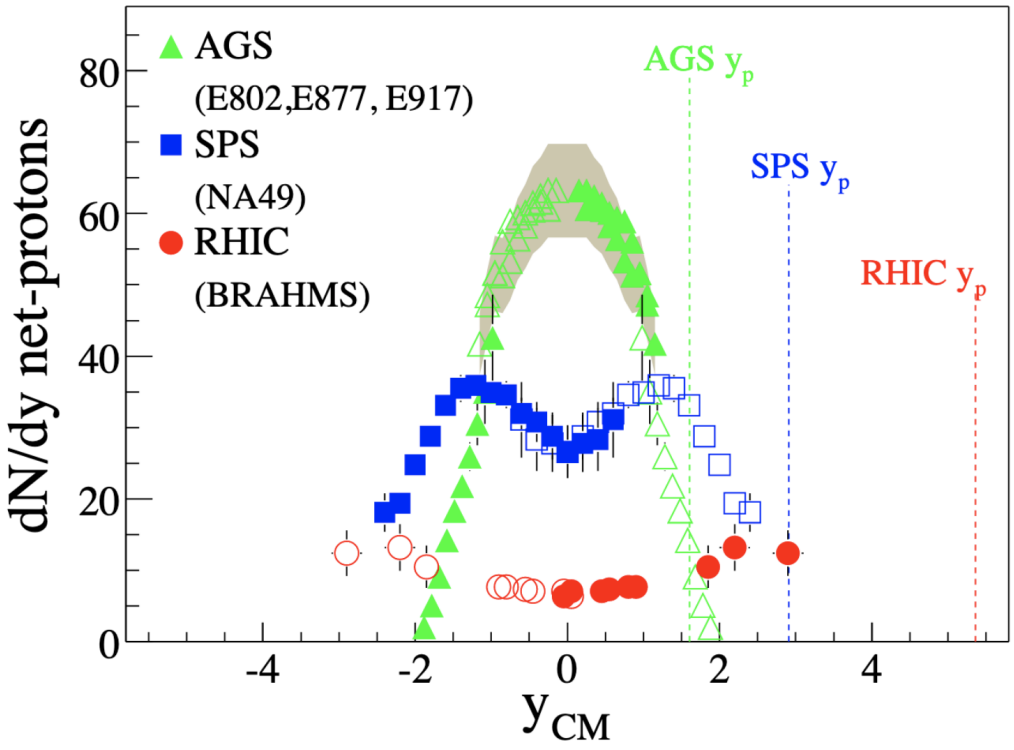

Figure 2.3: Rapidity distribution of nucleons at varying center-of-mass collision energies [28].

a vanishingly small amount of time. During collisions at such high energies, the nucleons are mostly transparent to each other. Most of the incident nucleons are not transported to mid-rapidity (for a definition of rapidity, see Appendix A), as shown in Figure 2.3, which shows the rapidity distribution of net protons as a function of center-of-mass energy, where we see that at RHIC energies the majority of beam nucleons end up at forward rapidity.

However, even with these caveats, a large amount of energy is deposited in the participant region when the nuclei overlap and interact. The Bjorken energy density [29], defined as

$$\epsilon_{Bj} = \frac{1}{A_{\mathrm{T}}\tau}\frac{\mathrm{d}E_{\mathrm{T}}}{\mathrm{d}y}, \tag{2.1}$$

where A_T is the transverse area of the participant region and τ is the formation time, gives an estimate of the energy deposited during a collision. Calculations of the Bjorken energy density at RHIC energies suggest the energy density can approach or exceed 5

GeV/fm^2/c [30], much larger than the energy density of normal hadronic matter ($\epsilon \approx 0.15$ GeV/fm^3), and significantly above predictions of the critical energy density required for QGP formation, generally on the order of 1 GeV/fm^3 [31]. This energy deposition results in a high temperature excitation of the QCD vacuum, which creates thousands of gluons.

2.1.4 System evolution and hydrodynamics

The initial system of produced partons is, in general, not in thermal equilibrium. However, there is good evidence that the system achieves equilibrium at some early time τ_0. This assumption is supported by the success of models that are based on thermal equilibrium, by statistical models of final-state particle yields, and generally by the success of hydrodynamic models at reproducing multiple differential measurements.

After this time τ_0, when the system has reached thermal equilibrium, the expansion of the system is modeled using hydrodynamics. For the case of ideal hydrodynamics, this consists of two constraint equations - conservation of the energy-momentum tensor, and conservation of baryon number, as written here:

$$\partial_\mu \langle T^{\mu\nu} \rangle = 0, \quad \partial_\mu \langle j_B^\mu \rangle = 0. \tag{2.2}$$

For the case of non-ideal hydro, other information is needed, such as the transport coefficients related to heat conduction, as well as the bulk and shear viscosity. The other input that is needed is the equation of state (EOS), which, in many cases, is extracted from lattice calculations. A detailed review of ideal and non-ideal hydrodynamics can be found in the references [32–34].

The ability of ideal hydrodynamics to reproduce experimental results has lead to the general acceptance that the shear viscosity (η/s) is very small, close to the AdS/CFT lower limit of $1/4\pi$ - from which the QGP has earned the monicker “the perfect fluid”.

Radial flow

The QGP system formed in heavy-ion collisions experiences very strong radial expansion. Compelling evidence for this is that multiple particle spectra can be fit with a common temperature when all are boosted by a common, significant radial velocity [35].

Anisotropic flow

In heavy-ion collisions, as described in Section 2.1.2, the shape of the participant region is, in general, non-spherical and fluctuates event-by-event. This spatial anisotropy can be transferred into a momentum space anisotropy due to variations in the pressure gradients, where the greatest acceleration is experienced by particles or fluid cells along the minor axis of the ellipse (or more generally, along the n participant planes).

The azimuthal anisotropy of the spectra resulting from these asymmetric pressure gradients can be characterized by their Fourier coefficients [36], $v_n(p_{\mathrm{T}})$, from the expansion

$$E\frac{d^3N}{d^3p} = \frac{1}{2\pi}\frac{d^2N}{p_{\mathrm{T}}dp_{\mathrm{T}}dy}(1 + \sum_{n=1}^{\infty} 2v_n \cos(n(\phi - \Psi_r))), \tag{2.3}$$

where Ψ_r is the reaction plane angle, and each coefficient is defined by

$$v_n(p_{\mathrm{T}}, y) = \langle \cos(n(\phi - \Psi_r)) \rangle, \tag{2.4}$$

averaged over all particles in the given p_{T}, y window. Because the reaction plane is not directly measurable, other methods have been defined, such as using the event planes, as discussed in Section 2.1.2 [37].

In non-central collisions, the largest term is in general $v_2(p_{\mathrm{T}})$, which is called the elliptic flow, as it is generated from the elliptical shape of the participant region. Elliptic flow decreases for more central collisions due to their on-average more spherical shape [38] as shown in the left side of Figure 2.4.

Elliptic flow is of particular interest as a measurement of the initial state anisotropy and

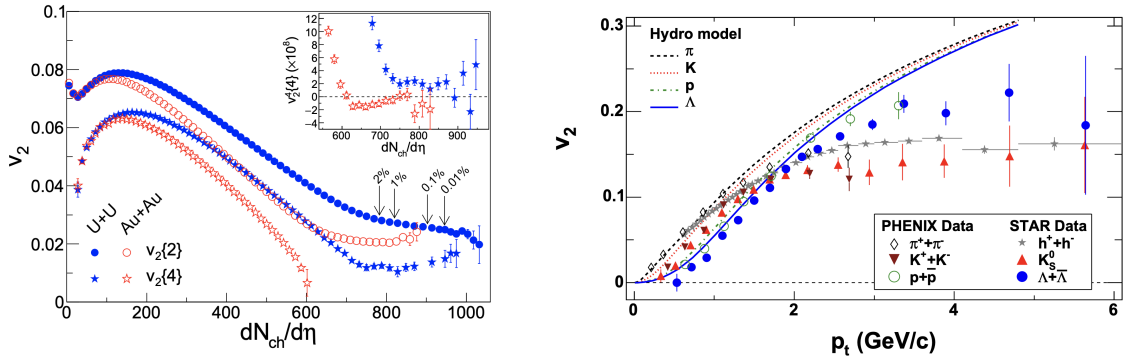

Figure 2.4: Left: v_2 for Au+Au and U+U collisions at $\sqrt{s_{NN}} = 200$ as a function of centrality [38]. Right: v_2 calculated for $\sqrt{s_{NN}} = 200$ GeV Au+Au collisions as a function of p_{T} [39]. Significant non-zero v_2 even at high p_{T}.

an indirect measure of the thermalization time τ_0. Due to the fact that any anisotropy in the pressure gradients is naturally quenched, a large v_2 is considered an indication of a very fast thermalization, with a τ_0 of $0.6 - 1.0$ fm/c being able to reproduce the elliptic flow measured at RHIC energies.

Elliptic flow is also important in jet physics in heavy-ion collisions. As discussed in Chapter 3, jets are measured in the heavy-ion event, and the average energy density of the background can vary significantly based on the relative orientation of the jet axis with the event planes. It is further possible that jets themselves may have some non-zero flow due to enhanced or decreased mean path lengths inside the medium. It is seen, for instance, that high-p_{T} charged hadrons have significant v_2, shown in the right side of Figure 2.4.

Freeze-out

Hydrodynamic models are used to evolve the system from about 1 fm/c until 10-15 fm/c. During this time, the QGP expands and cools, and eventually undergoes a chemical freeze-out - after which there are no inelastic scatterings, and thus particle species multiplicities become fixed, followed by a kinetic freeze-out - when elastic scatterings cease as well. After the kinetic freeze-out, the particles trajectories are essentially unaltered, and they traverse space until they eventually interact with other material, a detector or a decay.

2.2 In situ probes of the QGP

The plasma produced in heavy-ion collisions exists for less than 10^{-22} seconds, and fills a space on the order of the size of a nucleus. Due to these conditions, external tools such as lasers are infeasible for measurement of the QGP. Instead, experiments may use probes produced internally in the collision. Jet production in heavy-ion collisions happens in the pre-equilibrium stages of the collision, before any medium is formed. This allows jets to probe the entire lifetime of the QGP. Because the jet's initiating parton is a colored object, it will interact strongly with the QGP as it propagates, and the result of this interaction with the medium is then extracted via comparison of the heavy-ion measurement to $p + p$ or to pQCD calculations for the process in vacuum.

We will first discuss the theoretical predictions for jet energy loss mechanisms, before discussing important jet measurements and how they motivate the work being presented in this analysis.

2.2.1 Partonic energy loss

While the jet cross section can be calculated analytically, the modification of the produced partons by a strongly-coupled colored medium is non-trivial, both due to the relatively low interaction energy scale, as well as the rapid evolution of the QGP in time. The precise description of the modification of a parton as it passes through the QGP (also known as partonic energy loss or jet quenching), is still an active area of research, but is separated into two components: collisional energy loss (elastic) and medium induced gluon bremsstrahlung (inelastic). In general, at high energies, if the mean free path is larger than the coherence length, the system is in the Landau-Pomeranchuk-Migdal (LPM) regime [40], and radiative energy loss dominates. The radiative energy loss is described by the Bethe-Heitler formula. If the matter density becomes high enough, then multiple scatterings can occur before the radiation of a gluon, which will cause destructive interference and lead to a suppression of the gluon Bethe-Heitler radiation.

The collisional energy loss of a gluon or light quark in a QGP of temperature T can be

estimated to be [41]

$$-\frac{\mathrm{d}E_{coll}}{\mathrm{d}l} = \frac{1}{4}C_R\alpha_s ETm_D^2 \ln\frac{ET}{m_D^2}, \tag{2.5}$$

where $m_D \sim \sqrt{\alpha_s}T$ is the Debye mass, l is the path length in the QGP, and C_R is the color charge, 4/3 for a quark, or 3 for a gluon.

Radiative energy loss (gluon bremsstrahlung) can be estimated by

$$\Delta E_{\mathrm{rad}}^{\mathrm{LPM}} \approx C_R\alpha_s\hat{q}L^2, \tag{2.6}$$

when in the LPM regime. In this equation, $\hat{q} = m_D^2/\lambda$ is the jet transport parameter, or the mean transverse momentum squared transferred from the medium to a hard gluon per unit path length, λ is the parton's mean free path in the medium, and L is the path length.

There are two points of interest in both collisional and radiative energy loss: firstly, both depend on the color charge, implying that quarks are expected to be less suppressed than gluons, leading to a possible method of measuring quark or gluon jets separately. Secondly, both mechanisms are expected to explicitly scale with the path length of the parton through the medium, suggesting the possibility of non-zero jet anisotropic flow, as mentioned in Section 2.1.4, which is consistent with the non-zero charged hadron high-p_{T} shown in Figure 2.4. This path length dependence is also an important motivation for the differential di-jet imbalance measurement presented in this thesis and will be explored more in Chapter 7.

2.2.2 Cross section scaling in heavy ion collisions

Because the hard-scattering of partons can be calculated analytically in pQCD as discussed in Section 1.1.2, predictions for the cross sections of jet observables in heavy-ion collisions can be made by scaling the $p+p$ cross section by the number of binary nucleon-nucleon collisions in the larger system. This relies on the assumption that all binary collisions are identical and independent of each other. Under such an assumption, the hard process

scaling in a heavy-ion collision (with identical nuclei) is given by

$$\langle N_{AA}^{\text{hard}} \rangle(b) = \langle N_{AA}^{\text{coll}} \rangle(b) \sigma_{NN}^{\text{hard}} / \sigma_{NN}, \tag{2.7}$$

also known as the $T_{AA}(b)$. There is strong evidence that $\langle N_{AA}^{\text{coll}} \rangle(b)$ and the nucleon-nucleon cross sections are well-constrained by Glauber calculations, due to the good agreement of γ, $W^{\pm}$ and Z^0 cross sections, which can be used as reference measurements because they carry no color charge and thus experience no energy loss. Because estimation of $\langle N_{AA}^{\text{coll}} \rangle(b)$ is well-constrained, predictions of the cross section for jet observables in heavy-ion collisions (in the absence of any QGP interaction) can be made. Thus, any deviation from these vacuum predictions in heavy-ion collisions can be attributed to the presence of, and modification by, a strongly interacting medium.

2.2.3 Early jet quenching measurements

The current state of the art for identifying jets in a heavy-ion event involves the use of a jetfinding algorithm, which will be discussed in Chapter 3. While jetfinding algorithms were first introduced in the 70s for e^+e^- events by Sterman and Weinberg [42], techniques for robustly identifying jets in a heavy-ion event in a computationally efficient manner were not introduced until the mid-to-late 2000s, with the introduction of FastJet [43]. This means that for the first five-to-ten years of RHIC running, techniques other than jetfinders were used to identify and approximate a hard parton.

The fragmentation of hard partons into jets has some specific characteristics that help in identification of the jets experimentally. Due to momentum conservation, jets must be produced back-to-back in the center-of-mass frame in e^+e^- collisions. In hadron collisions, the hard-scattered partons are not correlated in rapidity, due to the internal motion of the partons inside the incident nuclei. However, they are still tightly correlated in azimuth. This correlation can be broadened slightly by initial-k_t, final-state scatterings, and radiative effects, which may introduce some acoplanarity into the produced jets; however, they are still produced approximately back-to-back. Furthermore, the larger the fraction of energy

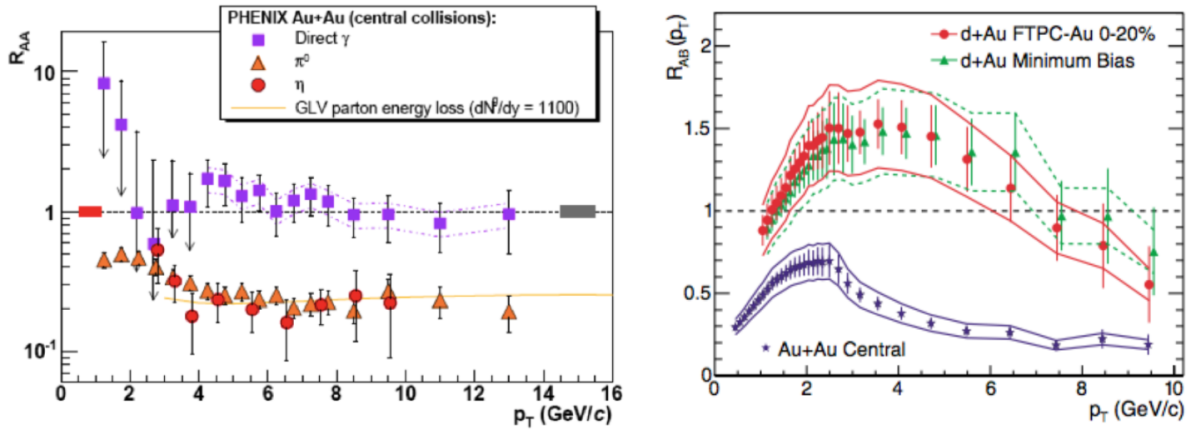

Figure 2.5: Nuclear modification factor for various control measurements. Left: γ R_{AA} is consistent with unity, as expected - this suggests our T_{AA} definition is correct. [44]. Right: the strong suppression in AA is not present in dA, showing that cold nuclear effects are not the dominant mechanism for suppression [45].

carried by any specific hadron in the jet, the more collimated that hadron is with the original parton axis. Therefore, high-p_{T} hadrons can be used as jet-proxies.

High-p_{T} hadrons have been used as jet-proxies since the SPS and early in RHIC; they have been used to measure the strength of jet quenching both in inclusive spectra and correlation analyses.

The first measurements of jet quenching were performed by comparing the number of high-p_{T} hadrons found in heavy-ion collisions compared to what would be found if no energy-loss would occur. This vacuum-like reference is defined from the $p+p$ spectra using the T_{AA} scaling that was defined in Equation 2.7. The ratio of the AA spectra to the T_{AA} scaled $p+p$ is called the nuclear modification factor (R_{AA}), and in its simplest form, for a given rapidity and centrality range, is defined as:

$$R_{AA}(p_{\mathrm{T}}) = \frac{\mathrm{d}N^{AA}/\mathrm{d}p_{\mathrm{T}}}{T_{AA}\mathrm{d}N^{pp}/\mathrm{d}p_{\mathrm{T}}}. \tag{2.8}$$

At top RHIC energies, high-p_{T} hadron production was found to be suppressed by a factor of 4-5 [46], while suppression was not found in reference measurements such as γ R_{AA}, or

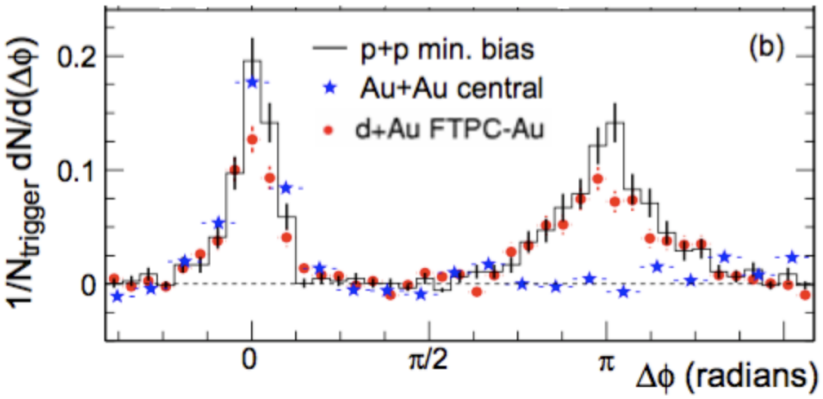

Figure 2.6: STAR di-hadron correlations. Suppression of high-p_{T} associates on the away side in central A+A when compared to p+p or d+Au [45]. $4.0 < p_{\mathrm{T}}^{\mathrm{trig}} < 6.0$ GeV/c and $p_{\mathrm{T}}^{\mathrm{assoc}} > 2.0$ GeV/c.

hadron R_{pA} or R_{dA}, as seen in Figure 2.5 [44, 47–49].

Signatures of jet quenching were also measured in angular correlations of hadrons, or "di-hadron correlations". In these analyses, the relative azimuthal angle ($\Delta\phi = \phi^{\mathrm{trig}} - \phi^{\mathrm{assoc}}$) between a "trigger" particle and "associated" particles are counted across many events. In general, these measurements are done differentially with respect to both the trigger and associated particle p_{T}. Using a high-p_T hadron in an event as the jet proxy, one expects unmodified jets to show peaks in the correlation around $\Delta\phi = 0$, where there is a relative increase in yield due to the jet that the trigger particle came from, and around $\Delta\phi = \pi$, where there should be a relative increase in yield due to the hadrons associated with the recoil jet. As shown in Figure 2.6, we see a strong reduction in yield of high-p_{T} constituents in the recoil jet in central Au+Au collisions, showing a significant modification of the recoil jet that can be attributed to the presence of the QGP - not cold nuclear matter effects - because the d+Au recoil jet yield is consistent with the $p + p$ yield, ruling out cold nuclear matter effects. These measurements firmly established the presence of jet quenching in heavy ion collisions, showing these high-p_{T} partons are effective probes of the QGP.

The measurement of jet quenching using reconstructed-jet observables at STAR will be

continued in Section 3.4, after current jetfinding techniques have been introduced.

3 JETFINDING

"There is nothing like looking, if you want to find something. You certainly usually find something, if you look, but it is not always quite the something you were after."

– J.R.R. Tolkien, *The Hobbit*

While the high-p_{T} hadrons that were used in the early life of RHIC to approximate jets are strongly correlated with the original jet axis, they are not as tightly correlated to the parton's energy. To better estimate the full kinematics of the initiating parton, one must attempt to fully reconstruct it from the resulting shower of hadrons, in a process called jetfinding.

Jetfinding, however, is a non-trivial task. The stochastic nature of jet fragmentation requires a well-defined algorithm to theoretically and experimentally reconstruct the initiating parton from the random distribution of final-state particles, as illustrated in Figure 3.1.

For a jetfinding algorithm to be meaningful in both theory and experiment, it is necessary for the algorithm to satisfy two requirements, it must be both infrared and collinear (IRC) safe. Infrared safety implies that a jetfinding algorithm's resulting jets will be unaffected by the addition of any number of infinitely soft particles to the event ($p_{\mathrm{T}} \approx 0$). Collinear safety, on the other hand, requires that the jetfinding algorithm be stable if any particle in the event is replaced by two particles such that they are infinitesimally close in angle, and that their total energy equals that of the original particle. Theoretically, IRC safe algorithms allow for calculation of finite cross sections. In IRC unsafe algorithms, the set of jets calculated from the tree level diagrams and the set calculated from higher order loop diagrams do not match, and their divergences will not cancel, leading to infinite cross sections. These properties also have important implications for experiments. When an algorithm is IRC safe it is only sensitive to the total energy flow of the jet, reducing the sensitivity of the algorithm to effects such as tracking or calorimeter resolution.

In the past, in $e^+ + e^-$ and $p + p$ collisions cone-finding algorithms have been used.

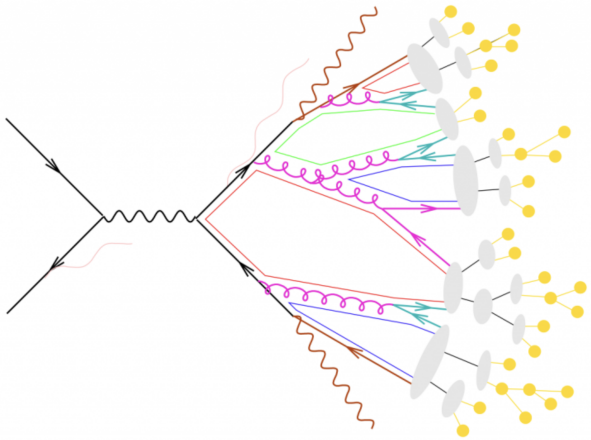

Figure 3.1: Artistic render of a parton shower [50].

These traditionally work by starting with a "seed" (usually a high-p_{T} hadron). However, these algorithms are not IRC-safe; naive implementations to make them safe have poor runtime scaling with the number of particles, making them infeasible for work in heavy-ion experiments.

3.1 Sequential recombination algorithms

The current state of the art are the sequential recombination algorithms, which are IRC safe by construction. The most widely known are the k_t family of algorithms, which are defined by the following distance metrics:

$$d_{ij} = \min(p_{Ti}^{2p}, p_{Tj}^{2p})\Delta R_{ij}^2/R^2, \tag{3.1}$$

$$\text{and} \quad d_{iB} = p_{Ti}^{2p}, \tag{3.2}$$

where $\Delta R = \sqrt{(\eta_i - \eta_j)^2 + (\phi_i - \phi_j)^2}$, and R sets the relative size of the resulting jets, with a larger R leading to larger jet areas. Because of this, R is sometimes called the jet radius, but is more correctly named the jet resolution parameter. The algorithm works by starting with a list of all the "pseudo-jets" in the event, whether it be charged particles, calorimeter hits, etc. From this list, it builds a table of distances between all pseudo-jet pairs using

the distance measure d_{ij} defined above, and the distance from the pseudo-jet to the beam: d_{iB}. The algorithm then combines the two closest pseudo-jets in this metric repeatedly. If a pseudo-jet's d_{iB} is smaller than any of its d_{ij} distances, then that pseudo-jet is considered a jet. Once all pseudo-jets have have no d_{ij} smaller than their d_{iB}, clustering is finished and all objects left are candidate jets.

The k_t family is differentiated into individual algorithms by modifying the power p in Equation 3.1. When p is positive, the algorithm preferentially clusters soft pseudo-jets first; the specific case of $p = 1$ is called the k_t algorithm [51, 52]. When p is zero, the distances are unweighted by p_{T} and are purely geometrical: this is known as the Cambridge/Aachen algorithm [53, 54]. Finally, if $p = -1$, the algorithm preferentially clusters hard constituents first, and is known as the anti-k_t algorithm [55]. In general, anti-k_t is found to have the best properties for jet-finding, especially in heavy-ion collisions, where it is less susceptible to smearing from the underlying event. Because of this, the field has converged on using anti-k_t as the de-facto standard jet-finding algorithm. However, to estimate the background energy density as described in Section 3.2, the k_t algorithm is used.

The FastJet software package was used for all jetfinding done in this thesis [43, 56, 57].

3.2 Background estimation in heavy-ion collisions

In an $e^+e^- \to q\bar{q}$ event, the jet production is clean, without any underlying event. In any hadron collision, even $p+p$ collisions, jet production is not the only source of final-state particles, and these other particles from other processes can affect the measurement of jet properties. This is further complicated as the size of the colliding nuclei increases. In a heavy-ion event at RHIC or LHC energies, the jet is embedded into an event consisting of hundreds or thousands of "background" particles, which can smear the resolution of the jet, or even create "fake" jets due to combinatoric fluctuations.

To estimate the kinematics of the initiating parton of a jet in such an environment, the background contribution to the clustered jet must be estimated and corrected for. In this work, we use area-based background estimation methods using the catchment jet area as

defined by FastJet [43, 57].

The area of a jet is estimated using "ghosts". A large number of ghost particles (which are 4-vectors that have approximately zero energy) are included in the clustering and are randomly distributed throughout the event. Because the k_t algorithms are infrared safe, particles with such low energy will not affect the clustering history. The area of the jet is then given by

$$A_{jet} = A_{\text{embedding}} \frac{N_{\text{ghosts}}^{\text{jet}}}{N_{\text{ghosts}}^{\text{total}}}, \tag{3.3}$$

where $A_{\text{embedding}}$ is the total area in which ghosts are embedded, $N_{\text{ghosts}}^{\text{jet}}$ is the number of ghosts that were included in the jet, and $N_{\text{ghosts}}^{\text{total}}$ is the total number of ghosts that were embedded.

The background p_{T} density, ρ, is estimated by clustering the full event using the k_t algorithm. The p_{T} density is given by

$$\rho = \text{median}\{\frac{p_{\text{T},i}^{\text{raw}}}{A_i}\}, \tag{3.4}$$

the median of the set of jet candidates of the event. An example of the measured ρ at STAR in the 20% most central events is shown on the left side of Figure 3.2. This significant ρ is due to the large density of particles produced in central collisions. For 0-10% central events, dN/dY is approximately 600; assuming the QGP is a black body with a temperature of about 250, the mean p_{T} of produced particles would be around 500 MeV, leading to a ρ before accounting for detector effects of about 50 GeV/A from charged tracks, or 75 GeV/A for charged tracks and neutral calorimeter deposits, under the assumption that all produced particles are pions. By convention, we remove the two highest p_{T} jets from the set before calculation of the median, to reduce the effect of any true jets in the event on ρ. Using the estimate of the background p_{T}, we construct a corrected jet candidate p_{T} as

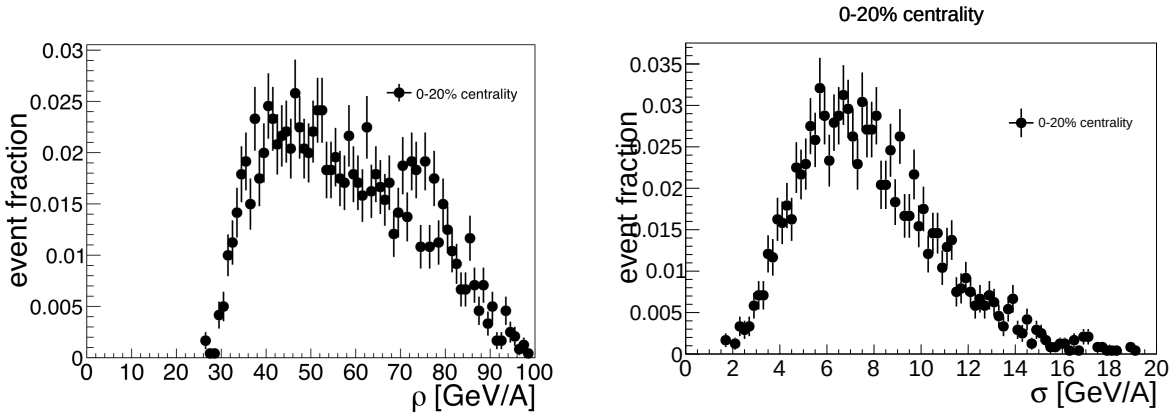

Figure 3.2: Left: ρ distribution measured at STAR in the 20% most central collisions. Right: Intra-event σ for the same events.

$$p_{\mathrm{T}}^{\mathrm{jet}} = p_{\mathrm{T}}^{raw} - \rho A^{\mathrm{jet}}. \tag{3.5}$$

This corrected p_{T}, however, cannot account for fluctuations in the background p_{T} density of the event. This leads to a significant uncertainty on the jet candidate's p_{T}, which we characterize by the width of the intra-event ρ distribution, or σ. At STAR collision energies in the 20% most central events, σ, as shown in Figure 3.2, can be large enough that fluctuations can create jet candidates with background-subtracted p_{T} on the same order as the jet kinematics accessible at STAR. These "fake" jets must be removed from the jet candidates or corrected for before meaningful measurements of jet observables can be made. There are statistical tools to remove fake jets at the ensemble level, such as the mixed-event method. However, there are also some techniques that allow for event-by-event classification of jets as having probably originated from a hard scattering, instead of a random background fluctuation. Section 3.3 discusses one such method developed at STAR: hard-core jets.

3.3 Hard-core jets

Hard-core jet tagging takes advantage of the fact that on average, a vacuum-like jet fragmentation leads to constituent hadrons that have significantly higher p_{T} than hadrons produced from the QGP (as discussed above, $\langle p_{\mathrm{T}} \rangle \approx 500$ MeV). Therefore, when performing

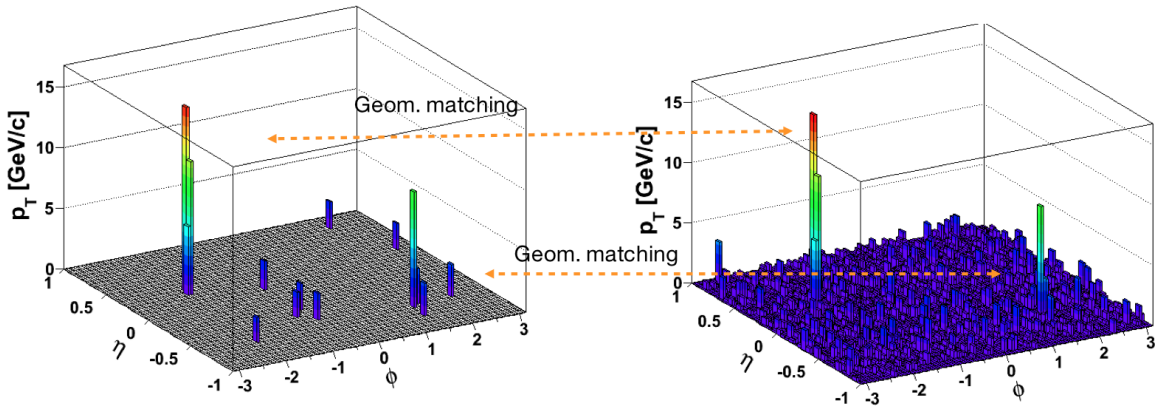

Figure 3.3: An illustration of hard-core jetfinding in an Au+Au event. A high $p_{\mathrm{T}} > 2.0$ GeV/c cut has been applied to the full event - this eliminates the majority of tracks and towers that did not originate from the hard process. Jetfinding can be performed and will pick out the hard-core di-jet. The full event (right side) can then be clustered with all constituents down to $p_{\mathrm{T}} > 0.2$ GeV/c, and matched to the original hard-core jets using the radial distance in $\eta \times \phi$.

jetfinding only with the constituents of an event with p_{T} above some high threshold, the background energy density is significantly reduced or eliminated for all practical purposes. Thus, any jet found with a hard-core selection has a much higher probability of originating from a hard scattering than a jet found in the full event would. This increases the purity of the jet sample considerably. Coupling this with a high-p_{T} cut on the hard-core jets can give an effectively pure di-jet sample. The full event with all constituents within the detector's acceptance can then be clustered and geometrically matched to the original hard-core jets, giving access to the full jet energy, while being certain that the jet originated from a hard process and is not just a fluctuation in the energy density of the event. An example of hard-core jetfinding and matching procedure is shown in Figure 3.3. Because there are some differences in the jetfinding procedures in the di-jet hadron correlations and the differential di-jet imbalance, the details will be explained in Chapters 6 and 7, respectively.

3.4 Previous hard-core jet measurements at STAR

The application of hard-core jetfinding at STAR originated in the jet-hadron correlations. This analysis can be considered a continuation of the di-hadron correlations, introduced in

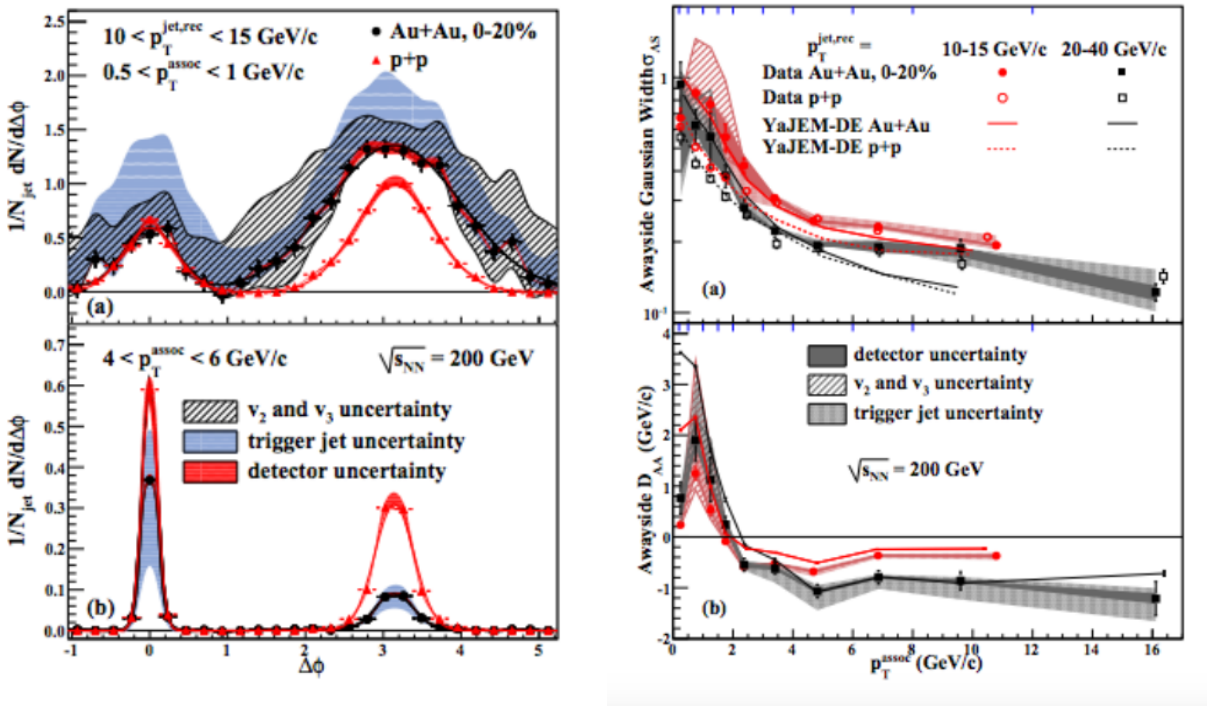

Figure 3.4: STAR jet-hadron correlations. Left: jet-hadron correlations for a hard-core trigger jet with $10 < p_{\mathrm{T}} < 15$ GeV/c, and associated hadrons with $0.5 < p_{\mathrm{T}} < 1.0$ GeV/c on top and $4.0 < p_{\mathrm{T}} < 6.0$ GeV/c on the bottom. Right: Gaussian width of the away-side peak on top, and away-side $\mathrm{D_{AA}}$ on bottom. [58]

Section 2.2.3, by replacing the trigger hadron with a reconstructed hard-core jet. The jet-hadron correlations are shown on the left side of Figure 3.4. STAR observed a significant reduction in the yield of recoil jet high p_{T} associated tracks along with a corresponding increase in the yield of low-p_{T} tracks below 2.0 GeV/c. The total energy loss/gain per associated p_{T} bin with respect to $p+p$ collisions can be quantified by the $p_{\mathrm{T}}^{\mathrm{assoc}}$ weighted difference in yield, given by

$$\mathrm{D_{AA}}(p_{\mathrm{T}}^{\mathrm{assoc}}) = Y_{\mathrm{AA}}(p_{\mathrm{T}}^{\mathrm{assoc}}) \cdot p_{\mathrm{T,AA}}^{\mathrm{assoc}} - Y_{\mathrm{pp}}(p_{\mathrm{T}}^{\mathrm{assoc}}) \cdot p_{\mathrm{T,pp}}^{\mathrm{assoc}}, \tag{3.6}$$

and by

$$\Sigma\mathrm{D_{AA}} = \Sigma_{p_{\mathrm{T}}^{\mathrm{assoc}}}\mathrm{D_{AA}}(p_{\mathrm{T}}^{\mathrm{assoc}}), \tag{3.7}$$

the total difference in associated yield weighted by p_{T}, as shown in the right panel of Figure 3.4. We see immediately that the crossover point between positive $\mathrm{D_{AA}}$, which shows an enhancement in total energy, and negative $\mathrm{D_{AA}}$, which shows a suppression in energy in the given $p_{\mathrm{T}}^{\mathrm{assoc}}$ bin is constant as a function of the jet p_{T}, suggesting the relevant scale for energy loss is the medium temperature, not the jet energy scale. Furthermore, $\Sigma\mathrm{D_{AA}}$ is zero within errors, providing good evidence that not only is the measured non-zero $\mathrm{D_{AA}}$ being caused by a reshuffling of energy due to medium modification, but that the quenched energy is being recovered within the significantly broadened away-side peak for all $p_{\mathrm{T}}^{\mathrm{assoc}}$ bins.

Hard-core jets were also used to tag di-jet events to measure the di-jet imbalance, defined as

$$A_J = \frac{p_{\mathrm{T}}^{\mathrm{lead}} - p_{\mathrm{T}}^{\mathrm{sublead}}}{p_{\mathrm{T}}^{\mathrm{lead}} + p_{\mathrm{T}}^{\mathrm{sublead}}} \quad . \tag{3.8}$$

The di-jet imbalance was first measured at the LHC by ATLAS and CMS [59,60]. The LHC experiments measured a significant imbalance with respect to unquenched Monte Carlo jet models in the most central collisions, and good agreement with the models in more peripheral

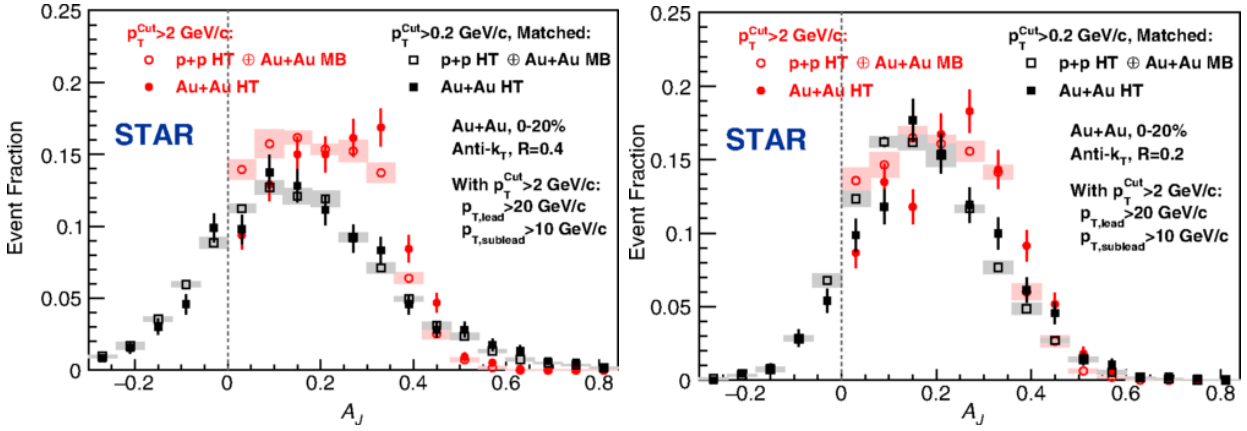

Figure 3.5: STAR di-jet imbalance. Left: hard-core and matched di-jet imbalance for jet radius R=0.4. Right: R=0.2. [61]

collisions, showing a strong centrality dependence to the jet quenching. Furthermore, CMS analyzed the radial distribution of the quenched energy and found it to be at large angle ($\Delta R > 0.8$) from the jet cone.

In STAR, the A_J was measured for both the hard-core and matched di-jets in central Au+Au collisions and compared to a p+p reference [61], as shown in Figure 3.5. A hard-core di-jet pair was found, requiring $p_{\mathrm{T}}^{\mathrm{lead}} > 20.0$ GeV/c for the highest-p_{T} jet, and $p_{\mathrm{T}}^{\mathrm{sublead}} > 10.0$ GeV/c for the second-highest-p_{T} jet. For jets with a radius of $R = 0.4$, the hard-core di-jets were significantly imbalanced compared to the p+p reference. However, the corresponding matched di-jets were balanced with respect to the p+p reference, showing that any energy loss in the hard constituents of the lead or recoil jet is recovered inside the jet radius. When the procedure is repeated for jets with a more narrow radius of 0.2, the matched jets are no longer balanced, showing that although there is some broadening of the jet, the broadening is contained within the original radius of 0.4, which is significantly more narrow that what was seen at LHC energies.

This shows a significant difference compared to the jet-hadron correlations discussed above, where there is only a single trigger jet, and the recoil jet was very broad - the width approached 1 for the lowest-p_{T} associated hadrons, as shown in the right panel of Figure 3.4.

In the di-jet imbalance, however, with the requirement of a hard-core recoil jet, the width of the distribution appears to be significantly narrower, contained within a cone of $R = 0.4$. If this were not the case, the matched jets could not be balanced to the level of the p+p reference.

This strong evidence for jets that are significantly modified, but still relatively narrow, and completely contained within the original jet axis, suggests opportunities that are not available to a more general population of modified jets, such as measuring the full fragmentation function and being able to more accurately estimate the initiating parton's energy.

However, from the di-jet imbalance alone, we cannot directly measure the broadening of the radiated energy, nor can we measure the constituent to directly investigate suppressions of high-p_{T} constituents or enhancements of low-p_{T} constituents. These questions motivated the di-jet hadron correlations that we performed, which are the topic of Chapter 6.

4 ACCELERATOR AND DETECTOR FACILITIES

"That's the only place in all the lands we've ever heard of that we don't want to see any closer; and that's the one place we're trying to get to!"

– J.R.R. Tolkien, *The Lord of the Rings*

All data used in this thesis comes from collisions produced at the Relativistic Heavy Ion Collider (RHIC) and recorded by the Solenoidal Tracker At RHIC (STAR) detector, located at Brookhaven National Laboratory (BNL). In this chapter we give a brief overview of the RHIC accelerator complex, the STAR detector, and the subsystems of interest for the research presented in this work. The full accelerator complex (shown in Figure 4.1) at BNL is capable of performing a variety of experiments, from low-energy fixed-target experiments to radiation studies for NASA. This work will only address those systems that are pertinent to the production of gold (Au) and proton (p) beams in the main RHIC ring.

RHIC and STAR are regularly upgraded, and as such the run configuration changes from year to year. If a subsystem has been modified since the data used in this analysis was recorded (2006 & 2007), then both the current state as well as the state during the 2006/2007 run will be described.

4.1 Relativistic Heavy Ion Collider (RHIC)

RHIC [62, 63] is a multi-purpose accelerator facility capable of producing beams of ions ranging in size from hydrogen ($N = 1$) to uranium ($N = 238$), at multiple collision energies. As of today, RHIC has run with beams of ${}^{1}_{1}\mathrm{H}$, ${}^{2}_{1}\mathrm{H}$, ${}^{63}_{29}\mathrm{Cu}$, ${}^{96}_{40}\mathrm{Zr}$, ${}^{96}_{44}\mathrm{Rb}$, ${}^{197}_{79}\mathrm{Au}$, and ${}^{238}_{92}\mathrm{U}$. The collider is also able to run in a variety of center-of-mass collision energy per- nucleon-pair configurations, ranging from $\sqrt{s_{\mathrm{NN}}} = 7.7 - 500$ GeV, depending on the charge-to-mass ratio (Z/N) of the species being accelerated, with protons (${}^{1}_{1}\mathrm{H}$) having a maximum energy-per-nucleon of 250 GeV, and species with a smaller Z/N having a maximum energy-per-nucleon of $Z/N \times 250$ GeV.

Currently, the accelerator complex uses an electron beam ion source (EBIS) [64] to be able to produce a large variety of ions for RHIC and other experiments. For the Au+Au

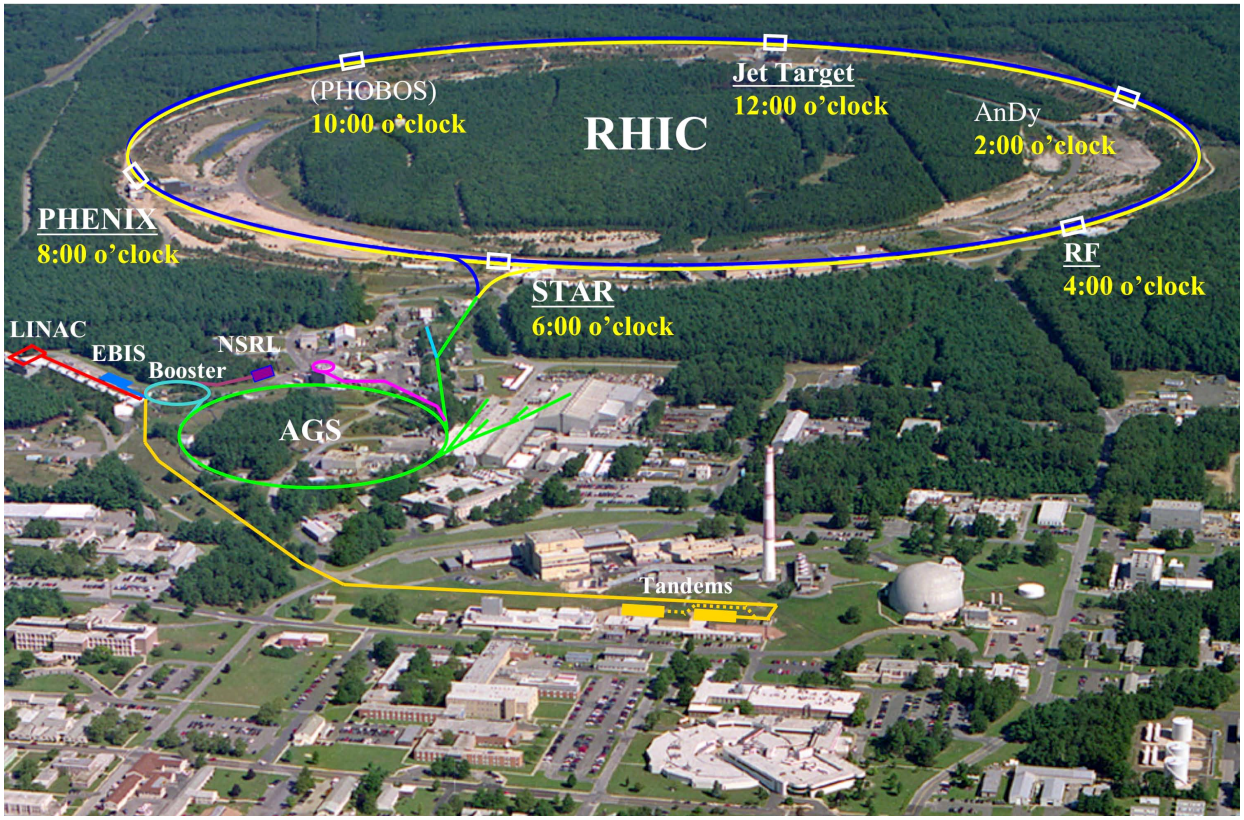

Figure 4.1: The RHIC accelerator complex.

collisions recorded in 2007, however, Au ions were produced from a Tandem Van de Graaf generator. A pulsed sputter ion source produced negatively ($q = -1$) charged ions, which were then stripped of some of their electrons in the Tandem Van de Graaf. From there, the ions are fed into the Booster Synchrotron. The booster further strips electrons, and accelerates the ions to 95 MeV per nucleon. The ions are then fed into the Alternating Gradient Synchrotron (AGS), which strips off the remaining electrons, and accelerates the ions to 8.86 GeV. The bare ions are then fed into the RHIC ring via the AGS-to-RHIC Transfer Line (ATR), which enters RHIC from the south (6 o'clock position). Once RHIC is filled (a maximum of 111 bunches of ions in each direction), the beams are accelerated to their target energy. The proton accelerator chain is the same, except for the source - hydrogen is produced, fully stripped ($q = +1$) from the Linear Accelerator (LINAC), not the EBIS or Tandems.

The RHIC storage ring is an intersecting storage ring (ISR) particle accelerator with two independent rings named blue and yellow. The two independent rings allow for the collisions of asymmetric species. The two storage rings are hexagonally shaped, and have a circumference of 3.834 kilometers. The beams are steered and focused by 1,740 helium-cooled superconducting magnets that operate with a maximum field strength of 3.5 T.

The beams cross at six "interaction points". Therefore, up to six experiments can be active at RHIC at any time. In 2000 when RHIC started, four experiments were active: STAR, PHENIX, BRAHMS, and PHOBOS. The PHOBOS experiment ended data-taking in 2005, BRAHMS in 2006, and PHENIX in 2016, leaving STAR the only active large experiment at RHIC. Other, smaller experiments have been active at RHIC, such as pp2pp (now incorporated into STAR), and A_NDY. sPHENIX, a new, large-scale experiment is planned to be commissioned and ready for data-taking in the early-to-mid 2020s. The long-range plan for RHIC is currently uncertain, as it may be decommissioned in the mid-to-late 2020s for the installation of an electron gun, turning the storage ring into an electron-ion collider (EIC).

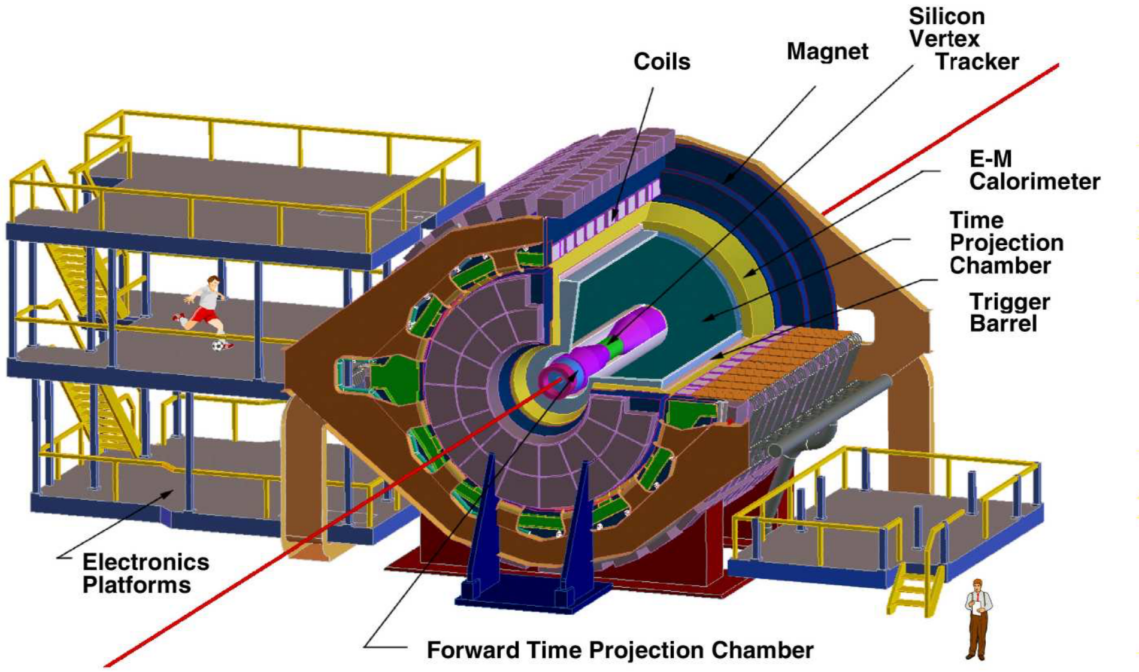

Figure 4.2: The STAR detector and some of its primary subsystems, including the magnet and TPC. Configuration shown is consistent with the data used in this thesis from 2006 and 2007.

4.2 Solenoidal Tracker At RHIC (STAR)

The STAR detector [65] was originally designed to study bulk observables, requiring a large acceptance and excellent tracking. STAR covers the largest solid angle of the RHIC detectors, and provides tracking via the large Time Projection Chamber (TPC) at the heart of the experiment, from which it takes its name. In this section we introduce many of the subsystems and upgrades that STAR has undergone over its 19 years of active data-taking at RHIC, including the primary tracking system, calorimetry, forward detectors and its multiple trigger systems.

4.2.1 Detector structure

Magnet

The largest and heaviest part of the STAR experiment is the magnet, which is shown in the right side of Figure 4.3 [66]. It is a solenoidal magnet designed not only to provide a very uniform magnetic field parallel to the beam direction, but also to provide structural support for, or completely contain, multiple other subsystems, including the TPC and the barrel calorimeter. Nominally, STAR operates at a field strength of $B_z = 0.5$ T, called full-field, or reversed full-field (when the field direction is reversed), but a half-field configuration with $B_z = 0.25$ T has also been used. This strong magnetic field is needed to bend charged particles passing through the TPC sufficiently to allow a precise measurement of the radius of curvature of the bent track, to estimate the momentum of the track. At a full-field setting, charged tracks with a transverse momentum of 0.2-10.0 GeV/c can be reconstructed with good momentum resolution. Below the 0.2 GeV/c threshold tracks do not reach the outer edge of the TPC and instead loop (and are therefore not found by the tracking algorithm). Above the 10.0 GeV/c limit a track's trajectory is straight enough that the error in the momentum resolution (and even the charge, as the transverse momentum increases further) becomes large.

The magnet is water-cooled, operating at room temperature, and consumes about 3.5 MW. The full magnet system consists of the main coils, poletips, and the space trim and poletip trim coils, which assist in maintaining field uniformity throughout the entire enclosed volume. The field is reproducible to about 0.5 Gauss, and time variations are less than 0.1 Gauss/12 hours. Radial deviations are less than 50 Gauss, and azimuthal variations are better than 3 Gauss. These performance parameters are required to achieve high-accuracy for high energy electron reconstruction ($\sim$200 μm), and estimates of the accuracy with which the magnetic field could be measured at $\sim$0.5 Gauss.

The magnet weighs approximately 1,100 tons, and rests on two 35 ton cradles. The cradles rest on rollers and have high-power pistons that allow the magnet - and thus the

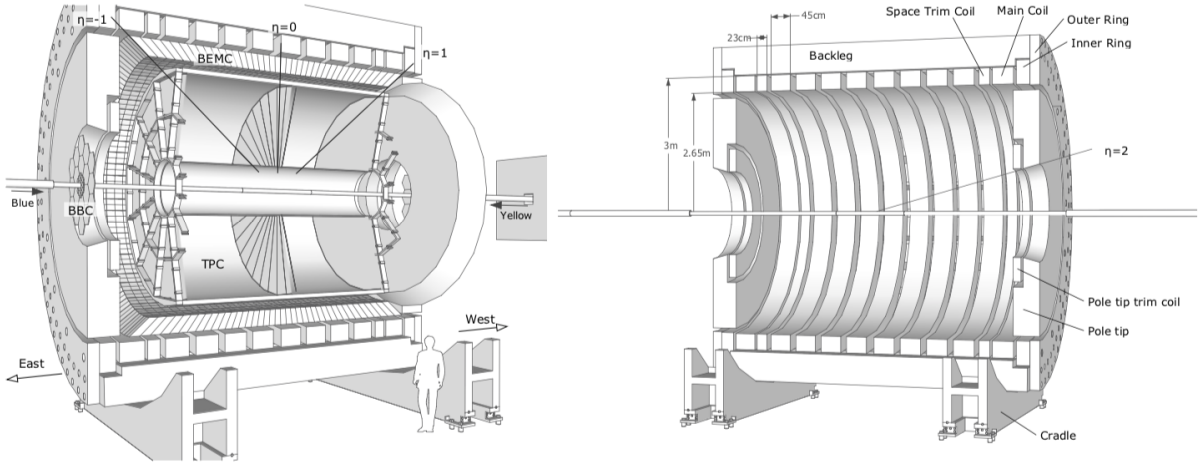

Figure 4.3: Left: Cross-section of some of the major STAR components. Right: Cross-section of the STAR magnet.

entire detector assembly and support structure - to be rolled out of the experiment hall on rails into the assembly building for maintenance.

4.2.2 Barrel detectors

Time projection chamber (TPC)

The TPC is the central detector and primary tracking device of the STAR experiment [67], with a full 2π azimuthal coverage in the pseudorapidity window $|\eta| < 1.0$ (for a definition of the coordinate system used in collider experiments, see Appendix A). At the time it was built, the STAR TPC was the largest time projection chamber in the world, being 4.2 M long with a 4 M diameter and an inner radius of 50 cm. The chamber is filled with P10 gas (10% methane, 90% argon), which is held at 2 mbar above atmospheric pressure to prevent ingress of external gasses such as oxygen. P10 has a high and stable drift velocity of about 5.45 cm/μs. The barrel is bisected in the transverse plane by the central membrane, a thin conductive disk, which is held at around 28 kV, which, along with the inner and outer field cages and the anodes (the barrel endcaps, held at 0 V) produces strong, uniform, and opposite direction electric fields in each half of the detector. The electric field is about 135

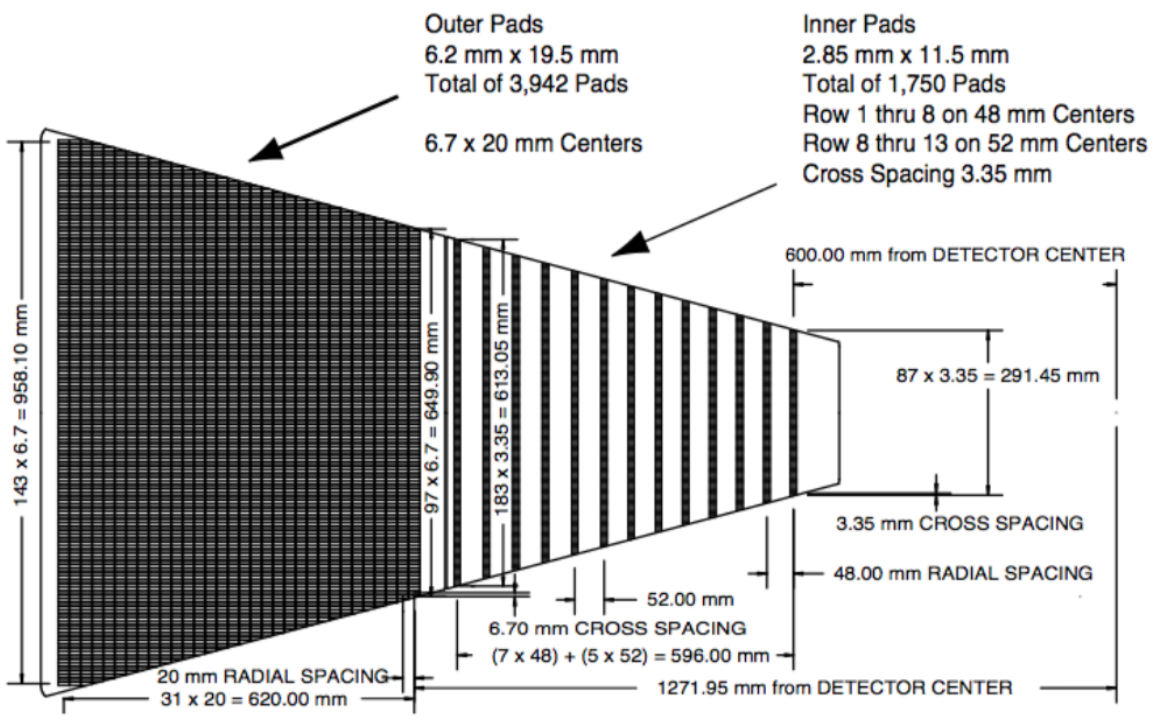

Figure 4.4: Diagram of one of STAR's 24 readout sectors.

V/cm, and runs parallel to the beam pipe, meaning charged particles will drift in the field along the z direction.

As charged particles from a collision traverse through the TPC, the gas is ionized, leaving behind a trail of freed electrons. These electrons drift in the electric field towards the nearest endcap, where they are recorded by readout planes. The uniformity of the electric field is important to allow for electron paths of up to 2.1 m to have sub-millimeter precision during reconstruction.

Each endcap is split into 12 individual sectors, each of which is split into an inner and outer sub-sector as shown in Figure 4.4. The sectors contain readout pads, consisting of multi-wire proportionality chambers (MWPC) with pad readout. Each chamber consists of four parts - a pad plane and three wire planes. From the endcap inwards, the layers are: the pad plane, the anode plane composed of 20 μm wires, the ground wire plane, and finally the

gating grid, which is used to maintain the boundary conditions of the electric field in the TPC. When the gating grid is in a closed configuration (wires alternating +75 V, -75 V), no electrons or ions can pass the plane, stopping the nearly continuous flow of electrons towards the readout plane. When the gating grid is in an open configuration (all wires at +110 V), the electrons are accelerated through, inducing an electron avalanche that produces a signal in the readout plane.

The inner sub-sectors consist of 1,750 small pads in 13 rows with wider spacing, while the outer sub-sectors consist of 3,942 densely packed larger pads in 32 rows. The pad sizes were chosen so that the induced charge from the avalanche would not be shared by more than 3 pads. A gaussian fit or weighted mean can then be used to determine the center of the avalanche in the $x - y$ plane. The $x - y$ resolution is typically equal to or better than 20% of the pad's narrow dimension. When two or more of these ionization events overlap, they can be separated into multiple hits. This happens when two tracks where not spatially distinct at some point in their trajectory. Once these ionization clusters have been separated and fit, they are converted into individual, distinct hits in the $x - y$ plane.

Each track, therefore, is recorded as a discrete set of $x - y$ coordinates in the plane transverse to the beam. The z-value can be measured by timing - because the electric field in the TPC is uniform and the drift velocity is calibrated, one can use the collision timing and the time-to-readout of each electron to measure z using the drift velocity of the gas in the TPC. This creates a 3D point cloud of individual "hits", as shown in Figure 4.5.

From this point, the cloud of hit points must be reconstructed into individual tracks; a non-trivial task when a single event could produce on the order of 10^5 hit points. Track-finding begins at the outer-most pad row, where the hit density is lowest. Hits from the outermost three pad-rows are permuted to find "reasonable" track seeds. From there, each track is projected into the next pad row - if a hit within a reasonable tolerance is found, it is added to the track segment and the procedure is repeated until the innermost pad row is hit or the track is discarded based on quality criteria. Once this is done, the tracks are

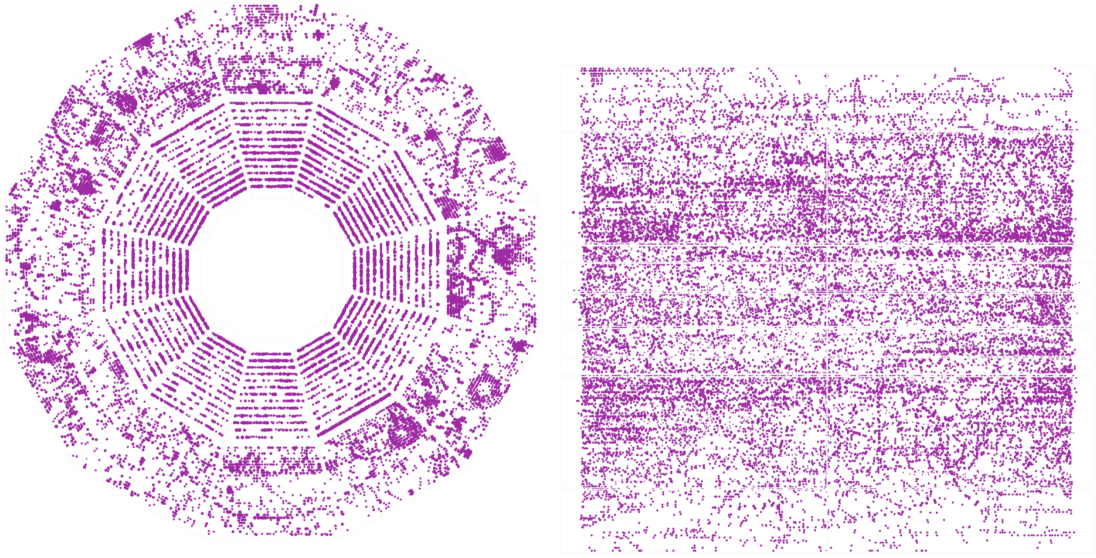

Figure 4.5: Left: $x - y$ projection of the 3D volume of hit points in a single event. Right: lateral view of the same event.

fit with a helix. The full helix requires five parameters, so five fit points is the minimum number required for a track to meaningfully constrain the helix. Corrections for multiple scatterings, space charge, and other effects are taken into account.

This set of "global" tracks is used to estimate the primary vertex by finding clusters of tracks along the beamline. An iterative procedure applying more stringent track and vertex cuts is used. Once a vertex is found, the tracks with a distance-of-closest-approach (DCA) of less than 3 cm from the vertex are refit, constrained to pass through that vertex. These refit tracks are considered primary tracks. If the refit does not converge, the track is not considered primary. Therefore, each primary track with a DCA less than 3 cm is matched to a global track, but all global tracks with DCA less than 3 cm do not match to a primary track.

From the radius of the helix we are able to determine the momentum of the track, and from the direction of curvature we can extract the charge. The TPC can also measure the ionization energy loss of a charged particle as it traverses the gas ($\mathrm{d}E/\mathrm{d}x$) [68–70], and the

magnitude of the energy loss can be characterized by the Bethe-Bloch formula. One of the TPC's advantages over silicon tracking is that this energy loss specifically depends on the track's velocity, not momentum - this means that the species of the particle can be inferred via the relationship between mass, momentum and velocity.

As of 2019, the inner sectors of the TPC were replaced - called the iTPC upgrade. The inner sectors of the iTPC have denser and smaller MWPCs [71], leading to a larger number of pad rows in the inner sectors. This increase in the number of pad rows leads to a larger number of possible fit points per track, allowing tracks at larger rapidity to be reconstructed, effectively increasing STAR's track rapidity acceptance from $|\eta| < 1.0$ to $|\eta| < 1.5$.

Barrel electromagnetic calorimeter (BEMC)

The BEMC is a lead-scintillator sampling electromagnetic calorimeter [72], covering the full 2π in azimuth, as well as a full two units in pseudorapidity, $|\eta| < 1.0$. The detector serves three primary purposes: to trigger on high-p_{T} processes such as jets; to measure the electromagnetically interacting neutral particles such as photons and neutral pions; and to help discriminate between hadrons and electrons.

The BEMC consists of 4,800 towers, each projective back to the nominal center of the detector. Each tower has an angular coverage of 0.05×0.05 in $\eta \times \phi$. The detector is split into 120 modules, each covering one unit in pseudorapidity, and 6° in ϕ. Each module consists of 40 towers: two in ϕ and 20 in η. Each tower consists of alternating layers of scintillator and lead. Electromagnetically interacting particles interact with the dense lead layers leading to a cascade of lower-energy electrons and photons which penetrates deeper into the tower. The scintillator levels transform this electromagnetic shower into a light signal, which is read out and digitized by a PMT outside of the STAR magnet.

The BEMC also includes a shower-maximum detector (SMD) between the fifth scintillator layer and the sixth lead layer. The SMD allows the width of the shower to be measured, which can help to discriminate between photons and neutral pions, as well as to discriminate

electrons from hadrons.

The final major use of the BEMC is as a trigger detector for hard processes, such as jet production. A high-tower event (HT) is an event where a single tower had a significant energy deposition - assumed to be a high energy photon or π^0. A π^0 will decay into two photons. Below an initial π^0 energy of 6 GeV, these photons will usually be recorded in different towers, but above 6 GeV the decay is boosted enough that the photons are very collimated and will generally be recorded in a single tower. A second type of BEMC trigger, called a jet-patch trigger (used in $p + p$ analyses only) can measure if a large amount of energy was deposited in an extended 1.0×1.0 area in $\eta \times \phi$.

4.2.3 Forward detectors

Forward detectors (in this case, detectors with a nominal pseudorapidity larger than the TPC) are important for extending the effective coverage of the detector, triggering on collision remnants, and estimation of the event plane.

Zero degree calorimeter (ZDC)

Every RHIC experiment has a pair of zero degree calorimeters installed past the first bending magnets in the RHIC rings, which collect neutral collision remnants (neutron spectators) that diverge less than 4 mr from the beamline at the interaction point. The ZDC therefore can be used as a minimum-bias trigger in heavy-ion collisions, as well as a luminosity and beam measurement tool for the accelerator [73].

Vertex position detector (VPD)

The VPDs are two identical forward detectors installed around the beam line at a distance of 5.7 meters from the center of the STAR experiment. Using photon coincidence measurements, the VPD allows for very good detection of the collision location along the beamline, and provides the "start time" for multiple other detectors that require precise collision timing, such as the TOF and MTD [74].

Beam-beam counter (BBC)

The ZDC is not applicable for collisions in $p+p$ collisions where there are no spectator neutrons. Instead, beam-beam counters installed at $z = \pm 3.7$ m are used for luminosity monitoring, v_z estimation, and triggering. The BBC can also be used as a local polarimeter in polarized $p+p$ runs [75].

4.2.4 Other detector components

STAR hardware is consistently being installed, upgraded, and removed as the physics of interest changes, and as technology improves. Below is a quick list of some of the most important systems to highlight the range of capabilities STAR has had over the years.

- Inner silicon tracking systems such as the Silicon Vertex Tracker (SVT) [76] and the Heavy Flavor Tracker (HFT) [77] were used to improve tracking accuracy and allow the study of heavy flavor decays.
- A Time of Flight (TOF) [78] detector was installed outside the TPC barrel to improve particle identification in the high-p_T regime.
- A Muon Telescope Detector (MTD) [79] was installed outside the magnet to track muons, due to their high probability of escaping both the BEMC and magnet material.
- Forward Time Projection Chambers (FTPCs) [80] where installed inside the primary TPC. These gave access to charged tracks at large rapidity, which the primary TPC could not reconstruct.

4.2.5 Triggering

The STAR TPC can record events at around 500 Hz. However, at current luminosities, RHIC can deliver collisions at a rate of over 100 kHz. Since STAR is unable to record every collision, smart selection of which events are recorded is necessary. Therefore, instead of immediately recording every time the TPC is ready, we instead look for signals in fast detectors such as the BEMC, EEMC, BBC, EPD, VPD, ZDC, TOF or MTD to provide

signals that have a high probability from coming from a physics process of interest. These triggers can be as simple as the ZDC or VPD saying "an event has occurred," or as specialized as trying to select on the production of specific particles, or identifying jet production using the calorimeters. The rate of these triggers can also be scaled, so that very frequent triggers do not saturate the bandwidth of the detector and inhibit other triggers. In this analysis we use a BEMC high-tower trigger (requires a single tower with large E_T) to select events with a high probability of containing a jet. We also use minimum-bias events selected with the VPD.

5 DATA SELECTION

"Choose from these ere we go, and may they serve you well!"

– J.R.R. Tolkien, *The Lord of the Rings*

Both the di-jet hadron correlations and the differential di-jet imbalance measurement use the same datasets, similar quality cuts, and similar jetfinding techniques. Therefore, to reduce repetition, methods that are common to both analyses are presented here. Any details specific to the di-jet hadron correlations or the differential di-jet imbalance will be presented in Chapter 6 or Chapter 7, respectively.

The results presented in this thesis come from two datasets: Au+Au collisions at $\sqrt{s_{\mathrm{NN}}} =$ 200 GeV recorded in 2007, and $p+p$ collisions at $\sqrt{s_{\mathrm{NN}}} = 200$ GeV recorded in 2006, with recorded luminosities of 1.12 nb^{-1} and 11.3 nb^{-1} respectively. We use charged tracks reconstructed by the TPC, as well as the neutral energy recorded in the BEMC for both analyses. The relevant selections and quality cuts for events, tracks, and towers are explained in the following sections.

Newer STAR datasets were considered to replace Run 7 with higher statistics. Run 11 was considered, but after extensive quality analysis, significant problems with the TPC were identified that reduced its total useable statistics to be only equivalent to Run 7 (See Appendix B). New data collected in 2014 was also intended to replace Run 7 as our primary Au+Au dataset. However, the Run 14 data had several issues regarding tracking and reconstruction that prevented it from being used as a replacement without significant QA from myself and multiple bug fixes in the reconstruction framework by the STAR software team. These are enumerated below in Section 5.5, and in more detail in Appendix C.

5.1 Event selection

The data analyzed in both Au+Au and $p+p$ were selected using a high-tower (HT) trigger, which requires a certain amount of energy (in this case, 5.4 or 5.5 GeV in $p+p$ and Au+Au, respectively [81, 82]) in a single calorimeter tower. This trigger is used to collect a large sample of events that contain a high-p_{T} track, and are therefore more likely to contain

jets.

Some minimal event quality cuts are applied to select events that are relatively uniform and reduce background signals, biases, and the inclusion of unphysical signals due to detector uncertainties or malfunctions. The primary vertex of the collision is required to be within 30 cm of the nominal center of the detector; this keeps the tracking efficiency in the TPC, as well as the effective track and tower η acceptance, relatively uniform. We also do not consider events with a track that has a reconstructed $p_{\mathrm{T}} > 30.0$ GeV/c, due to poor momentum resolution; in the STAR TPC (see Section 4.2.2), the track momentum resolution is about 2% at $p_{\mathrm{T}} = 0.5$ GeV/c, 7% at $p_{\mathrm{T}} = 3.5$ GeV/c, and grows approximately linearly over that range and into higher p_{T} ranges. To keep the cuts symmetric between tracks and towers, any event with a BEMC tower with $E_{\mathrm{T}} > 30.0$ GeV is also discarded.

In Au+Au collisions, only the 20% most central events are considered. In the 2007 data, the primary measure of centrality is the uncorrected charged particle multiplicity in the TPC within a single unit of rapidity: $|\eta| < 0.5$, with minimal track quality requirements. For a more detailed explanation of how the centrality is calculated for a STAR dataset, see Appendix D.

5.2 Track selection

Not all tracks reconstructed in an event come from the collision of interest, or are of high enough quality to be used for analysis. Because of the relative slowness of the TPC (due to the non-negligible time needed for electrons to drift through the detector volume, see Section 4.2.2), there can be tracks from multiple events read out in the same recording window if the collision rate is higher than the TPC read out rate. These "extra events" are called *pile-up* and must be removed before analysis. As an example, at the highest Au+Au collision rates recorded in the Run 14 data of about 100 kHz, there were, on average, seven events being recorded during each readout by the TPC. There are multiple ways of addressing pile-up, generally revolving around matching collision vertices or TPC tracks to fast detectors such as the VPD or the barrel TOF.

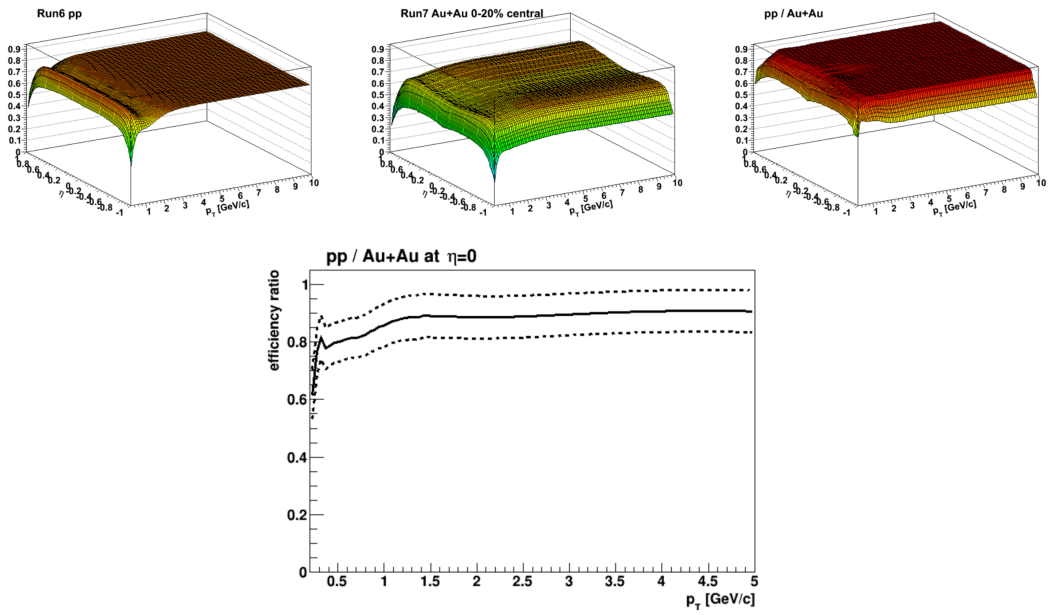

Figure 5.1: Left: Tracking efficiency of Run 6 p+p. Middle: Tracking efficiency of Run 7 Au+Au 0-20%. Right: Ratio of Run 7 / Run 6. Bottom: Ratio of Run 7 / Run 6 at $\eta = 0$. Dashed lines are the systematic uncertainty.

To enhance the quality of the tracks used, we only analyze primary tracks - tracks that were used in the cluster finder for the primary vertex, and are within 3 cm of the vertex - this significantly improves the momentum resolution of the track, and reduces background such as secondaries and pileup. Tracks are further required to have a global track DCA < 1 cm. To ensure that a track has a robust estimation of its kinematics, they are required to have at minimum 20 fit points, including the primary vertex. It is also required that the track have a majority of the fit points along its trajectory ($N_{\text{hits}}/N_{\text{hits}}^{\text{possible}} > 0.52$) - this eliminates the chance of a single physical track to be reconstructed as two "split" tracks.

Finally, tracks are required to have $|\eta| < 1.0$. This pseudorapidity cut ensures that each track has traversed the majority of both the inner and outer sector pad rows, and has a long enough trajectory through the TPC to be efficiently and accurately reconstructed.

5.2.1 Tracking efficiency

The TPC and the tracking algorithms used are not 100% efficient. This probability of successfully reconstructing a track depends on the geometry of the detector, the support structure, the current luminosity, the track geometry and the multiplicity of a given collision. To estimate the tracking efficiency of the STAR detector in a given environment, "known" Monte Carlo (MC) generated tracks are embedded into real events and the new event is reconstructed using the same software and reconstruction algorithms that the original data was processed with. The translation of Monte Carlo tracks into a realistic set of detector responses (TPC gas ionization, calorimeter energy deposits, interactions with support structures, etc) is done using GEANT-3 [83] and STAR-specific software to model the TPC response to the passing of an ionizing track, called the TPC response simulator (TRS). Once the event has passed through the complete STAR reconstruction chain, the efficiency can be calculated as the ratio of reconstructed to injected MC tracks using the same quality cuts that were used in the analysis. No embedding was done for the 2007 data, so the efficiencies were bootstrapped by comparing to Run 2004, where embedding was performed. The details of the efficiency calculations for both the Au+Au and $p+p$ data used in this analysis can be found in the references [84], and the resulting efficiencies and their ratio can be seen in Figure 5.1.

5.3 BEMC tower selection

Towers are individually calibrated for each run. Hardware errors, however, can lead to dead towers(towers that don't fire) or "hot" towers (towers that fire too frequently, or with bad ADC values). Finally, poor calibration can also lead to the ADC value from the PMT being translated into an incorrect E. To avoid unphysical signals, post-calibration analysis of the BEMC is performed on a tower-by-tower basis to find the dead, hot, or otherwise misbehaving towers, which are then removed from consideration for the entire run. This analysis was done by comparing the relative frequency that a tower recorded $E_{\mathrm{T}} > 0.2$ GeV, the $\langle E_{\mathrm{T}} \rangle$ of each tower, and the frequency that a tower recorded $E_{\mathrm{T}} > 2.0$ GeV, and removing

all outliers above or below some threshold.

To avoid any double-counting of energy between the TPC and the BEMC, we perform what is referred to as 100% hadronic correction, where any charged tracks that are extrapolated to a tower have their full p_T subtracted from the tower's transverse energy. This approach has been shown to be the most robust for the jet p_T momentum resolution [85]. Any tower with $E_T < 0$ after hadronic correction is set to zero.

5.4 Comparison of Au+Au to p+p

In both analyses the $p + p$ dataset is modified to match, as close as possible, the run conditions of the Au+Au so that jets and other measured physical quantities are directly comparable between the two without relying on unfolding techniques. The first step of this process is to simulate the large background energy density of an Au+Au event. To do this, the HT p+p data is embedded into minimum-bias (MB) Au+Au. This minimum-bias trigger only requires some energy to be deposited into the ZDCs, and therefore selects a sample that is representative of all heavy-ion collisions (approximately: the ZDC has relatively similar efficiency across all centralities). Unless otherwise specified, Au+Au MB data has the same event selection criteria as Au+Au HT.

To match the tracking efficiency between Au+Au and $p + p$, $p + p$ tracks are discarded randomly with a probability equal to one minus the ratio of the tracking efficiencies between the two datasets. This leaves the p+p event with an effective tracking efficiency equal to that of the Au+Au.

To accurately compare the calorimeter between the two datasets, the lists of hot and dead towers of Run 6 and Run 7 are combined so that both datasets removed the same set of towers, leading to a consistent BEMC geometry.

5.5 Run 14 Au+Au

The data collected in Run 14 has gone through multiple revisions to get to the most current production, labeled P18ih. The original production (labeled P16id) of the new data included the HFT (see Section 4.2.4) in the definition of all primary tracks whose geometry

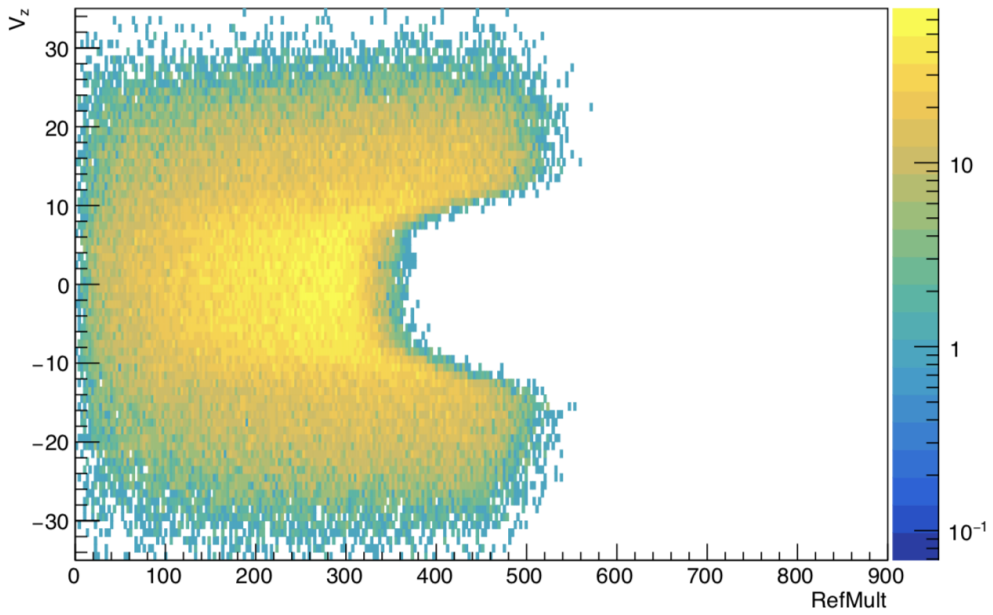

Figure 5.2: Significant reduction of tracking efficiency when the primary vertex is located inside the HFT ($|v_z| \leq\sim 6$ cm).

contained a possible HFT hit. I found this had a significant impact on the reconstruction efficiency, as demonstrated in Figure 5.2. For jetfinding unrelated to heavy-flavor physics, we do not need the high precision DCA measurements of the HFT, and benefit from having a uniform, high tracking efficiency and a large v_z acceptance to increase statistics. Because of this, a new production was requested from STAR that did not include the HFT in the tracking, so that the tracking efficiency was more consistent across v_z, and higher inside the HFT acceptance. The data was produced in 2017, and labeled P17id.

However, I found that this production had significant problems. First, the vertex-finder (VF) used to identify potential collision vertices produced a significantly larger number of candidates than in normal Au+Au datasets. This was found to be because the selected VF during reconstruction was optimized for $p + p$ collisions instead of Au+Au. This has minimal effect on the most central collisions where the "true" primary vertex is associated with hundreds of primary tracks, but it can have a significant impact on very peripheral events where the triggered primary vertex can have very few associated tracks.

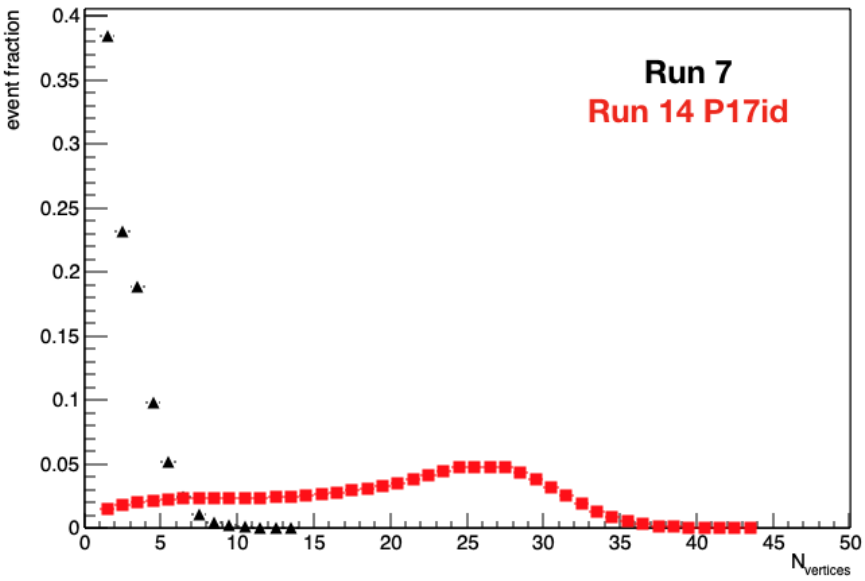

Figure 5.3: Number of vertices reconstructed in Run 7 and Run 14 with the P17id library. There is significant increase in the average number of candidate vertices due to the use of a $p+p$ optimized VF is seen when compared to Run 7.

There were also significant issues during reconstruction and embedding of the P17id production. As seen in Figure 5.4, the number of tracks reconstructed per event depends on the current version of the STAR reconstruction library being used. For our tracking efficiency calculations to work, the same reconstruction library must be used for the embedding data (from which we calculate the efficiencies) and the original dataset. Two bugs were found, one in the reconstruction code, and one in the embedding code. Together, these bugs made our efficiencies unusable, and required our dataset to be reproduced a second time, now labeled P18ih. This new production was finished in early in 2019. The QA, centrality definition and efficiencies are being currently in progress, and did not make it in time to be part of the results of this thesis.

For a more detailed explanation of the P17id QA, see Appendix C, and for more information on the centrality definition or tracking efficiencies, see Appendices D and E, respectively.

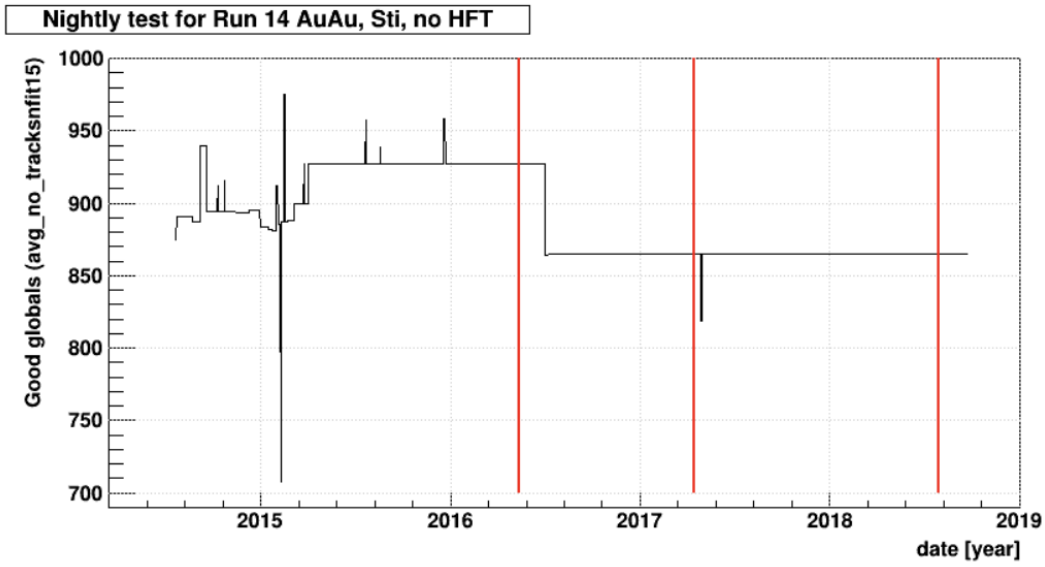

Figure 5.4: Number of tracks reconstructed in the same sample of events as a function of time. Variations are due to changes in the star reconstruction code. The red lines indicate when new production versions of the STAR library were released [86].

6 DIJET-HADRON CORRELATIONS

"It does not do to leave a live dragon out of your calculations, if you live near him."

– J.R.R. Tolkien, *The Hobbit*

The STAR di-jet imbalance measurement shown in Section 3.4 introduced the quantity $A_J = \Delta p_{\mathrm{T}}/\Sigma p_{\mathrm{T}}$, which is a measure of the relative transverse momentum imbalance of a di-jet pair. Because the partons undergoing a hard scattering have $p_{||} \gg p_{\mathrm{T}}$, the resulting jets are expected to have almost equal and opposite transverse momenta. In $p+p$, any significant broadening of this distribution can be attributed to radiation outside the jet cone, and any further broadening measured in heavy-ion collisions with respect to the $p+p$ result can then be attributed to the presence of a QGP. This comparison of Au+Au to $p+p$ thus gives a method of directly measuring the presence of QGP interactions on jets, providing a useful probe of the medium. The STAR A_J results highlight a set of hard-core di-jets (as defined in Section 3.3) that experience significant modification of the hard-core ($p_{\mathrm{T}}^{\mathrm{const}} > 2.0$ GeV), but where the radiated energy is contained within a narrow cone of $R = 0.4$ [61]. However, the A_J observable does not distinguish which of the jets in the event (or both) lost energy, and does not give direct access to the broadening and softening of the jet. To quantify the modification of these hard-core selected di-jets, a measurement similar to the jet-hadron correlations, introduced in Section 3.4, can be performed, which can give direct access to the broadening and softening of jets at the ensemble level, integrated over all A_J.

Hadron correlations have been used before with success at STAR to study the phenomena of jet quenching. The original di-hadron correlations discussed in Section 2.2.3 showed an essentially complete suppression of high-p_{T} hadrons in the average recoiling jet when compared to $p+p$, indicating very strong quenching [45]. With the advent of jetfinding techniques in heavy-ion collisions, the jet-hadron correlations extended the kinematic range available for the trigger and quantified the amount of energy that was redistributed within the recoil jet constituents compared to $p+p$ using the $\mathrm{D_{AA}}(p_{\mathrm{T}}^{\mathrm{assoc}})$ and $\Sigma\mathrm{D_{AA}}(p_{\mathrm{T}}^{\mathrm{assoc}})$ observables [58].

This analysis of the di-jet hadron correlations follows a similar procedure to the jet-hadron correlations, but with some significant changes to methodology, including the measurement of complete 2D angular correlations in $\Delta\eta$ and $\Delta\phi$ between the di-jets and associated charged hadrons, measurement of the yield, Y, as a function of $\langle p_{\mathrm{T}}^{\mathrm{assoc}} \rangle$ in both $\Delta\eta$ and $\Delta\phi$, use of a mixed-event acceptance correction, and a flow-agnostic background subtraction method that removes the necessity of calculating the event plane and estimating individual v_n components (See Section 2.1.4 for information on flow).

6.1 Data selection

Data selection follows the procedure explained in Chapter 5, comparing the most central 20% of Au+Au collisions to $p + p$ jets. While charged tracks and calorimeter towers are used for jetfinding, only charged tracks are considered for the correlations and yields. This is because a large fraction of low-E_{T} towers are photons from decayed π^0s, so towers can't be used in the correlations without first doing π^0 reconstruction, or else the associated p_{T} bins are not equivalent between the TPC and BEMC.

To effectively match the jet energy scale between Au+Au and p+p, the p+p is embedded into minimum-bias Au+Au events of the same centrality class as the triggered Au+Au sample. As discussed in Chapter 5, the TPC has significantly different tracking efficiency in central Au+Au collisions compared to $p + p$ collisions. To account for this, $p + p$ tracks are randomly discarded so that $p + p$ events have the effective efficiency of the central Au+Au events, so all jetfinding is done at the effective Au+Au jet energy scale. For details, see Section 5.4. This embedding is only done during jetfinding, and is not used when calculating the correlations; instead, the correlations are fully corrected for detector effects and reported at the particle level for both Au+Au and $p + p$.

Because there is a slight difference in the online trigger requirement between the Au+Au and $p + p$ data (a single tower with transverse energy above 5.5 or 5.4 GeV, respectively), a further offline trigger is required during analysis. For each event, a single tower is required to have $E_{\mathrm{T}} > 6.0$ GeV. This threshold was chosen to be far enough away from both online

thresholds to avoid any potential calibration effects that could affect the comparison. The same offline trigger threshold was applied in the jet-hadron correlation analysis [45].

6.2 Jetfinding and di-jet definition

This analysis was originally performed to study the internal structure of the di-jets found in the STAR A_J paper, and as such uses a di-jet trigger definition that almost exactly matches the one used in the A_J result. For both Au+Au and embedded $p+p$, hard-core di-jets are found using charged and neutral constituents with $p_{\mathrm{T}} > 2.0$ GeV/c using the anti-k_t jetfinder with a jet resolution parameter of $R = 0.4$. The leading jet is required to have $p_{\mathrm{T}} > 20.0$ GeV/c, and the subleading jet is required to have $p_{\mathrm{T}} > 10.0$ GeV/c. The hard-core jets are also required to be back-to-back in azimuthal angle ($|\Delta\phi^{\mathrm{dijets}}| > \pi - 0.4$, where $|\Delta\phi^{\mathrm{dijets}}| = |\phi^{\mathrm{trigger}} - \phi^{\mathrm{recoil}}|$). Once an event has an accepted hard-core di-jet pair, the event is reclustered with all constituents down to $p_{\mathrm{T}} > 0.2$ GeV/c, and the jets are matched geometrically to the hard-core jets by taking the closest matched jet to the hard-core jet axis in angular distance ($\Delta\mathcal{R} = \sqrt{\Delta\phi^2 + \Delta\eta^2}$, where $\Delta\phi = \phi^{\mathrm{jet}}_{\mathrm{hard-core}} - \phi^{\mathrm{jet}}_{\mathrm{matched}}$ and $\Delta\eta = \eta^{\mathrm{jet}}_{\mathrm{hard-core}} - \eta^{\mathrm{jet}}_{\mathrm{matched}}$). After matching, leading and subleading jets are still defined by the hard-core jets, so it is possible that $p_{\mathrm{T}}^{\mathrm{sublead}} > p_{\mathrm{T}}^{\mathrm{lead}}$.

Because there is a high energy calorimeter trigger required in at least one jet, there is a significant bias in both the neutral energy fraction of the jet, and the fragmentation of the jet. Because of this, instead of calculating the yields with respect to the leading jet (highest p_{T}) and subleading jet (second highest p_{T}), we instead perform the correlations with respect to the trigger jet and the recoil jet, where the trigger jet contains the BEMC trigger tower. If neither jet contains the trigger tower, the event is discarded, and if both towers contain a trigger, the highest p_{T} jet is considered the trigger jet.

The use of the term trigger can lead to confusion, due to the presence of an online trigger during data-taking, the offline trigger required in each event, and the traditional use of the term "trigger" to define the object with which associated objects are correlated in the correlation function. From now on, any discussion of a "trigger" will refer to the BEMC

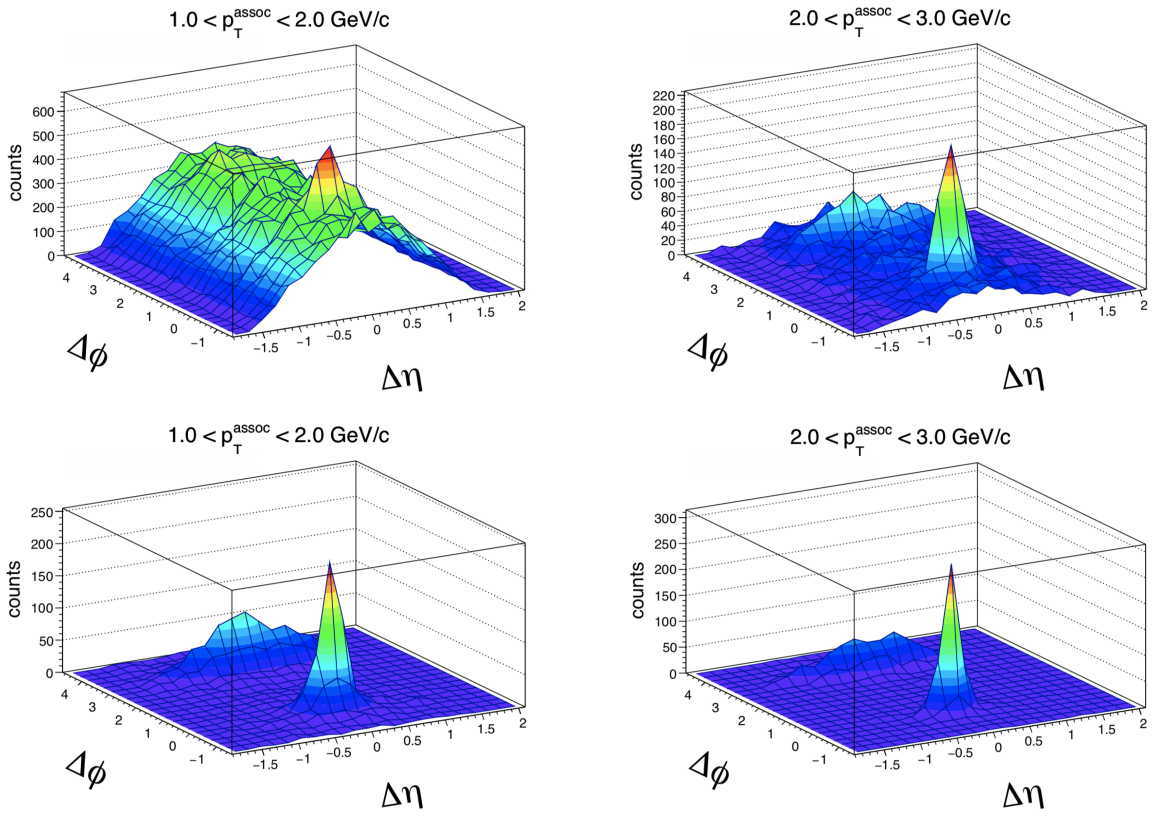

Figure 6.1: Raw di-jet hadron correlations with respect to the trigger jet. Top: Au+Au correlations for $1.0 < p_{\mathrm{T}}^{\mathrm{assoc}} < 2.0$ GeV/c (left) and $2.0 < p_{\mathrm{T}}^{\mathrm{assoc}} < 3.0$ GeV/c (right) Bottom: $p+p$ correlations for $1.0 < p_{\mathrm{T}}^{\mathrm{assoc}} < 2.0$ GeV/c (left) and $2.0 < p_{\mathrm{T}}^{\mathrm{assoc}} < 3.0$ GeV/c (right).

trigger object used to initially select the event, and "trigger jet" and "recoil jet" will refer to the two trigger objects used to measure the correlation functions.

6.3 Measurement of the correlation function

Once a di-jet has been found, all the associated charged tracks in the trigger event are correlated with the trigger and recoil jet axes separately in two angular dimensions ($\Delta\eta = \eta^{\mathrm{jet}} - \eta^{\mathrm{assoc}}$, $\Delta\phi = \phi^{\mathrm{jet}} - \phi^{\mathrm{assoc}}$), as a function of $p_{\mathrm{T}}^{\mathrm{assoc}}$ separately. This means that the signal of interest in the correlations is always located around the point $\Delta\eta \approx 0.0$, $\Delta\phi \approx 0.0$, for both the trigger jet and recoil jet. The correlations are weighted track-by-track by the inverse of the tracking efficiency of the TPC. This produces two 2D correlations that are efficiency corrected, allowing the extraction of yields that are fully corrected for

detector effects. Because of the lack of statistics and a small signal relative to background, the associated p_{T} is restricted to be above 1 GeV/c. An example of the raw correlations is shown in Figure 6.1.

6.4 Mixed event correction

In the correlations shown in Figure 6.1, there is a significant triangular shape along $\Delta\eta$. This is not caused by jet or heavy-ion physics. Instead, it is an artifact from the limited acceptance of the detector. Because the detector only covers the pseudorapidity range $|\eta| < 1.0$, there is a maximal $\Delta\eta$ value the trigger jet and the associated tracks can have: $|\Delta\eta|_{\mathrm{max}} = 2.0 - R = 1.6$. Furthermore, it is much less likely to have a very large $\Delta\eta$ value for any jet/track pair than it is to have a small value, not because of the physics of the collision but because there is only a single configuration of jet and track that leads to a $\Delta\eta = \pm 1.6$, whereas there are many configurations that lead to $\Delta\eta \approx 0.0$. Because of this, a measurement of the correlation in $\Delta\eta$ that contains no physical correlation between the jet and the associated hadrons will still produce a strong pyramidal shape.

This "acceptance effect" can be corrected to produce signal correlations that are flat in $\Delta\eta$ in the absence of any physical correlation. To do this, a "mixed event" correlation is prepared by placing an already found di-jet 4-vector from the high-tower data (Au+Au and p+p) into uncorrelated events and performing the 2D correlations in $\Delta\eta$ and $\Delta\phi$ between the embedded jet and the uncorrelated event. This produces a background that contains the same acceptance effect as the signal correlation, as well as any effects from detector inefficiencies, but without any physical correlations between the jet and the associated charged hadrons. Dividing the signal correlation function by the mixed event correlation then "corrects" the correlation for the finite $\Delta\eta$ acceptance.

Because of a lack of statistics in the minimum-bias 0-20% central Au+Au data and $p+p$ min-bias data, the di-jets are embedded into high-tower events. To minimize the effect of jets in the embedding event, only events where no hard-core jet with $p_{\mathrm{T}} > 16.0$ GeV/c was found are considered.

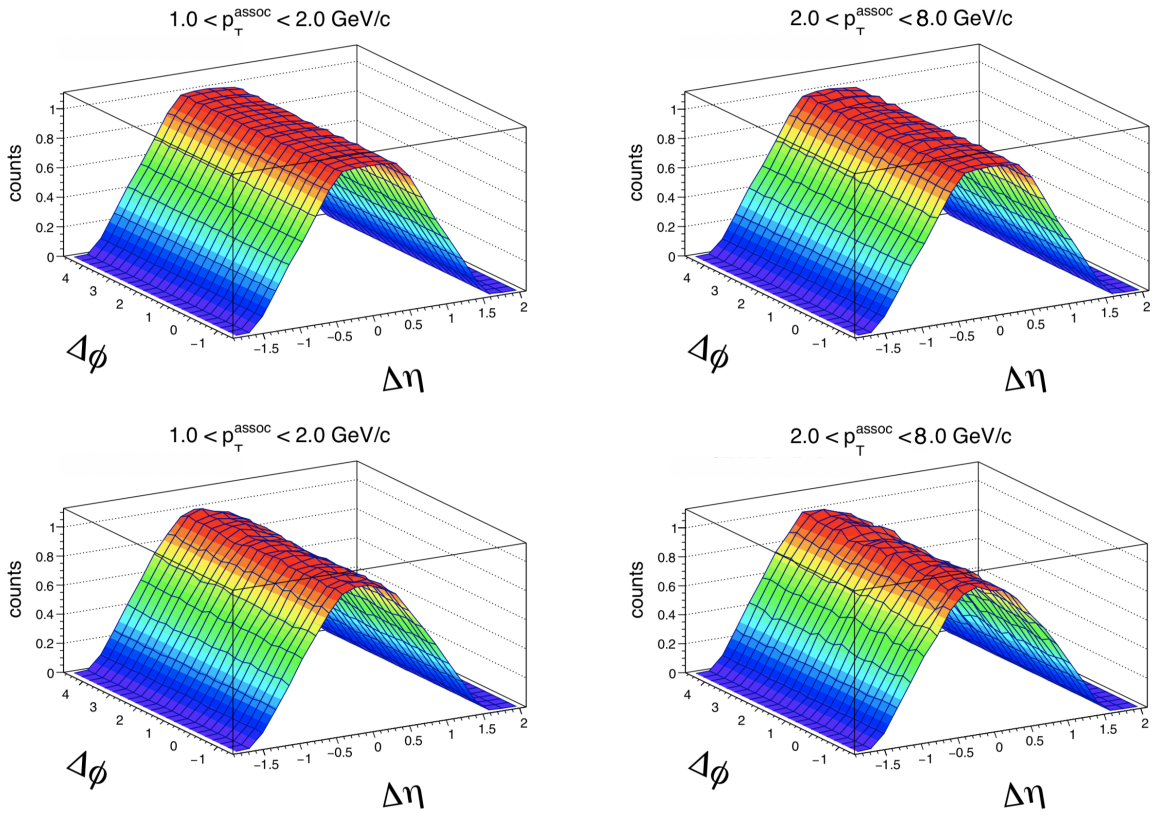

Figure 6.2: Event mixing di-jet hadron correlations with respect to the trigger jet.Top: Au+Au correlations for $1.0 < p_{\mathrm{T}}^{\mathrm{assoc}} < 2.0$ GeV/c (left) and $2.0 < p_{\mathrm{T}}^{\mathrm{assoc}} < 8.0$ GeV/c (right) Bottom: $p + p$ correlations for $1.0 < p_{\mathrm{T}}^{\mathrm{assoc}} < 2.0$ GeV/c (left) and $2.0 < p_{\mathrm{T}}^{\mathrm{assoc}} < 8.0$ GeV/c (right).

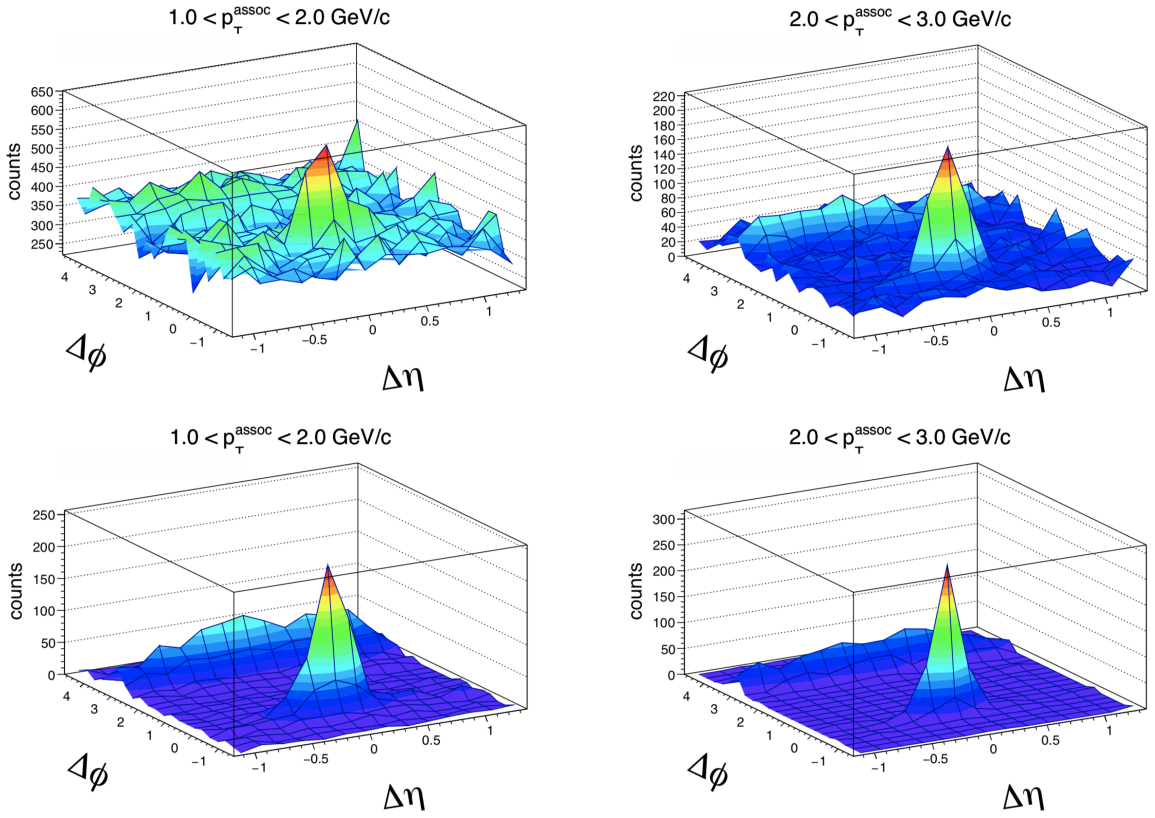

Figure 6.3: Event mixing corrected di-jet hadron correlations with respect to the trigger jet.Top: Au+Au correlations for $1.0 < p_{\mathrm{T}}^{\mathrm{assoc}} < 2.0$ GeV/c (left) and $2.0 < p_{\mathrm{T}}^{\mathrm{assoc}} < 3.0$ GeV/c (right) Bottom: $p+p$ correlations for $1.0 < p_{\mathrm{T}}^{\mathrm{assoc}} < 2.0$ GeV/c (left) and $2.0 < p_{\mathrm{T}}^{\mathrm{assoc}} < 3.0$ GeV/c (right).

The event mixing is done in bins of v_z because the effective track η range changes as a function of the primary vertex position. The event mixing is also done in bins of centrality to match the detector conditions and acceptance of the signal events. Because of the lack of statistics, instead of correcting each (v_z, centrality) bin individually, a weighted average of the (v_z, centrality) bins is created. Furthermore, all $p_{\mathrm{T}}^{\mathrm{assoc}}$ bins above 2.0 GeV/c are combined because the tracking efficiency is approximately constant (See Figure 5.1).

The averaged mixed event correlations are normalized so that the maximum bin in the $\Delta\eta$ projection has a bin content of $1.0/N_{\phi}^{\mathrm{bins}}$. The final mixed event histograms are shown in Figure 6.2.

The acceptance-effect-corrected signal correlations are produced by dividing the signal histogram by the normalized mixed event correlations. The results are shown in Figure 6.3.

6.5 Background subtraction

To extract the yield associated with the jet from the correlation function, the background from the underlying event must be estimated and subtracted. This background, however, may not be completely uncorrelated with the jet, because there is some correlation between the jet axis and the event plane; high-p_{T} charged hadrons, produced from jets, are found to have significant v_2 [39, 87]. To handle the case of non-zero jet v_n in $\Delta\phi$, a side-band subtraction method is used, whereas in $\Delta\eta$ the background is assumed to be flat (this requires flow to be independent of $\Delta\eta$ in the kinematic region of interest, which has been verified [39, 87]).

6.5.1 $\Delta\eta$

One-dimensional $\Delta\eta$ projections are extracted from the two dimensional correlations for all $p_{\mathrm{T}}^{\mathrm{assoc}}$ bins for both trigger and recoil jets by projecting over the region $|\Delta\phi| < 0.71$. To account for the large background contribution in low-$p_{\mathrm{T}}^{\mathrm{assoc}}$ bins, background subtraction is performed by fitting a gaussian and a constant to the resulting distribution and subtracting the constant term from each bin. Again, flow is assumed to be independent of $\Delta\eta$, allowing the constant background subtraction. The projection region is visualized on the left side of

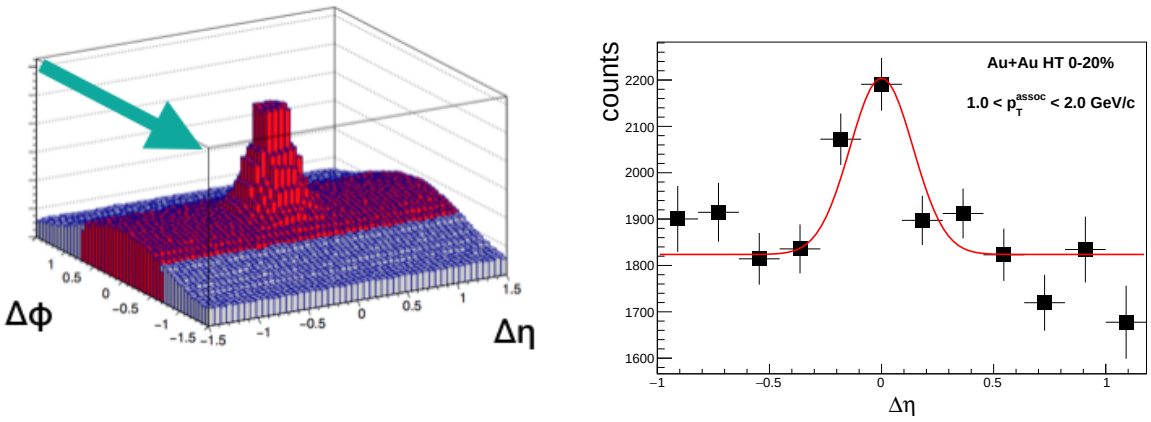

Figure 6.4: Example of background estimation for $\Delta\eta$. Left: Visualization of the projection region for $\Delta\eta$ ($|\Delta\phi| < 0.71$). Right: Example projection with the gaussian+constant fit.

Figure 6.4 with an example projection for a single p_{T} bin from data shown on the right.

6.5.2 $\Delta\phi$

One dimensional $\Delta\phi$ correlations for both trigger and recoil jets for all $p_{\mathrm{T}}^{\mathrm{assoc}}$ are extracted from the 2D correlations. To account for the large background contribution in low-$p_{\mathrm{T}}^{\mathrm{assoc}}$ bins, and any possible correlation between the jet and the underlying event (jet flow, etc), background is subtracted using the side band method. This method assumes all flow components (v_n) are $\Delta\eta$ independent. The correction is done by taking the projection over the signal region, $|\Delta\eta| < 0.45$, and subtracting from that the side band region, $0.45 < |\Delta\eta| < 1.0$. The signal and side band projection regions are visualized in Figure 6.5 with an example projection for a single p_{T} bin on the right.

6.6 Systematic uncertainties

Two sources of systematic errors were considered for the relative jet energy scale between Au+Au and p+p. We must account for the time dependence of both the TPC and the BEMC (Au+Au was recorded in 2007, $p+p$ in 2006), which includes the relative tracking efficiency between Au+Au and $p+p$ ($90\% \pm 7\%$ for $p_T > 2.0$ GeV/c) and the relative tower energy scale ($100\% \pm 2\%$). The effect from these uncertainties was assessed in the Au+Au MB embedded $p+p$. For ease of notation I will introduce $(\pm, \pm)$, where the first term represents

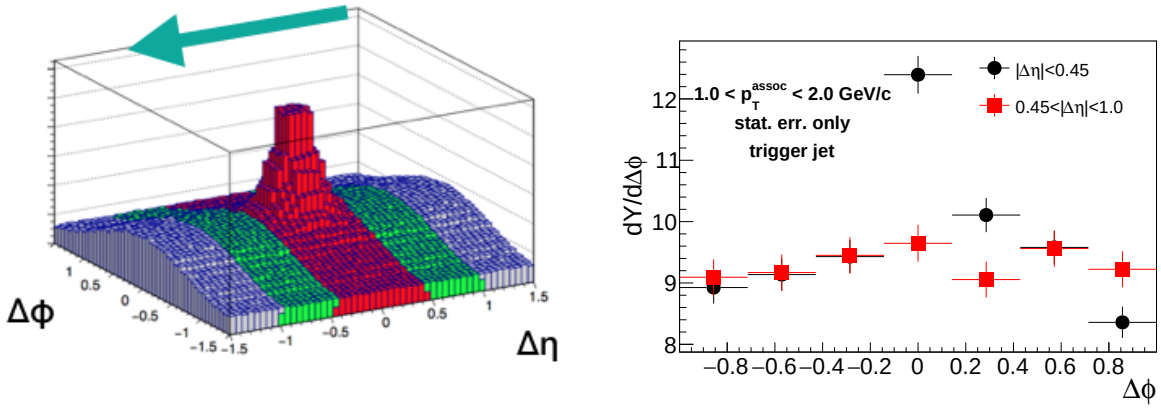

Figure 6.5: Example of the background estimation for $\Delta\phi$. Left: $\Delta\phi$ subtraction method signal projection region is over $|\Delta\eta| < 0.45$ (red), and the side band region is from $0.45 < |\Delta\eta| < 1.0$ (green). Right: Example projection of the signal and side band for a single p_{T} bin.

the variation of the relative TPC efficiency, and the second term represents the variation of the tower energy scale. Because the two subsystems are to leading order independent of each other (before hadronic correction), only the cases where both tracking efficiency and tower scale where higher or lower were analyzed ((+,+), (-,-)), not the cross terms ((+,-), (-,+)). The effect of the towers was estimated by scaling each calorimeter hit energy by two percent either positively or negatively. The relative tracking efficiency was then assessed by varying the probability of discarding tracks during jetfinding; the tracking efficiency used to correct the correlations and yields is not varied. The correction to individual bins in $\Delta\eta$ and $\Delta\phi$ correlations are calculated as the difference between the corresponding (+,+) and (-,-) projections. The uncertainties on the yields are calculated by performing the projection and integration over the corresponding $p_{\mathrm{T}}^{\mathrm{assoc}}$ bin for (+,+) and (-,-) and taking the difference to be the systematic uncertainty. An example of the effect of the tower energy scale uncertainty and relative tracking efficiency uncertainty on the correlations are shown in Figure 6.6.

A third systematic uncertainty is applied to the correlations and yields. The absolute uncertainty on the TPC tracking efficiency is taken to be 5%, which accounts for any systematic uncertainty in the embedding used to estimate the efficiencies, as discussed in Section 5.2.1.

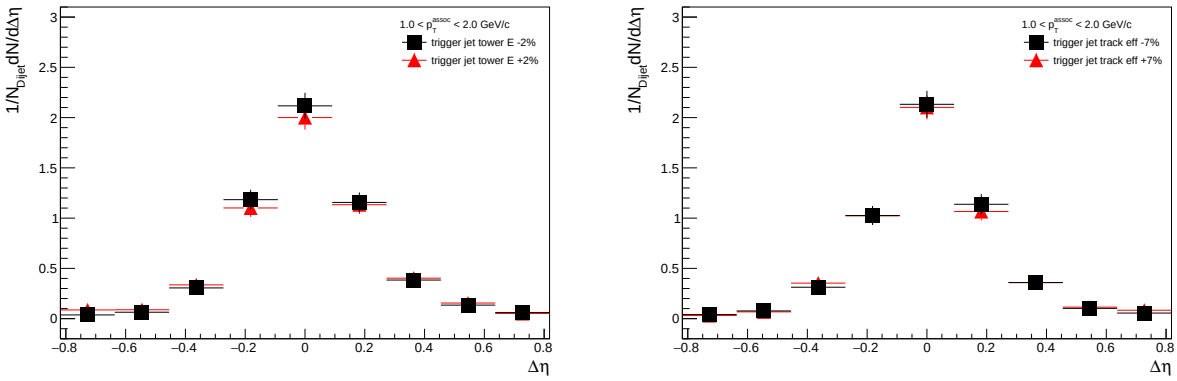

Figure 6.6: Examples of the effect of the jet energy scale systematic variations on the trigger jet hadron correlations for $1.0 < p_{\mathrm{T}}^{\mathrm{assoc}} < 2.0$ GeV/c. Left: Effect of varying the tower energy scale by $\pm 2\%$ during jetfinding. Right: Effect of varying the relative tracking efficiency by $\pm 7\%$ during jetfinding.

Examples of the tracking efficiency uncertainty are not shown because they are just a multiple of the bin content.

6.7 $\Delta\eta$, $\Delta\phi$ Correlation functions

After background subtraction, the correlations are compared between Au+Au and $p+p$. They are shown below, split into $\Delta\eta$ and $\Delta\phi$, for trigger and recoil jets in Figure 6.7, Figure 6.8, Figure 6.9, and Figure 6.9.

Qualitatively, the correlations have similar widths and magnitudes for the same $p_{\mathrm{T}}^{\mathrm{assoc}}$ bins, when comparing $\Delta\eta$ to $\Delta\phi$ correlations. However, we note that in general, the integral of the recoil jet correlations tends to be slightly higher in each $p_{\mathrm{T}}^{\mathrm{assoc}}$ bin compared to the trigger jet, which is consistent with the biased neutral energy fraction of the trigger jet due to the inclusion of the BEMC trigger requirement. The quantitative comparison of yields will be shown in the next section.

6.8 Correlated di-jet hadron yields

The yields are extracted from the correlations by summing over the 1D correlation histograms $Y(p_{\mathrm{T}}^{\mathrm{assoc}}) = \Sigma_X \mathrm{d}Y(p_{\mathrm{T}}^{\mathrm{assoc}})/\mathrm{d}X$, where X is either $\Delta\eta$ or $\Delta\phi$. The integration regions are chosen to exactly match the projection regions in the other dimension: for instance,

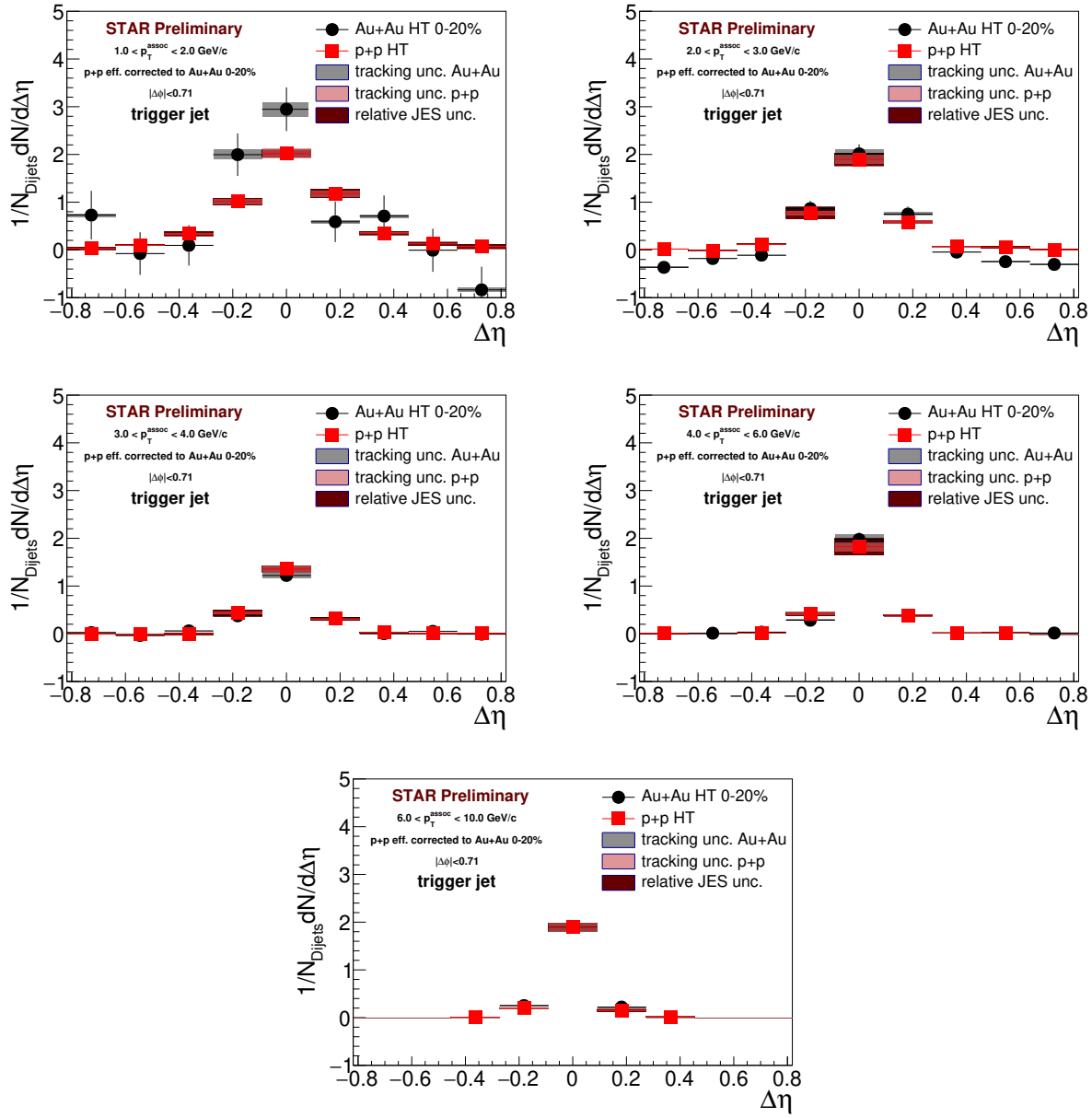

Figure 6.7: $\Delta\eta$ correlations for the trigger jet with associated charged hadrons.

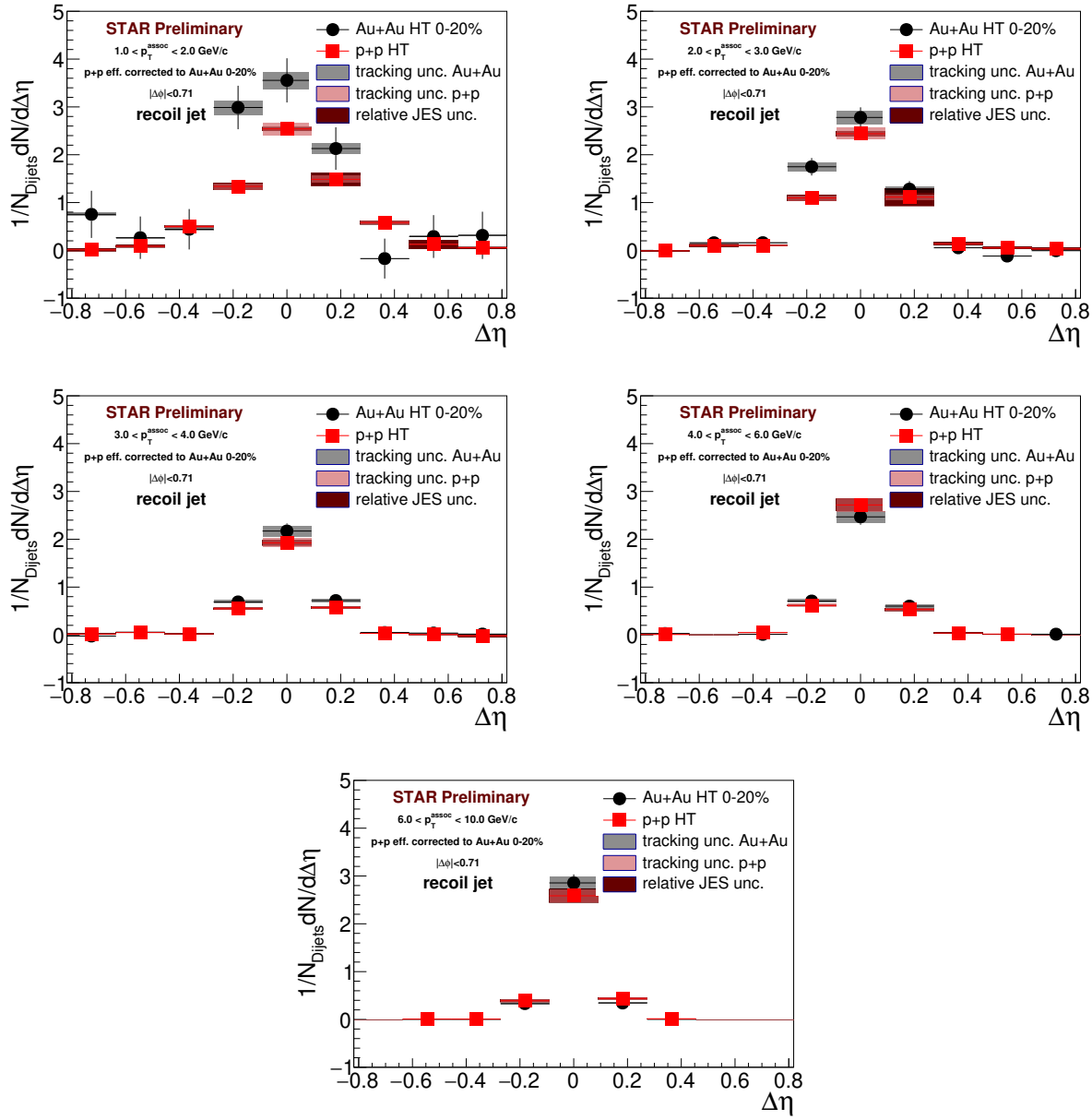

Figure 6.8: $\Delta\eta$ correlations for the recoil jet with associated charged hadrons.

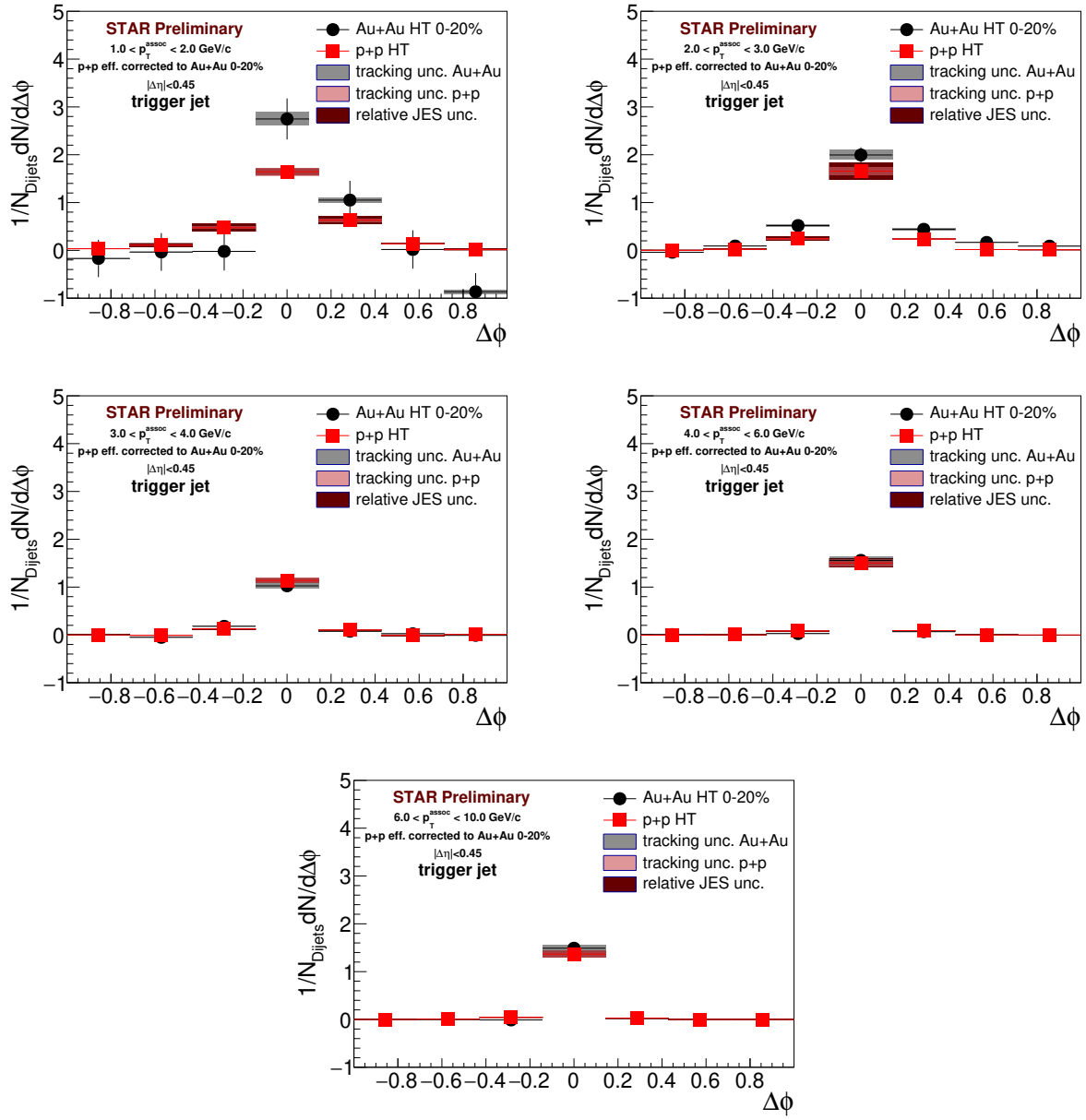

Figure 6.9: $\Delta\phi$ correlations for the trigger jet with associated charged hadrons.

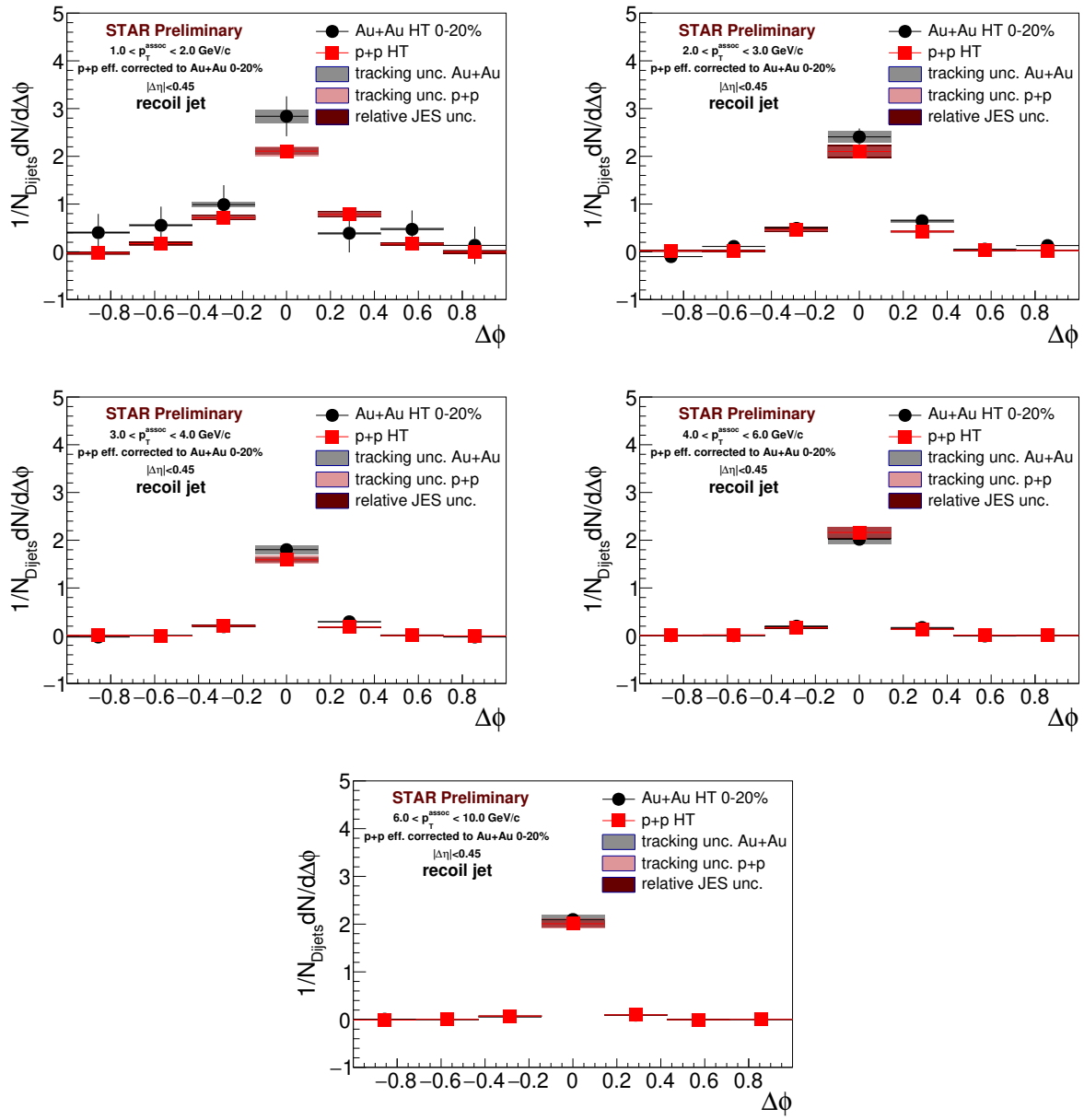

Figure 6.10: $\Delta\phi$ correlations for the recoil jet with associated charged hadrons.

since the $\Delta\eta$ correlations were projected over $|\Delta\phi| < 0.71$, the $\Delta\phi$ integration region is now $|\Delta\phi| < 0.71$ as well. And similarly, because the $\Delta\phi$ integration region (not including the side band) was $|\Delta\eta| < 0.45$, the $\Delta\eta$ integration region is taken to be $|\Delta\eta| < 0.45$. This gives a consistent 2D integration region in both dimensions, and allows the direct comparison of the yields between $\Delta\eta$ and $\Delta\phi$. Because the correlations are corrected for TPC tracking efficiency, the yields are fully corrected and Au+Au and $p+p$ yields can be compared at the particle level.

One correction has to be performed on the yields that was not performed on the correlations themselves. Because of the steeply falling jet spectrum, it is likely to find hard-core jets in both Au+Au and embedded $p+p$ where the jet had $p_{\mathrm{T}}^{\mathrm{jet}}$ less than the required threshold (20 GeV/c for the leading jet, 10 GeV/c for the subleading jet), but sat on top of a background constituent of 2 GeV/c or more. This effect is more significant in the trigger jet, and minimal in the recoil jet. This is due to the fact that once a trigger jet with $p_{\mathrm{T}} > 20$ GeV/c is found, it is significantly more likely to find a recoil jet with $p_{\mathrm{T}} > 10$ GeV/c, even with possible quenching effects.

However, under the assumption that the hard-core jets of the Au+Au and $p+p$ have a similar spectral shape in p_{T} (consistent with both the A_J and correlation results, and shown in the jet-hadron paper for the trigger jet [58]), the effect can be measured in the embedded $p+p$ and used to correct the Au+Au yield to the level of $p+p$, effectively removing the remaining "correlated background" that arises during jetfinding. This is done by finding the rate at which hard-core particles from the embedding event were found in the hard-core $p+p$ trigger or recoil jet. If that rate was above the normal background rate, then the yield of those particles was subtracted from the Au+Au yields.

The yields for the trigger jet are shown in Figure 6.11, and for the recoil jet in Figure 6.12. From the yields, we immediately see that on average, recoil jets contain more charged tracks in all but the highest $p_{\mathrm{T}}^{\mathrm{assoc}}$ bins. This is consistent with the trigger neutral energy fraction bias. We also see that the yields are consistent between $\Delta\eta$ and $\Delta\phi$. This is consistent with

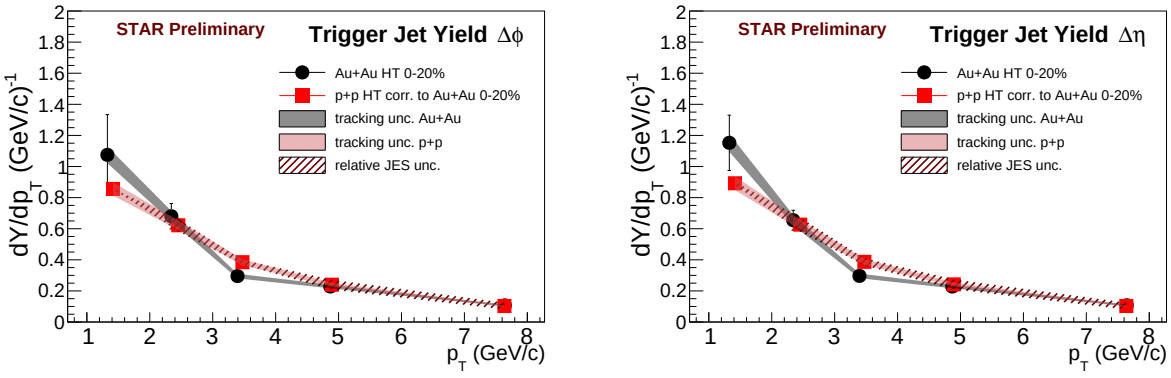

Figure 6.11: Trigger jet yields. Left: From $\Delta\phi$ correlations. Right: From $\Delta\eta$ correlations.

the fact that the correlations were narrow, and suggests that the entire jet was within our relatively narrow integration range. Otherwise, if there was significant jet energy outside the integration range, the different background subtraction methods would have led to significant differences in the yield between the two dimensions. These findings are consistent with and confirm the results of the A_J paper's findings, highlighting that the low-p_{T} associated yield is slightly broadened as can be seen in the 1D correlations, but contained within the jet cone.

Finally, comparing the Au+Au to $p+p$, we see that the trigger jet yield is consistent between the two datasets. In the recoil jet, however, while the hard-core part of the jet ($p_{\mathrm{T}}^{\mathrm{assoc}}$ >2.0 GeV/c) has consistent yields between Au+Au and $p+p$, the associated particles below the 2.0 GeV/c threshold appear to be slightly enhanced in Au+Au compared to $p+p$, consistent with medium modification.

6.9 Conclusions

In the di-jet hadron correlations, Au+Au hard-core di-jets appear to be minimally modified when compared to a $p+p$ reference, except for some slight enhancement in the soft constituents - mainly in the recoil jet. We see in the correlations that there is some broadening of the lowest p_{T} bin in Au+Au with respect to $p+p$, which is consistent with the A_J measurement, where the radiated energy was recovered within a cone of $R = 0.4$.

The minimal modification of the hard-core yields of the di-jet can be naively difficult to

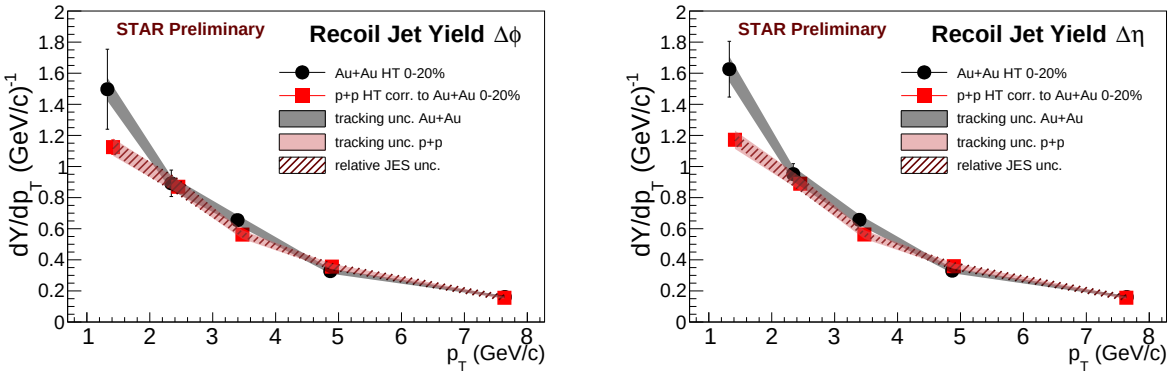

Figure 6.12: Recoil jet yields. Left: From $\Delta\phi$ correlations. Right: From $\Delta\eta$ correlations.

understand when contrasted with the results of the STAR A_J measurement, where significant modification of the hard-core was observed. However, there are two important differences between a measurement like the di-jet imbalance and the di-jet hadron correlations.

Firstly, the correlations (and thus, the yields) are an ensemble-level quantity averaged over all A_J, whereas the A_J is measured per di-jet. Because of this, a small number of modified events can show up statistically significantly in the A_J distributions without having a large effect on the average jet yields, which can still appear relatively vacuum-like because the majority of events show minimal modification.

A more subtle effect that would be more difficult to quantify in the di-jet hadron correlations and the corresponding yields is that the A_J quantity depends explicitly on the relative balance between each di-jet pair in every event, whereas in the di-jet hadron correlations, the trigger and recoil jet are effectively de-coupled. Therefore, it is possible for trigger jet and recoil jet populations to look relatively similar between the Au+Au and $p+p$ datasets, but be combined in such a way as to produce significantly different A_J distributions.

Which of these effects (or others not mentioned) contributed to the differences have not been explored yet - however, the upcoming Run 14 dataset has a large enough increase in statistics to allow the study of the di-jet imbalance and the correlations in more detail. A few interesting measurements, such as the di-jet hadron correlations as a function of A_J,

or the di-jet hadron correlations as a function of $\Delta A_J = A_J^{\text{hard-core}} - A_J^{\text{matched}}$ will provide an opportunity to study different populations of di-jets that may be more or less modified relative to the $p + p$ reference and help to isolate the effects of interest.

7 DIFFERENTIAL DI-JET IMBALANCE

"There are no safe paths in this part of the world. Remember you are all over the Edge of the Wild now, and in for all sorts of fun wherever you go."

– J.R.R. Tolkien, *The Hobbit*

The di-jet hadron correlations explored the medium modification of the STAR hard-core di-jets as defined in the di-jet imbalance measurement (Section 3.4), and found that both the average trigger and recoil jets looked relatively vacuum-like, showing much less modification than the recoil jets studied in the jet-hadron correlations, where a significant suppression was found for $p_{\mathrm{T}}^{\mathrm{assoc}} > 2.0$ GeV/c, coupled with a large enhancement for $p_{\mathrm{T}}^{\mathrm{assoc}} < 2.0$ GeV/c. While there is a slight difference in trigger jet kinematics between the jet-hadron and di-jet hadron correlations, the major difference is the presence of the second hard-core jet, the subleading jet, in the di-jet analysis. This shows that the presence of the hard-core recoil jet is significantly biasing the event selection when compared to the measurement when back-to-back jets are not required.

The goal of the differential di-jet imbalance measurement is to expand on the original STAR A_J results by systematically varying the di-jet definition, and measuring the effect the variations have on the resulting balance or imbalance when compared to a $p+p$ reference, and inferring from this the bias that is introduced by the hard-core jet definition. Until this point, the discussion of what "bias" is being referred to has not been well defined. These jet-like trigger object biases lead to a bias of the fragmentation of the jet (for hard-core jets, we select jets with a hard fragmentation pattern). A more detailed discussion, and how this fragmentation can be related to a path length bias in the medium will be given in Section 7.1.

The observable used is the absolute value of the di-jet asymmetry, defined as

$$|A_J| = \frac{|p_{\mathrm{T}}^{\mathrm{lead}} - p_{\mathrm{T}}^{\mathrm{sublead}}|}{p_{\mathrm{T}}^{\mathrm{lead}} + p_{\mathrm{T}}^{\mathrm{sublead}}} \quad , \tag{7.1}$$

where the absolute value is used to make visual comparison easier, and does not change the results of the measurement. The $|A_J|$ is calculated for embedded $p+p$ and Au+Au hard-core

and matched di-jets.

To make a quantitative measure of the similarity between the $p+p$ reference and the Au+Au, the Kolmogorov-Smirnov (KS) test of similarity is used [88, 89]. The test is defined as the maximum distance between the empirical cumulative distribution functions. This distance is converted into a probability via a function that depends on the number of entries in both datasets. The probability is much less than one if the two datasets are sampled from different probability density functions (PDFs), and randomly distributed between 0 and 1 if the two datasets are sampled from the same PDF. For all comparisons, a binned KS test is used, but the number of histogram bins is chosen to be larger than the number of data points, to minimize the chance of over-estimation of the test statistic.

7.1 Jet-like biases in heavy-ion collisions

In a collider experiment, the inclusion of specialized triggers during data-taking is used to enhance the probability of recording certain types of events when only a fraction of the total events can be recorded. Triggers are used for identifying events with rare decays, jets, or simply the presence of a collision. These triggers are introduced for multiple reasons; at STAR, data taking rate is limited primarily by the TPC's slow electron drift velocity. Electrons from a mid-rapidity track can take up to 42 μs to cross the gas volume, whereas RHIC can deliver collisions at around 100 kHz at maximum luminosity. Because the TPC is not designed for continuous readout, this drift speed puts a limit on how fast events can be recorded.

Whatever the cause, these trigger selections necessarily select a sample of events that is not representative of the inclusive event sample. The jet trigger we use at STAR in heavy-ion collisions, for instance, is a high-tower trigger. This trigger requires a single calorimeter tower to record a large amount of energy (generally $E_{\mathrm{T}} > 5.4$ GeV). Therefore the trigger preferentially selects events with a very high energy π^0 or γ, leading to a significant fragmentation bias in the jets that are selected by this trigger. This fragmentation bias is the primary cause of the charged hadron yields in the di-jet hadron correlations in Section 6.8

being systematically lower in the trigger jet than the recoil jet, even in the highest p_{T} ranges, because a large amount of the average trigger-jet's energy is found in a single neutral constituent.

Further biases are introduced during jetfinding in heavy-ion collisions. To positively identify jets from background fluctuations, many analyses require jets to have some $p_{\mathrm{T}}^{\mathrm{min}}$ that is significantly larger than the background fluctuations, σA, or require a jet-like fragmentation pattern, like the hard-core jet selection. However, medium modification can both soften the fragmentation pattern and lead to significant radiation outside the jet cone, effectively reducing the jet's reconstructed energy; because of the steeply falling jet spectrum, in particular at RHIC energies, there is a strong bias towards selecting low p_{T} jets that were minimally modified, instead of higher p_{T} jets that experienced significant quenching.

However, these biases have the potential to be useful tools to allow a more differential study of jet quenching and the properties of the medium itself. Because partonic energy loss depends explicitly on the path length the initiating parton travels through the medium (Section 2.2.1) [41], this suggests that when a jet is found, it has a higher probability of being produced close to the surface of the QGP and thus would experience less medium modification. The path length dependence of energy loss is balanced, however, by stochastic energy loss fluctuations. If fluctuations in the energy loss are significantly stronger than the path length dependence, it could nullify the path length bias effect. This has been explored in theoretical calculations at RHIC and LHC energies; an analysis showed that for the most central 10% of events at RHIC when either a high-E leading hadron or a hard-core jet is required, a significant surface bias is present for the originating hard-scattering vertex, whereas the distribution of all hard scatterings scales with the number of nucleon-nucleon binary collisions and is thus the most dense at the center of the collision, as seen in Figure 7.1 [90]. However at LHC energies the same calculation suggested that energy loss fluctuations would be the dominant effect, and predicted minimal path length bias due to high-p_{T} hadron triggers.

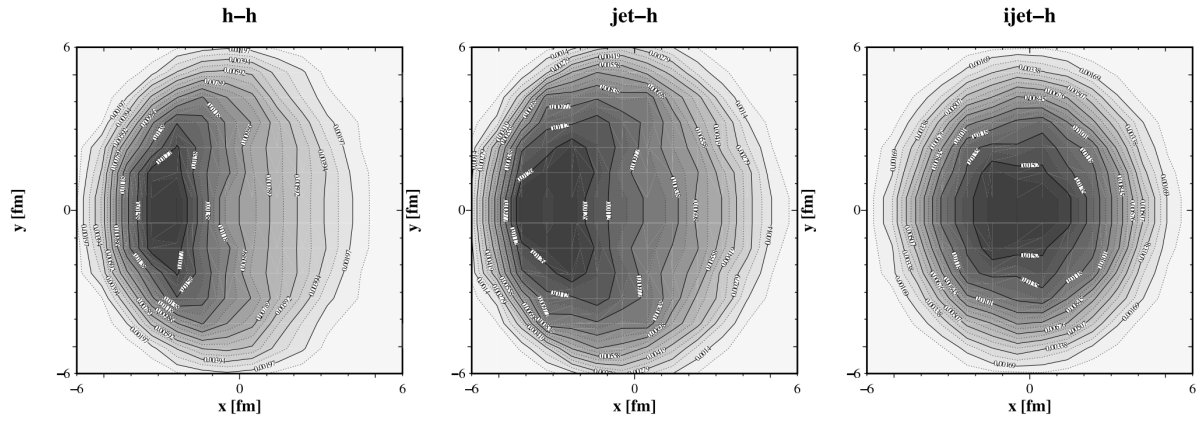

Figure 7.1: Path length biases introduced by various trigger definitions. Conditional distribution of production vertices in the transverse plane. Trigger object momentum is always along $-x$ axis. Trigger required to have $12 < E < 15$ GeV. Left: requiring a single hadron. Center: requiring a hard-core jet. Right: an "ideal" jetfinder (insensitive to modification) [90].

The goal of the differential di-jet imbalance measurement is to study the feasibility of using the hard-core di-jet selection to preferentially select more or less modified di-jets via control of the radius and hard-core constituent p_{T} cut parameters of the hard-core di-jet definition. If the amount of modification measured with respect to the $p+p$ reference varies significantly with the variation of the di-jet definition, then that would suggest a possible variation in the average path length of the di-jets with those changes in the definition. This would be the first step towards "jet geometry engineering", a term we use to describe the process of selecting di-jet samples that have a specific geometry with respect to the bulk of the heavy-ion collision. This would be achieved by controlling the path length of the di-jets either via selection of jet production vertices close to the surface of the fireball, or selecting di-jets that were produced tangentially to the QGP, significantly reducing the in-medium path length using these hard-core di-jet definitions or other bias-inducing criteria such as a high-p_{T} leading hadron. A visual depiction of jet geometry engineering can be seen in Figure 7.2.

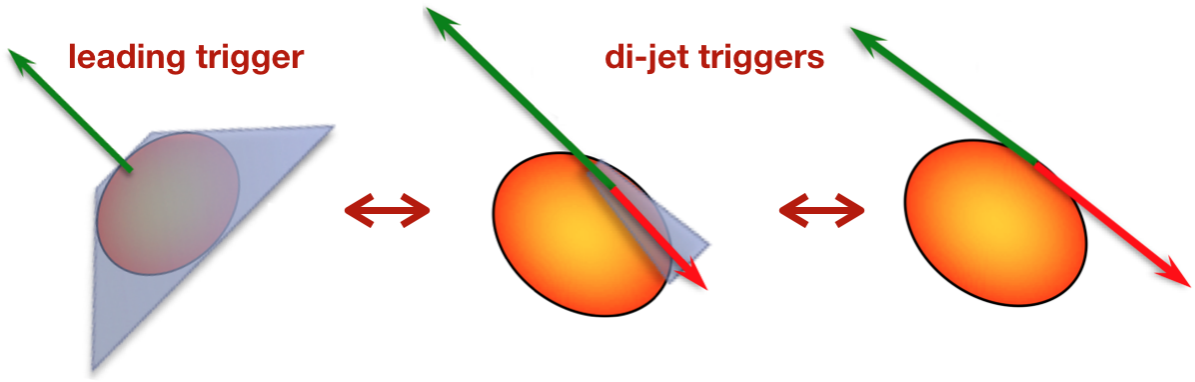

Figure 7.2: A schematic of jet-geometry engineering. Left: requiring a single jet-like object, like the jet-hadron correlations [58] or hadron-jet correlations [91] would bias the trigger jet to be produced close to the surface, but leave the recoil jet unconstrained. Middle: a hard-core di-jet selection like the STAR A_J measurement [61] would bias both the leading and subleading jets to be close to the surface, creating a tangential configuration with respect to the fireball. Right: A very strict di-jet selection could possibly select essentially unmodified jets that experience minimal modification. This is consistent with what is seen in the STAR 2+1 correlations [92, 93].

7.2 Data selection

Data selection is similar to the description in Chapter 5. The most central 0-20% Au+Au high-tower events from 2007 are compared to $p+p$ high-tower events from 2006 embedded in central Au+Au minimum bias. The minimum-bias data is also used for an analysis of the sensitivity of the measurement to correlated jet yield for balancing, described in Section 7.5. Each $p+p$ event is used multiple times, by embedding the same event into 10 different minimum-bias Au+Au events to reduce the statistical error on the $p+p$ reference.

Event, track, and tower selections follow the procedure outlined in Chapter 5. The $p+p$ tracking efficiency is made to match Au+Au by randomly discarding tracks as described in Section 5.4, to compare the $p+p$ to Au+Au at the Au+Au jet energy scale.

7.3 Jetfinding procedure

Jetfinding is done using TPC tracks and calorimeter towers for both Au+Au and embedded p+p data. All hard-core and matched jet-finding uses the anti-k_t algorithm. The analysis uses the general hard-core and matched jetfinding procedure defined in Section 3.3,

with some modifications.

Initial hard-core jet-finding is done using constituents above a certain $p_{\mathrm{T}}^{\mathrm{const}}$ that is systematically varied from 1.0 to 3.0 GeV/c in steps of 0.5 GeV/c. The jet resolution parameter is also varied from 0.2 to 0.4, producing 25 distinct hard-core di-jet definitions.

Hard-core jets are required to be in the pseudorapidity range $|\eta| < 1.0 - R$. The leading and subleading hard-core jets are required to have a p_{T} greater than 16.0 and 8.0 GeV/c, respectively. These thresholds were lowered from the original STAR di-jet imbalance measurement to increase statistics, in particular for di-jet definitions with $p_{\mathrm{T}}^{\mathrm{const}} > 2.0$ GeV/c. The hard-core di-jets are required to be back-to-back in ϕ, satisfying $|\Delta\phi| > 2.74$. Once a di-jet pair is found, then the full event is clustered with all constituents down to $p_{\mathrm{T}} > 0.2$ GeV/c. These jets are then matched to the hard-core di-jets via their radial distance, requiring $\Delta\mathcal{R} = \sqrt{(\Delta\phi)^2 + (\Delta\eta)^2}$, where $\Delta\phi = \phi^{\mathrm{jet}}_{\text{hard-core}} - \phi^{\mathrm{jet}}_{\text{matched}}$ and $\Delta\eta = \eta^{\mathrm{jet}}_{\text{hard-core}} - \eta^{\mathrm{jet}}_{\text{matched}}$ to be less than the jet-finder resolution parameter.

All jets (not just the matched jets) are background-subtracted. This is because the $p_{\mathrm{T}}^{\mathrm{const}}$ cut for the hard-core jets is varied from 1.0 to 3.0 GeV/c. When $p_{\mathrm{T}}^{\mathrm{const}}$ approaches 1.0 GeV/c, the background ρ is non-zero in central Au+Au events and must be corrected for. This can be seen in Figure 7.3, where ρ is shown on the left and σ is shown on the right. We see that the ρ distribution for the full event ($p_{\mathrm{T}}^{\mathrm{const}} > 0.2$ GeV/c) is very broad - this is due to the wide centrality definition we use: 0-20%. Large ρ is not a problem, as it is estimated and subtracted. Large intra-event σ, however, is a measure of significant uncertainty in the ρ estimation on an event-by-event basis. We see on the right side of Figure 7.3 that in the most central events, a matched jet can have a σ of over 15 GeV/A, leading to background fluctuations on the order of 8 GeV inside a jet cone of $R = 0.4$. Background estimation and subtraction is performed as described in Section 3.2. We only use the constituents that were used during jetfinding for background ρ estimation; for example, for a di-jet definition with a $p_{\mathrm{T}}^{\mathrm{const}} > 1.5$ GeV/c selection, ρ estimation is performed with constituents with $p_{\mathrm{T}}^{\mathrm{const}} > 1.5$ GeV/c as well.

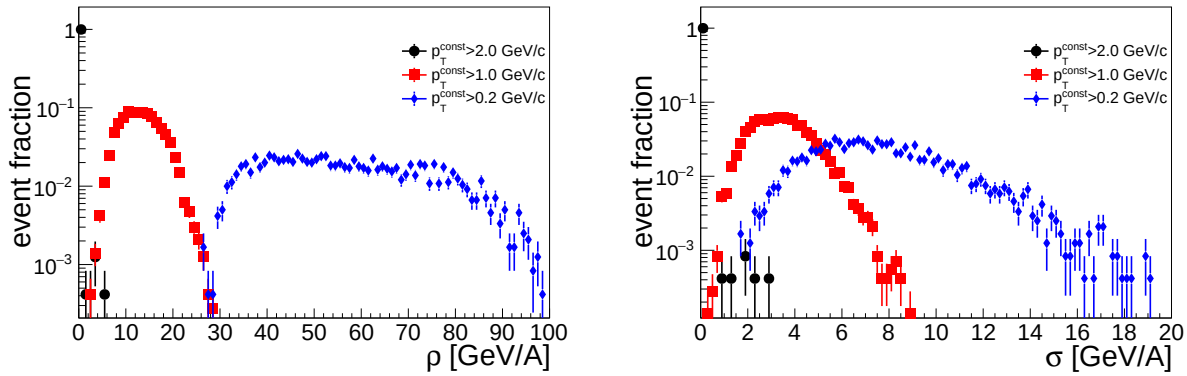

Figure 7.3: Left: ρ distribution measured at STAR in the 20% most central collisions for constituents with $p_{\mathrm{T}} > 2.0$, 1.0, and 0.2 GeV/c. Right: Intra-event σ for the same events.

7.4 Systematic uncertainties

Systematic uncertainties are assessed on both relative TPC efficiency and the BEMC energy scale, as was done for the jet energy scale uncertainty in the di-jet hadron correlations. The tracking efficiency uncertainty between Au+Au and $p+p$ is approximately $90 \pm 7\%$ [45]. The effect of this systematic is assessed by repeating the di-jet imbalance measurement with the relative efficiency set to $90-7 = 83\%$ and $90+7 = 97\%$. The relative tower efficiency between Au+Au and p+p is $98 \pm 2\%$ [45]. The effect of the tower efficiency on the measurement was found to be negligible. The tower energy scale uncertainty is 2% [45]. This is assessed similarly to the tracking efficiency, by performing the di-jet imbalance measurement again while varying the tower energy scale by $\pm 2\%$. The systematics are estimated by varying the embedded p+p only. The uncertainty on each bin in the $|A_J|$ due to either tracking or tower uncertainty is taken as the maximum absolute difference between the nominal value and the two variations. Because the systematics are independent of each other (modulo some small effect due to the hadronic correction of the tower energy), they are varied separately, and correlations are not considered. The systematics reported on the di-jet imbalance measurement are the quadrature sum of tower energy scale uncertainty and the relative tracking efficiency uncertainty, and is shown as shaded box on all $p+p$ measurements. Tracking efficiency was

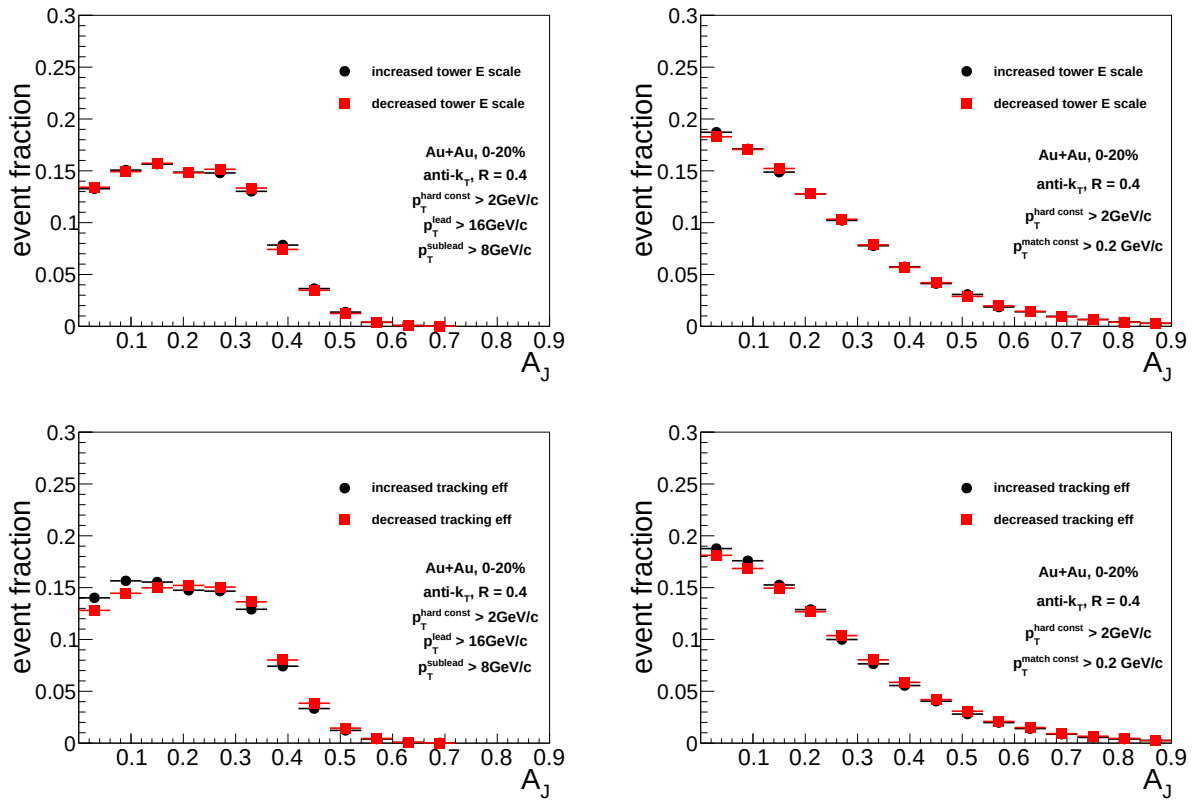

Figure 7.4: Examples of the change in the $|A_J|$ distribution due to the variation of the tower energy scale and the relative tracking efficiency on the embedded $p+p$ hard-core and matched di-jets. Top left: varying the tower E scale by $\pm 2\%$ on the hard-core di-jets. Top right: varying the tower E scale by $\pm 2\%$ on the matched di-jets. Bottom left: varying the relative tracking efficiency by $\pm 7\%$ on the hard-core di-jets. Bottom right: varying the relative tracking efficiency by $\pm 7\%$ on the matched di-jets.

found to be the dominant systematic for both hard-core and matched di-jets. An example of the effect the systematics have on the A_J measurement can be seen in Figure 7.4 for a single di-jet definition, and the full set of systematics can be found in Appendix F.

7.5 Quantifying sensitivity to jet modification

The large increase in background energy density when reducing $p_{\mathrm{T}}^{\mathrm{const}}$ cut from the hard-core parameter value to 0.2 GeV/c for the matched jets leads to a significant increase in the region-to-region fluctuations of the background density ($\sigma_{\rho,p_{\mathrm{T}}^{\mathrm{const}}}$). When the quantity $\sigma_{\rho,p_{\mathrm{T}}^{\mathrm{const}}} A$ – a measure of the magnitude of fluctuations that can be expected in a jet of area A – becomes much larger than $p_{\mathrm{T}}^{\mathrm{jet}}$, the A_J distribution could become insensitive to the physical balancing from the correlated jet yield due to fluctuations. To quantify the sensitivity to the physics of interest, we test a null hypothesis that any balancing that is measured is completely due to uncorrelated background fluctuations.

To perform this test, Au+Au hard-core di-jet axes are embedded into 0-20% central Au+Au minimum-bias events as 4-vectors, and perform the matched clustering. We can embed the jets as 4-vectors instead of imbedding the individual constituents because of the anti-k_t algorithm's IRC safety. We then perform the radial matching of the hybrid event jets to the embedded hard-core jet axes. This explicitly disallows any physical balancing from correlated soft jet yield, and thus any balancing that is measured comes purely from the background fluctuations present in the embedding event. This test is called the random cone (RC) method. The results of the RC method are shown in Figure 7.5. This method is identical to the random-cone method used in the original STAR A_J paper [61]. The STAR A_J also performed a second test called the eta-cone (EC), which was not performed in this analysis because the EC and RC methods showed similar behavior.

The KS test results for the RC test are shown in Table 7.1. Any test value less than 10^{-5} is approximated as zero. In this table and all following tables, the color is chosen as a visual aid to represent the magnitude of the test value. Green is for test values greater than 0.05, yellow for values between 10^{-4} and 0.05, and red for all values less than 10^{-4}.

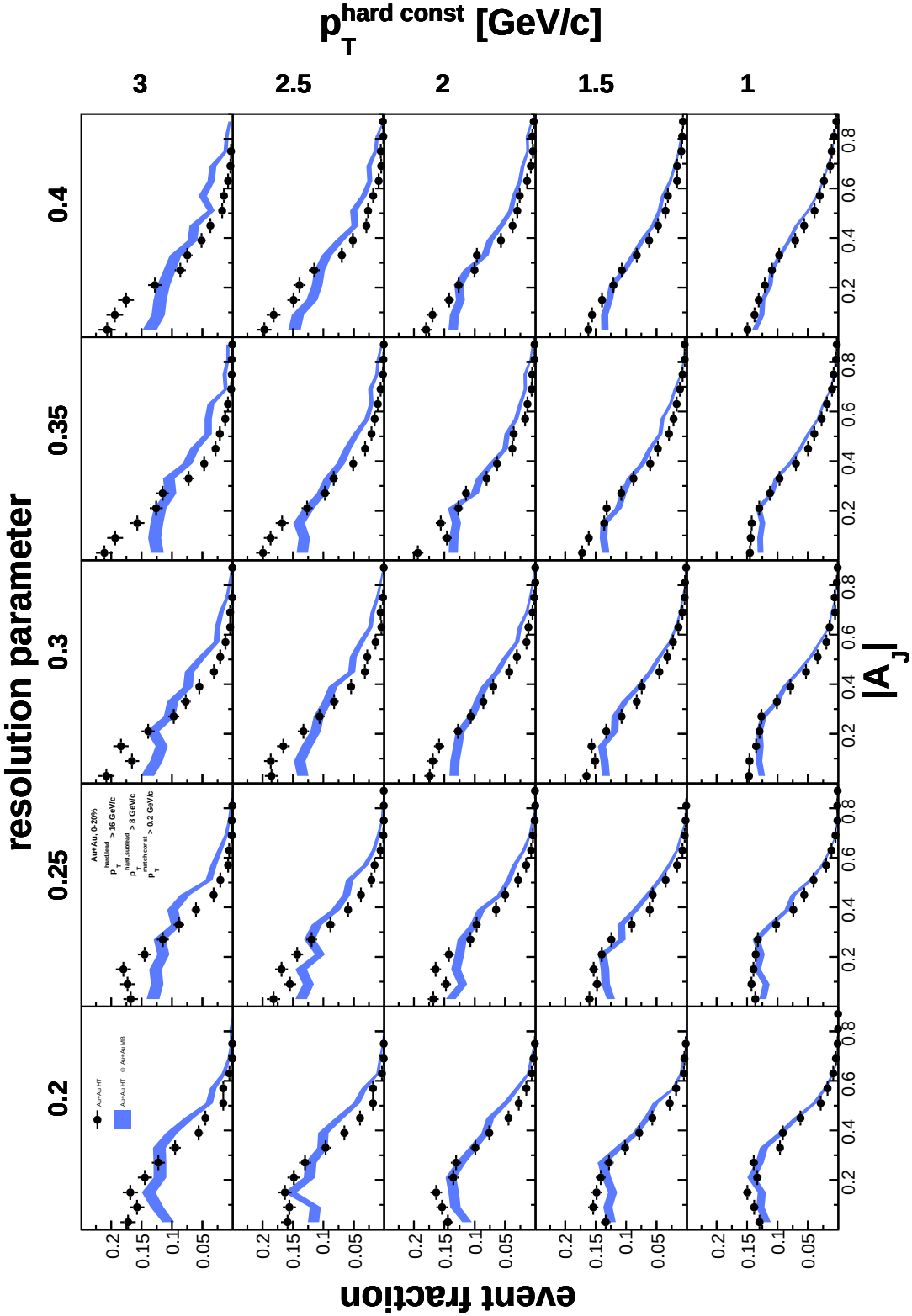

Figure 7.5: $|A_J|$ distributions for all di-jet definitions varying $p_{\mathrm{T}}^{\mathrm{const}}$ and R for Au+Au matched di-jets (black) and the RC null hypothesis (blue band).

p_T^{const} [GeV/c] \ jet-finder R	0.2	0.25	0.3	0.35	0.4
3.0	0	0	0	0	0
2.5	0	0	0	0	0
2.0	0	0	0	0	0
1.5	0	0	0	0	10^{-4}
1.0	10^{-5}	10^{-5}	0	0	0

Table 7.1: Kolmogorov-Smirnov test for matched Au+Au and RC di-jets. Test result $\ll 1.0$ for all di-jet definitions.

From the distributions in Figure 7.5 it can be seen that the background fluctuations introduce significant broadening of the $|A_J|$ distribution, but that the RC test is less balanced than the matched $|A_J|$, with a significant shape difference. This is consistent with the test results in Table 7.1 that show the distributions are statistically dissimilar. From this we conclude that for all di-jet definitions considered in this work, there is sensitivity to the physical balancing of the di-jets by the correlated jet yield inside the jet cone down to low p_{T}.

7.6 Differential di-jet imbalance of hard-core jets

The di-jet imbalance is calculated for all hard-core di-jet definitions. The resulting distributions are shown in Figure 7.6. By eye, all distributions differ significantly when compared to the $p+p$ reference.

The results from the KS test are shown in Table 7.2. The test result is significantly less than one for all di-jet definitions, from which we conclude that Au+Au is not balanced to the level of the $p+p$ and significant modification is present for all di-jet definitions. This shows that we have identified a selection of hard-core di-jets. Therefore we can use these di-jets to study the hard-core di-jet definition's effect on jet modification via the matched di-jets. We also consider a radial scan of a select set of hard-core di-jets, which is introduced in the next section.

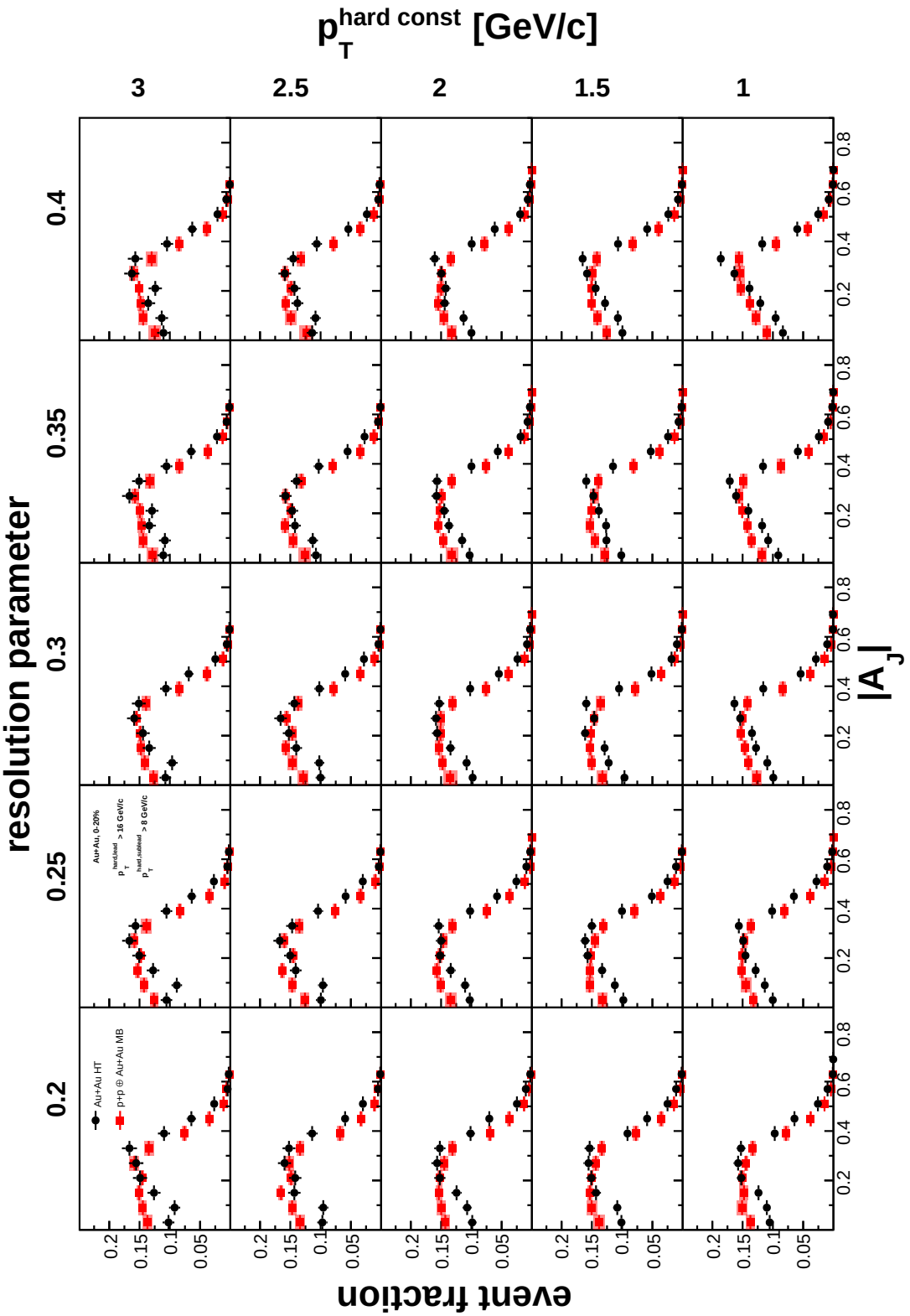

Figure 7.6: $|A_J|$ distributions for all di-jet definitions for Au+Au (black) and p+p $\oplus$ Au+Au (red) hard-core jets.

p_T^{const} [GeV/c] \ jet-finder R	0.2	0.25	0.3	0.35	0.4
3.0	0	0	0	0	0
2.5	0	0	0	0	0
2.0	0	0	0	0	0
1.5	0	0	0	0	0
1.0	0	0	0	0	0

Table 7.2: Kolmogorov-Smirnov test for hard-core Au+Au and p+p $\oplus$ Au+Au di-jets. Test result $\ll 1.0$ for all di-jet definitions.

7.7 Radial scan of hard-core di-jets

We would like to estimate the radial distribution of the radiated energy loss for a given set of modified hard-core jets and determine at what, if any radius that balance is recovered to the level of the $p+p$ reference. To accomplish this, we fix the jet radius to a specific value ($R = 0.2$). We then match these narrow hard-core jets to matched jets with varying radii from $R = 0.2$ to 0.4. A visual representation of this procedure is shown in Figure 7.7. The result is shown in Figure 7.8. Each row has the same population of hard-core jets, and the variation from column to column is only in the radius of the matched jet - thus, we call this a radial scan of the hard-core jets. A summary of the results of the KS test is shown in Table 7.3. We see that balance is generally restored to the level of the $p+p$ reference around $R = 0.3 - 0.35$, relatively independently of the $p_{\mathrm{T}}^{\mathrm{const}}$ cut. This suggests that for a fixed, narrow hard-core radius of $R = 0.2$, there is minimal change in the radiated energy. It is possible that this is because such a narrow initial radius is necessarily selecting jets that are fragmenting similarly regardless of the $p_{\mathrm{T}}^{\mathrm{const}}$ cut; this is consistent with the normal angular ordering of jet fragmentation in vacuum, where constituents carrying a significant fraction of the jet's energy are found more closely to the jet axis.

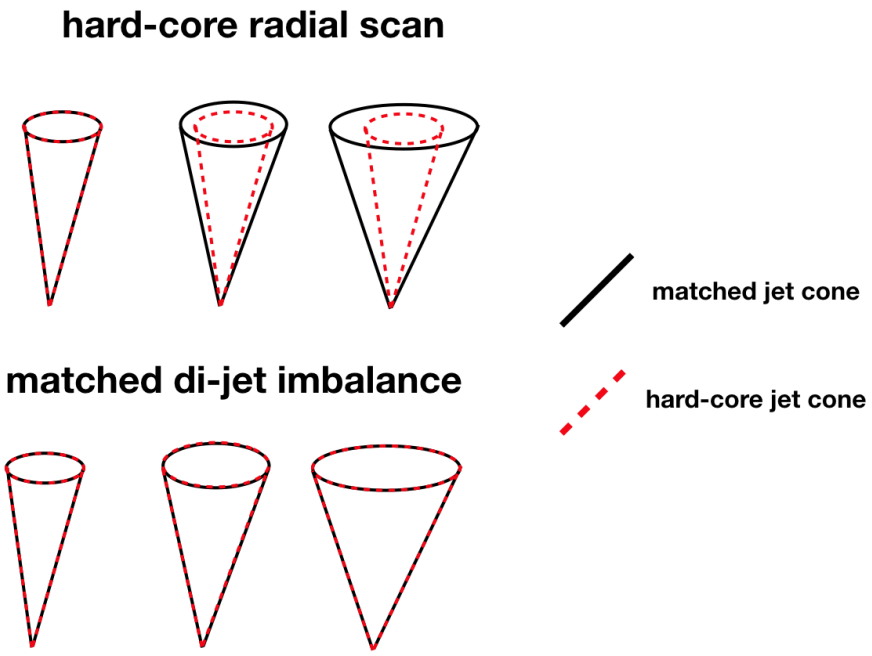

Figure 7.7: Visual representation of the radial scan procedure. A hard-core di-jet is found with a fixed R=0.2, and a variable $p_{\mathrm{T}}^{\mathrm{const}}$. Each hard-core di-jet is then matched to matched di-jets with $p_{\mathrm{T}}^{\mathrm{const}} > 2.0$ GeV/c with radii varying from 0.2 to 0.4. Thus, every hard-core di-jet is matched to five matched di-jets. For the traditional matched di-jet imbalance however, each hard-core and matched di-jet have the same radius.

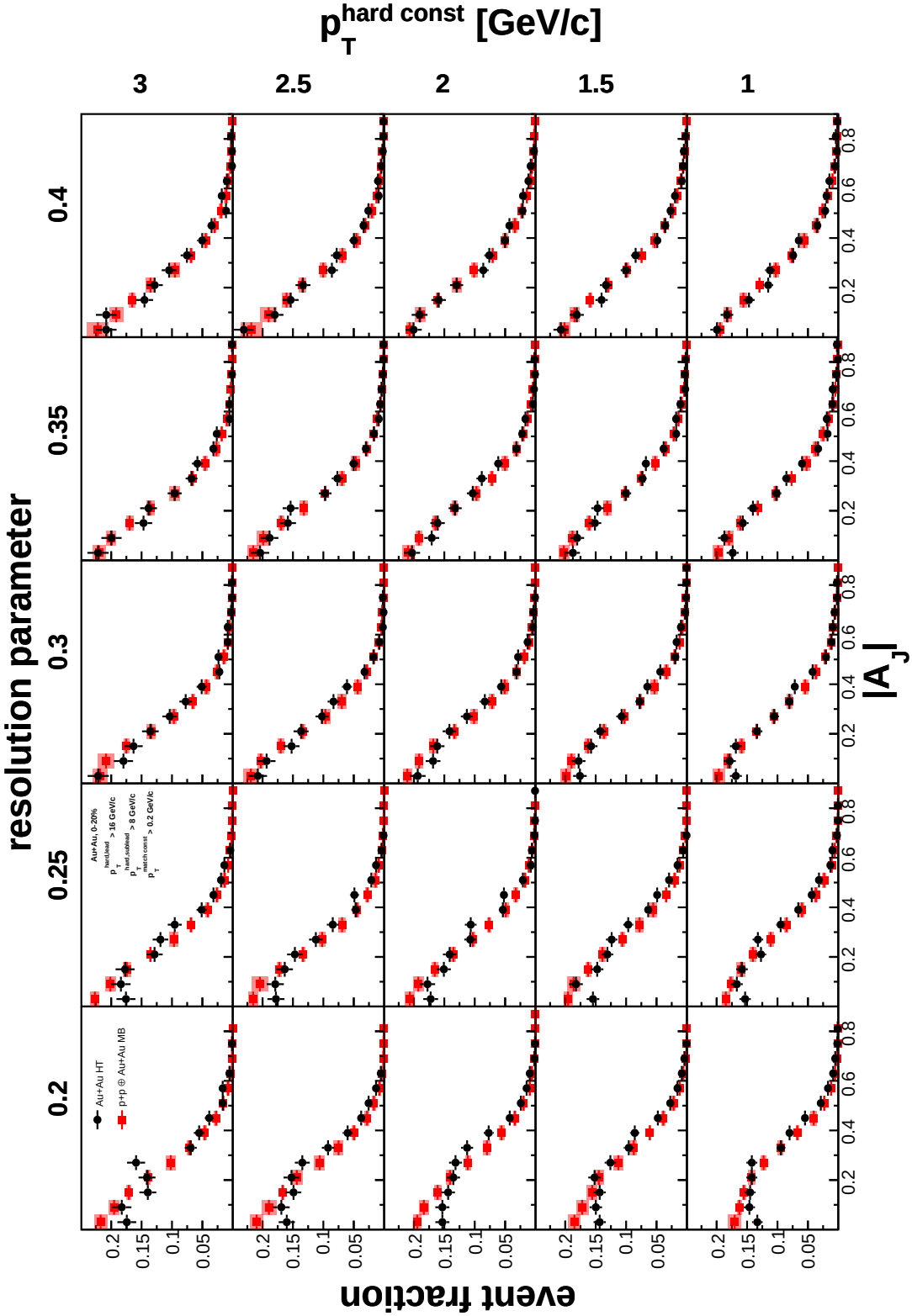

Figure 7.8: $|A_J|$ distributions for all di-jet definitions for Au+Au (black) and p+p $\oplus$ Au+Au (red) matched di-jets with a fixed hard-core radius (R=0.2).

p_T^{const} [GeV/c] \ jet-finder R	0.2	0.25	0.3	0.35	0.4
3.0	10^{-5}	10^{-4}	0.15	0.77	0.55
2.5	0	10^{-4}	0.079	0.12	0.69
2.0	0	0	0.0060	0.077	0.59
1.5	0	0	0.0084	0.034	0.58
1.0	0	10^{-5}	0.0019	0.13	0.48

Table 7.3: Kolmogorov-Smirnov test for matched Au+Au and p+p $\oplus$ Au+Au di-jets for a fixed hard-core radius (R=0.2). Test result $\ll 1.0$ for di-jet definitions with R$<$ 0.3 . Test result generally ~ 1 for R $\geq$ 0.35.

7.8 Differential di-jet imbalance of matched jets

In the original STAR A_J results it was found that while balance was restored for matched di-jets with a radius of 0.4, when the radius was reduced to 0.2 balance was no longer restored [61]. We have shown that even when increasing the $p_{\mathrm{T}}^{\mathrm{const}}$ cut for the hard-core di-jet selection, all di-jets are modified with respect to the $p+p$ reference in our kinematic selection. We show the corresponding matched di-jets, where the radius is equal between the hard-core and matched jets in Figure 7.9, with the results of the KS test shown in Table 7.4. We see a different trend than in the radial scan, where we now see a relatively smooth transition from very modified di-jets at smaller R and smaller $p_{\mathrm{T}}^{\mathrm{const}}$ to balanced jets at larger R and larger $p_{\mathrm{T}}^{\mathrm{const}}$. In the region defined by $R \geq 0.35$ and $p_{\mathrm{T}}^{\mathrm{const}} \geq 2.0$ GeV/c the Au+Au is found to be balanced to the level of the $p+p$ reference which implies that the soft radiation is recovered within the cone of the jet-finder, and tightly correlated with the original jet axis, whereas for smaller R and $p_{\mathrm{T}}^{\mathrm{const}}$ the balance is not recovered, suggesting significant broadening of the radiated energy outside the jet cone. This shows that the radial distribution of the radiated energy is sensitive to the initial hard-core di-jet definition. The di-jet definition dependence of the energy loss suggests an experimentally robust method of jet geometry engineering at RHIC energies.

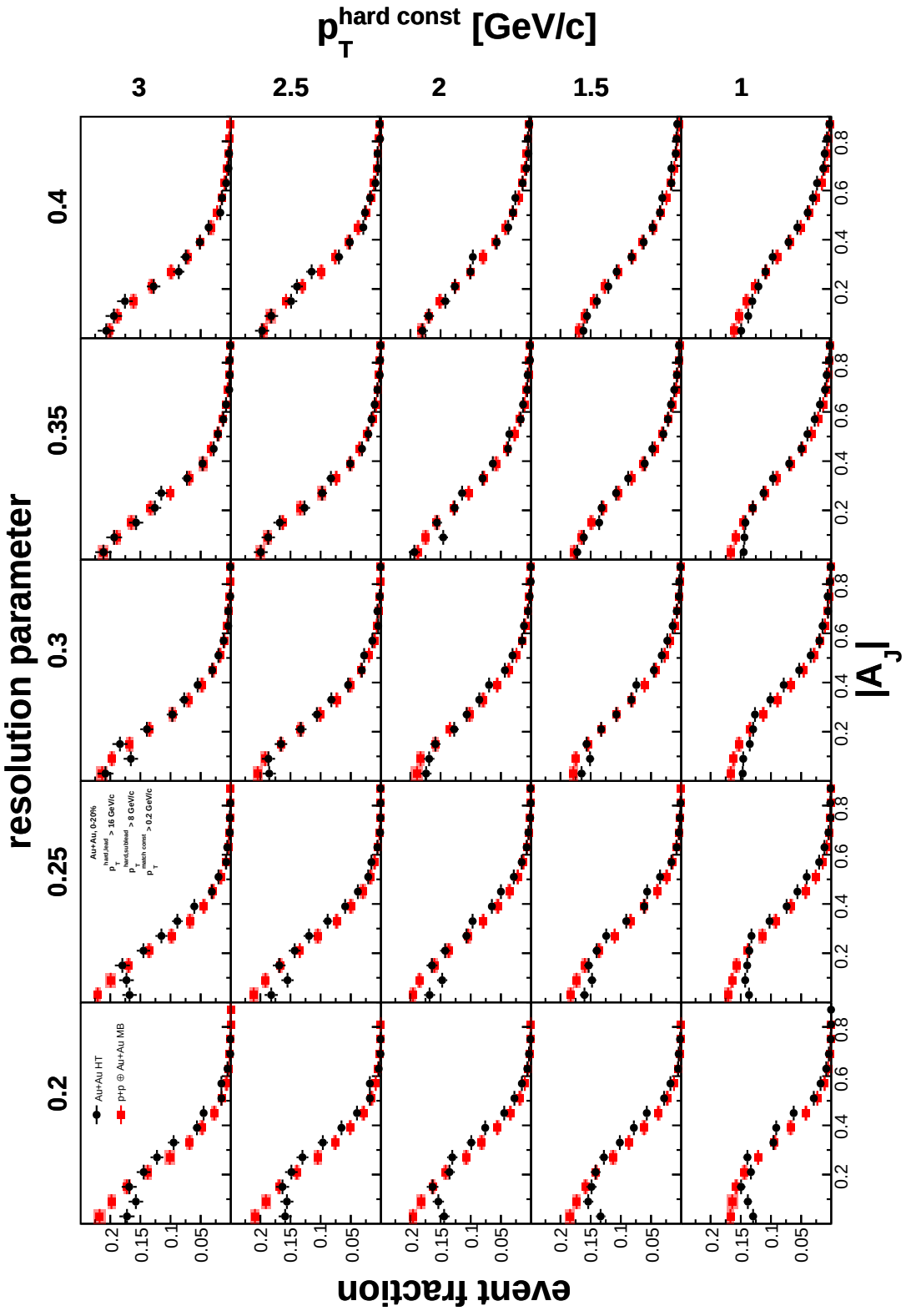

Figure 7.9: $|A_J|$ distributions for all di-jet definitions for Au+Au (black) and p+p $\oplus$ Au+Au (red) matched di-jets.

p_T^{const} [GeV/c] \ jet-finder R	0.2	0.25	0.3	0.35	0.4
3.0	0	0	0.0012	0.60	0.29
2.5	0	0	0.0029	0.99	0.54
2.0	0	0	0.0051	0.026	0.78
1.5	0	0	10^{-4}	0.018	0.020
1.0	0	0	0	0	0

Table 7.4: Kolmogorov-Smirnov test for Au+Au and p+p $\oplus$ Au+Au matched di-jets. Test result $\ll 1.0$ for di-jet definitions with small R, p_T^{const}. Test result ~ 1 for large R, p_T^{const}.

7.9 Conclusions

We have shown differential measurements of $|A_J|$ for central Au+Au and embedded $p+p$ at RHIC energies as a function of the hard-core $p_{\mathrm{T}}^{\text{const}}$ and jet radius. We see a significant imbalance of all hard-core di-jets, showing that in the kinematic regions explored in this analysis no unmodified samples of di-jets were found. However, the balance is recovered to the level of the $p+p$ reference for a subset of di-jet definitions with larger radii and higher p_T^{const} when soft constituents are included in the matched di-jet definitions, suggesting the energy is recovered within the jet cone.

This is consistent with the results of the previous STAR A_J result, and shows that the amount of softening and broadening of the jet can be controlled by tuning of the jet resolution parameter and the $p_{\mathrm{T}}^{\text{const}}$ of the di-jet definition. This suggests there is a possibility of controlling the jet in-medium path length via proper selection of di-jets (jet geometry engineering). The measurement may also provide novel methods to validate and tune jet energy loss models at RHIC energies; compared to traditional jet measurements that may vary a single parameter, such as the radius or the jet p_{T}, a systematic variation of the jet/di-jet definition in multiple parameters should provide stronger constraints.

To further study jet geometry engineering, comparison to jet energy loss models is necessary. Because the path length is not an observable quantity, it must be inferred from theoretical calculations or phenomenological models. Two Monte Carlo generators are being considered: JEWEL and JETSCAPE. The next steps will be to attempt to reproduce the

results seen in the differential di-jet imbalance, measure if the di-jet definitions lead to any significant path length dependence, and see if the path length dependence varies significantly between definitions.

8 SUMMARY

"Don't adventures ever have an end? I suppose not. Someone else always has to carry on the story."

– J.R.R. Tolkien, *The Lord of the Rings*

In this dissertation, two analyses related to partonic energy loss and properties of the QGP were shown. To understand the structure of the hard-core di-jets being used at STAR, the di-jet hadron correlations measured the charged hadron correlations with respect to the trigger and recoil jet axes in the event, as a function of hadron p_{T}. In the analysis it is found that both the trigger jet and recoil jet show similar yields and widths in the $p_{\mathrm{T}}^{\mathrm{assoc}} > 2.0$ GeV/c region compared to a $p+p$ reference, showing that the hard-core di-jets in general have a relatively vacuum-like fragmentation pattern. However, while the trigger jet appears vacuum-like in the yields, a modest enhancement of the yield in constituents in the range of $1.0 < p_{\mathrm{T}}^{\mathrm{assoc}} < 2.0$ GeV/c in the recoil jet compared to the $p+p$ shows that some modification of the jets is occurring, and that the radiated energy is recovered within a relatively narrow cone in this $p_{\mathrm{T}}^{\mathrm{assoc}}$ range. These results are consistent with and enhance the understanding of the previous STAR jet-hadron correlations and A_J results, which show hard-core jets significantly bias the selected jet population towards relatively unmodified jets, and that any energy loss in this population is found within a relatively narrow jet cone. This bias in the jet fragmentation suggests the possibility of a surface bias of the jet production with respect to the medium, due to the predicted path length dependence of partonic energy loss, previous theoretical calculations (see Sections 2.2.1 and 7.1), as well as the predicted behavior of gluon radiation in the medium; larger path lengths (increased time in the medium) would correspond to being transported further from the jet axis, increasing the effect of broadening of the jet.

To explore the possibility of varying the amount of modification in the selected di-jet sample, the differential di-jet imbalance measurement studied the evolution of the imbalance as a function of the jet radius and hard-core constituent p_{T} cut. Using the A_J observable, the

analysis showed that for all hard-core di-jets with a constituent p_{T} cut between 1.0 and 3.0 GeV/c and with radii between 0.2 and 0.4, the di-jet population was significantly modified with respect to the $p+p$ reference. However, in the matched A_J it is seen that there is a significant dependence of the balancing on both the jet radius and the hard core constituent p_{T} cut. This result shows that it is possible to select jets that are more or less modified with respect to vacuum fragmenting jets by controlling the parameters of the hard-core di-jet selection, and suggests that it may be possible to systematically control the path length of selected di-jets via the parameters of the di-jet definition as illustrated in Figure 8.1. This would allow for jet geometry engineering to be used to more differentially study partonic energy loss at RHIC energies.

8.1 Extensions and improvements to current analyses

Both the di-jet hadron correlations and the differential di-jet imbalance have interesting opportunities for continuing study and refinement, especially with the use of the new STAR Run 14 Au+Au dataset that is now available.

The di-jet hadron correlations have a few areas that could be explored with a larger dataset. First, the widths of the higher $p_{\mathrm{T}}^{\mathrm{assoc}}$ bins are not well defined, because the $\Delta\eta$ and $\Delta\phi$ bin widths were made relatively large to increase the individual bin statistics. With the expected increase in statistics of Run 14, this would allow a reduction in the 2D bin size, and allow a more robust comparison of the shape of the correlations in the high-p_{T} ranges. The increase in statistics should also allow at least one more $p_{\mathrm{T}}^{\mathrm{assoc}}$ bin to be analyzed down to 0.5 GeV/c (by reducing the relative error on the background), which would give a more comparable range to the jet-hadron correlations and allow for a more complete statement about the radius of the quenched energy. Another possibility for an extension is to measure the centrality dependence. To further understand the interplay between the STAR A_J result and the di-jet hadron yields, the increased statistics would allow the correlations to be performed in bins of A_J or $\Delta A_J = A_J^{\mathrm{hard-core}} - A_J^{\mathrm{matched}}$. This could help understand exactly what mechanism contributes most to the significant deviation in the hard-core A_J, while the

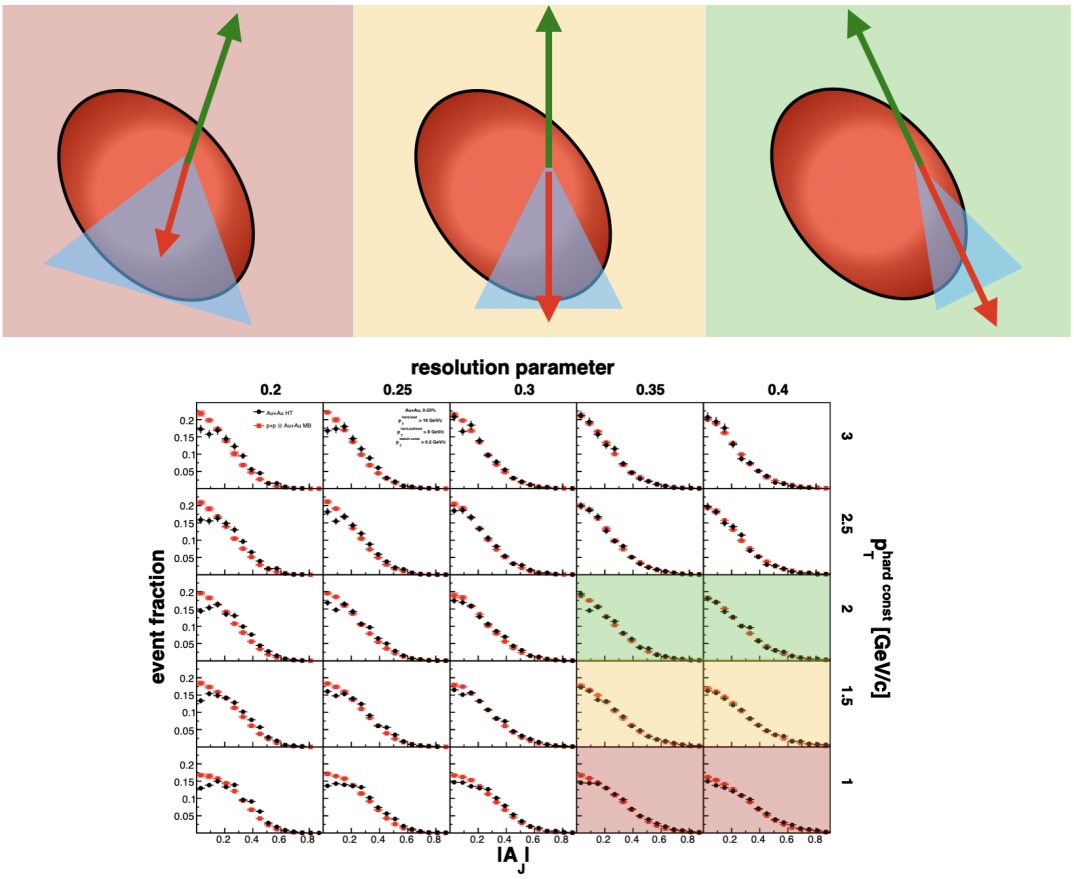

Figure 8.1: Illustration of the predicted change in jet geometry with respect to the QGP due to variations of the jet definition based on the results of the differential di-jet imbalance. The neutral online trigger that is used for event selection is predicted to significantly bias the trigger jet (green arrow) towards surface production. By variation in the di-jet definition, however, the path length bias of the recoil jet could be varied from less biased and more strongly quenched (left image) to a strong bias towards more tangential production and minimal quenching (right image). In this picture, the left image would correspond to di-jet definitions that show significant imbalance, while the right image corresponds to balanced definitions.

di-jet hadron yields show minimal modification in the relevant $p_{\mathrm{T}}^{\mathrm{assoc}}$ range.

The differential di-jet imbalance measurement would also benefit significantly from increased statistics. It would allow the $p_{\mathrm{T}}^{\mathrm{lead}}$ and $p_{\mathrm{T}}^{\mathrm{sublead}}$ to be increased, and thus allow for a more complete scan of the di-jet definition parameters. Measuring the centrality dependence of the differential di-jet imbalance would also be possible, which would allow for a measurement of evolution of the modification for each di-jet definition as a function of the system size.

Since the jet path length is not a directly observable quantity, it can only be inferred via comparison to theory. To make a direct connection between the amount of modification of a set of di-jets and an actual path-length bias will require a comparison to energy loss models. A few Monte Carlo models are available and are being considered, primarily JEWEL [94] and JETSCAPE [95]. If a model can both predict the differential results measured by STAR and predict a path length dependence, it would strengthen the picture of the path-length bias in the jet-hadron correlations and A_J and give a quantitative description of jet geometry engineering.

The ability to systematically control the path length would provide a new tool to study the path length dependence of partonic energy loss, and would allow for a robust tomographic scan of the medium, increasing the ability of experimentalists to study the details of jet-medium interaction at RHIC energies. Irrespective of the path length dependence, the differential di-jet definition provides a multi-dimensional data-driven approach that will both allow for greater constraints on partonic energy loss models and introduce the idea of more fully differential measurements in the jet definition for future analyses.

8.2 Outlook

The potential of jet geometry engineering to augment current and future jet studies of the quark gluon plasma could be profound. The trend in experimental heavy-ion jet physics is moving towards more differential measurements, including tools and observables beyond the single inclusive spectra and R_{AA}-style ratios. It has become clear that single inclusive

measurements are not sufficient to fully utilize jets as a probe of the QGP, as significant information is encoded in the structure of the jet.

For instance, if the initiating parton radiates a high p_{T} gluon carrying a significant fraction of the jet's total energy either before or during transport through the medium, the energy loss of the jet can be modified, depending on how the medium resolves the jet. If the radiation occurred at a sufficiently narrow angle, then the medium would not resolve the jet as two separate color charges, but as a single color charge. However, if the angle is wide enough, then the medium would resolve two color charges, and the average medium modification would be expected to be increased [96]. This coherence/decoherence effect can be used to estimate the transport coefficient and would allow for further understanding of the details of jet-medium interaction.

However, this relies on the ability to tag populations of jets which have a high probability of having split inside or outside the medium. The formation time of the first hard split in vacuum should be proportional to $1/z\theta^2$, where θ is the angle of emission and z is the fraction of the initiating parton's energy that is radiated. Of course, one does not have access to the parton shower history, and thus we use the Soft Drop algorithm, which "grooms" away wide angle, soft radiation, and the z_g and R_g observables, which may be correlated with the first hard split's z and θ, respectively [97]. Jet geometry engineering would allow jets to not only be selected based on their formation times, but also by their in-medium path length, possibly allowing selection of otherwise similar jet populations, but which differ in the in medium path length, and thus the fraction of jets which had a hard split before exiting the medium. This would allow for direct testing of the coherent/incoherent radiation picture described above, with the first attempts at this measurement showing no significant difference in the amount of quenching due to the opening angle of the first hard split at RHIC energies, suggesting the hard-core recoil jets at STAR in our current kinematic selections are in fact probing the medium as a single color charge [98]. These formation times are also significantly different at RHIC and LHC kinematics, suggesting complimentary measurements at the two facilities

will prove useful [99].

Appendix A TERMINOLOGY AND KINEMATIC VARIABLES FOR COLLIDER PHYSICS

The lab frame for high energy physics collider experiments tend to be defined with the $\hat{z}$ along the beam line (by convention), with $\hat{x}$ and $\hat{y}$ set arbitrarily in the plane defined by $\hat{z}$ as the normal vector. The major experiments at both RHIC and the LHC are generally cylindrical in design to allow a full 2π coverage in azimuth, and the symmetry of both the detector geometry and the physics of interest naturally lends itself to a cylindrical coordinate system. When cylindrical coordinates are used, they follow the traditional definitions, with $r = \sqrt{x^2 + y^2}$, $\phi = \tan^{-1}\left(\frac{y}{x}\right)$ and z equivalent to the cartesian direction.

The observables of interest in a high energy physics collider experiment are the collision or decay vertices and particle momenta and energy. The *primary* vertex of a collision is the position of the collision inside the detector body along the beam line. it is generally described in cartesian coordinates (v_x, v_y, v_z). Secondary vertices due to particle decays are described with respect to the primary vertex.

Particle tracks, calorimeter hits, or other methods of particle identification are generally described by their 4-momenta, (p_x, p_y, p_z, E). However, p_z (and the polar angle with respect to the beam axis, $\theta = \tan^{-1}\left(\sqrt{x^2 + y^2}/z\right)$) are not boost-invariant, and thus physics relevant effects are conflated with background effects like the energy spread in the colliding beams ($\mathrm{RMS}(\delta E_{\mathrm{beam}}/E_{\mathrm{beam}}) \approx 0.6 \times 10^{-3}$) at $\sqrt{s_{NN}} = 200$ GeV at RHIC [63], whereas in boost-invariant kinematics these effects would average out. Due to this effect we introduce a polar coordinate, the *rapidity*, y,

$$y = \frac{1}{2} \ln \frac{E + p_z c}{E - p_z c}. \tag{A.1}$$

Rapidity is additive under z boosts, so the effects mentioned above average out. We can then define the 4-momenta by $(p_{\mathrm{T}}, \phi, y, E)$, where ϕ is the traditional azimuthal angle, and p_{T} is the transverse momentum: the momentum transverse to the beam line, $p_{\mathrm{T}} = \sqrt{p_x^2 + p_y^2}$.

Sometimes the energy E of a particle is not known - for instance, in STAR, the TPC

reconstructs a track's momenta, not its energy. In these cases, we substitute the rapidity for the *pseudorapidity*, defined as

$$\eta = \frac{1}{2} \ln \frac{|\vec{p}| + p_z c}{|\vec{p}| - p_z c}. \tag{A.2}$$

Because $E^2 = |\vec{p}|^2 + m^2$, η and y converge in the high-momentum limit, and are exactly equal in the case of massless particles.

Appendix B RUN 11 QUALITY ANALYSIS

In an effort to increase the useable di-jet statistics for both the original A_J measurement and the analyses discussed in this dissertation, a quality analysis (QA) was done for Au+Au data recorded in 2011. The high tower dataset from Run 11 contains approximately seven times more events than Run 7. The primary focus of the QA was the TPC and BEMC performance, and if the data could be used as a replacement for Run 7 in the analyses that were active at that time. However, due to problems in the TPC that are enumerated below, Run 11 was ultimately rejected as the next primary Au+Au dataset in favor of Run 14, which is discussed in Appendix C.

B.1 Time projection chamber

The TPC had two major issues during Run 11. First, two sectors were damaged. This resulted in a significant decrease in the tracking efficiency for charged tracks that were located in the range of about $-1.0 < \phi < 0.0$. Figure B.1 shows that these two sectors had an average efficiency of about 70% compared to the rest of the detector.

To use this data in the same way we have done previous analyses (compare Au+Au to a p+p reference that is made to match the efficiency of the Au+Au), this would have required a ϕ dependent efficiency, which is generally not done to reduce the amount of statistics needed in the embedding data used to estimate the effciency. The other option is to not accept jets that are found within the damaged sectors, so that a 2D (p_{T},η) dependent efficiency definition would be useable. However, because jets are extended objects, and because we look at di-jet events, requiring back-to-back jets, this reduces our useable ϕ range to less than 1/2 of the full 2π azimuth, significantly reducing available statistics.

The TPC was also was found to have significant differences in tracking efficiency during a run period of about 300 runs, corresponding to about 1/4 of the total data recorded in 2011. During this time period, there is a significant time dependence of the tracking efficiency, shown in Figure B.2, where the average number of tracks dips for a period of about 150 runs, before increasing again. The effect of the damaged sectors on the mean refmult was

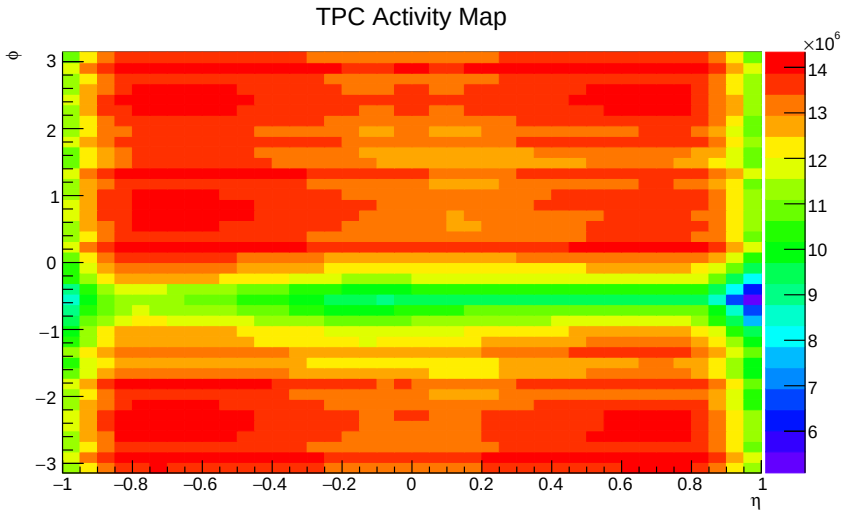

Figure B.1: Total number of tracks recorded by the TPC for the entire Run 11 high-tower dataset. It is found that for the average track, the sectors in the region $-1.0 < \phi < 0.0$ operated at about 70% of the rest of the TPC when compared with tracks that passed some minimal quality cuts including DCA and number of fit points. The reduced efficiency was more pronounced in high-p_{T} tracks, due to their straighter path through the magnetic field.

checked, and was found not to be the cause. Ultimately, no obvious cause was found. Because the cause was unknown, these runs would not have been able to be used in analysis without a time-dependent efficiency correction.

Due to these two problems, the effective useable statistics with a nominal (p_{T},η) dependent efficiency correction was found to be only equal to the statistics in Run 7. Because Run 14 was being produced at the time, the effort required to recover more statistics from Run 11 was deemed unneccessary, and the focus shifted to Run 14.

B.2 Barrel electromagnetic calorimeter

The barrel calorimeter was deemed to be relatively healthy in Run 11. A map counting the number of times a tower fired in η, ϕ coordinates is shown in Figure B.3. A relatively small group of dead towers (towers that were not active during the run) was seen, and a handful of "hot" towers (towers that fired too frequently, or recorded energies that were unphysical, due to a stuck bit in the readout, other hardware error, or poor calibration). The accepted procedure to deal with hot towers is to mask them out. To do this, an iterative

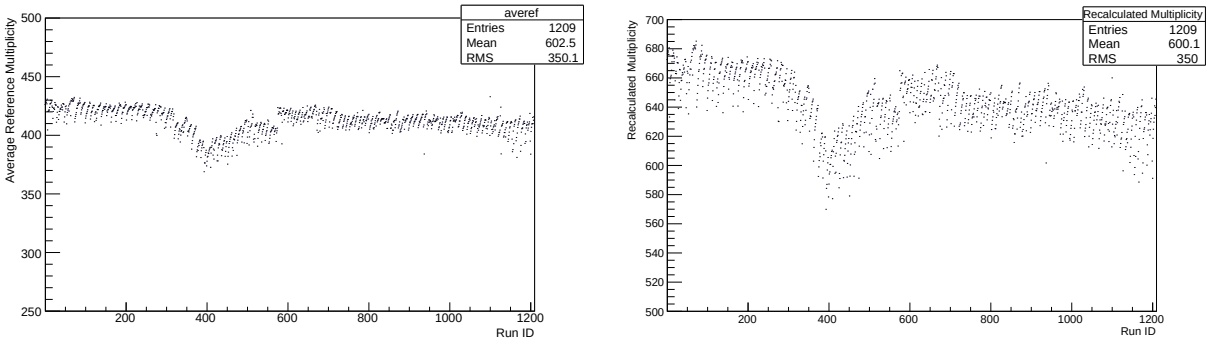

Figure B.2: Left: Mean refmult as a function fo run number for central events - a stand in for time. A significant dip in the tracking efficiency was seen in the range of the 300th run to the 600th run. This effect was not explained by the damaged sectors, and the cause was not identified. Right: Same events but counting the number of primary tracks outside of the damaged sectors. This shows that the damaged sectors were not responsible for the reduction in mean refmult.

removal procedure was used. First, towers that fired too frequently compared to the average were removed (too frequently was defined as any tower that fired more than four standard deviations higher than the mean). Next, towers that had an average recorded energy four standard deviations higher than the mean were removed. Finally, to help remove towers that fired the online trigger too frequently, any tower that fired with $E > 2.0$ GeV four standard deviations higher than the mean was also removed. The effect of this bad tower removal can be seen in Figure B.3. In the pre-hot tower removal E_T spectrum, there are multiple jumps in the distribution. These jumps (except for the jump at 4 GeV) are unphysical, and caused by hot towers. In the E_T spectrum after hot tower removal, these jumps are no longer present. The peak at 4 GeV is from the presence of the online high tower trigger, and is expected.

The complete list of all the hot and dead towers are critical for our embedding procedure. To make the BEMC equivalent in the triggered Au+Au and the embedded $p + p$ reference, the hot and dead tower lists are combined from both datasets, so that the active towers are identical between the two. This allows for a consistent geometry, and reduces any systematic bias that may be present in the calorimeter between runs.

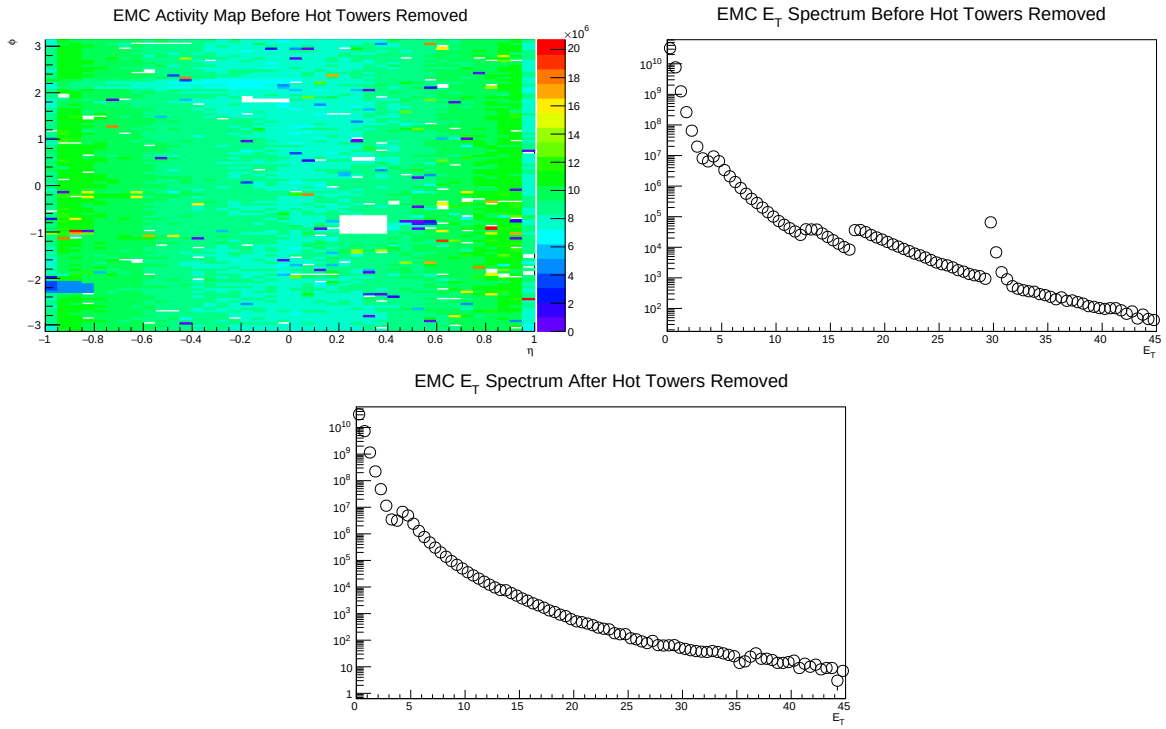

Figure B.3: Top left: tower activity map. White spots are dead towers, red spots are hot towers. Top right: Tower E_T spectrum before hot towers are removed. Jumps in the distribution are from hot towers. Bottom: E_T spectrum after hot tower removal. The distribution is approximately smooth out to 30 GeV, except for the online trigger threshold at 4 GeV.

Appendix C RUN 14 QUALITY ANALYSIS

Because of the issues found in the TPC in Run 11 data, it was decided to move to Run 14, skipping Run 11. Run 14 is a high luminosity dataset with a large increase in statistics compared to Run 7 or Run 11. Run 7 had a maximum zero degree calorimeter (ZDC) coincidence rate (measure of the number of interactions per second) of around 20 to 25 kHz, whereas Run 14 has a maximum ZDC coincidence rate of over 100 kHz. For an estimate of the increase in statistics, Run 14 has approximately 10 times more hard-core jets with $p_{\mathrm{T}}^{\mathrm{jet}} > 20.0$ GeV/c and $p_{\mathrm{T}}^{\mathrm{const}} > 2.0$ GeV/c compared to Run 7 (before event quality cuts and application of a hot tower list).

Because of issues with the heavy flavor tracker (HFT) and reconstruction code, there have been multiple productions of the high tower and minimum bias data that we are interested in for jet physics. Because of this, this appendix will discuss the productions in chronological order and explain the decisions that led to new productions being requested.

C.1 Production P16id/P15ic

The original production of the Run 14 data was split into two sets: the high luminosity data (zdc coincidence rates (zdcX) ¿ 60 kHz) and the low and mid luminosity data. The high luminosity data was recorded without the HFT to protect the detector from damage. This high luminosity data was produced in the production series P15ic, and for some reason a $p+p$ vertex finder was used. We believe this was a mistake on the part of the software and computing team. This change in the vertex finder does not affect the most central events, but can have significant effects in the most peripheral collisions, where the track multiplicity is low.

The low and mid luminosity data (zdcX ¡ 60 kHz) was originally produced in the P16id production series and included the HFT as a required component for all primary tracks that were found within the acceptance of the HFT structure (approximately when an event was within $|v_z| < 6$ cm, with a v_z dependent track η window). This requirement for HFT hits massively increases the resolution of the DCA for those tracks, but significantly reduces the

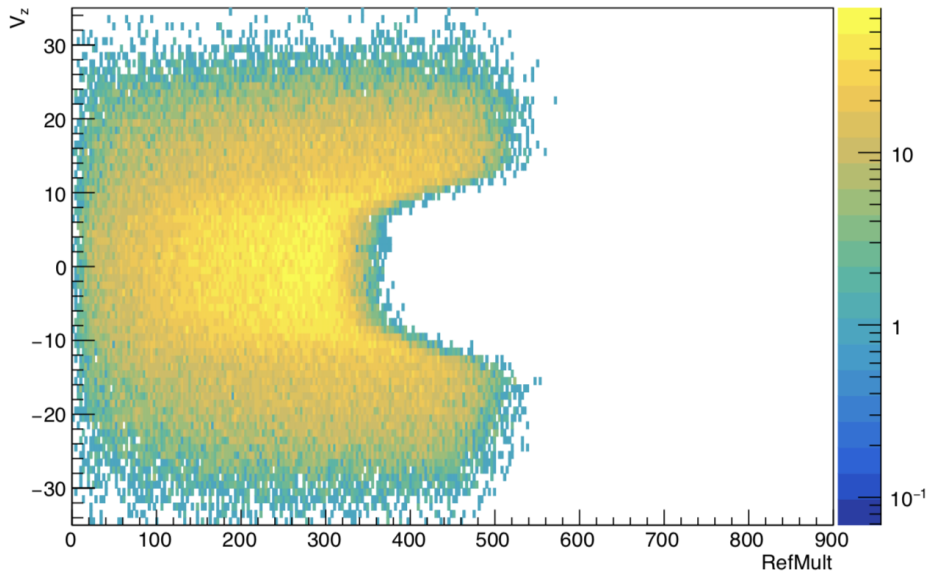

Figure C.1: Significant reduction of tracking efficiency when the primary vertex is located inside the HFT ($|v_z| \leq\sim 6$ cm)

overall tracking efficiency, as any tracks that do not have matched hits in the HFT are not primaries. The effect on the tracking efficiency as a function of v_z can be seen in Figure C.1.

For jet physics, the DCA of the tracks is of less importance than having a good tracking efficiency. Because of this, we evaluated two options: either using global tracks (which did not require the HFT in the tracking) or ask for a reproduction of the dataset without including the HFT. To test the usability of the global tracks, a small test data set without any HFT was requested, such that we had the same physical events produced with and without the HFT included in the tracking, so that we could compare on a track-by-track basis the degradation of the tracking resolution when global tracks are used instead of primary tracks. The comparison is shown in Figure C.2. The result showed that the majority of global tracks, which do not include HFT hits, had significantly worse transverse momentum resolution than the corresponding primary track, and further, that this resolution is not the same for global tracks with an HFT hit. Because of this, we decided it would be more efficient to ask for full reproduction of the data without the HFT included in tracking.

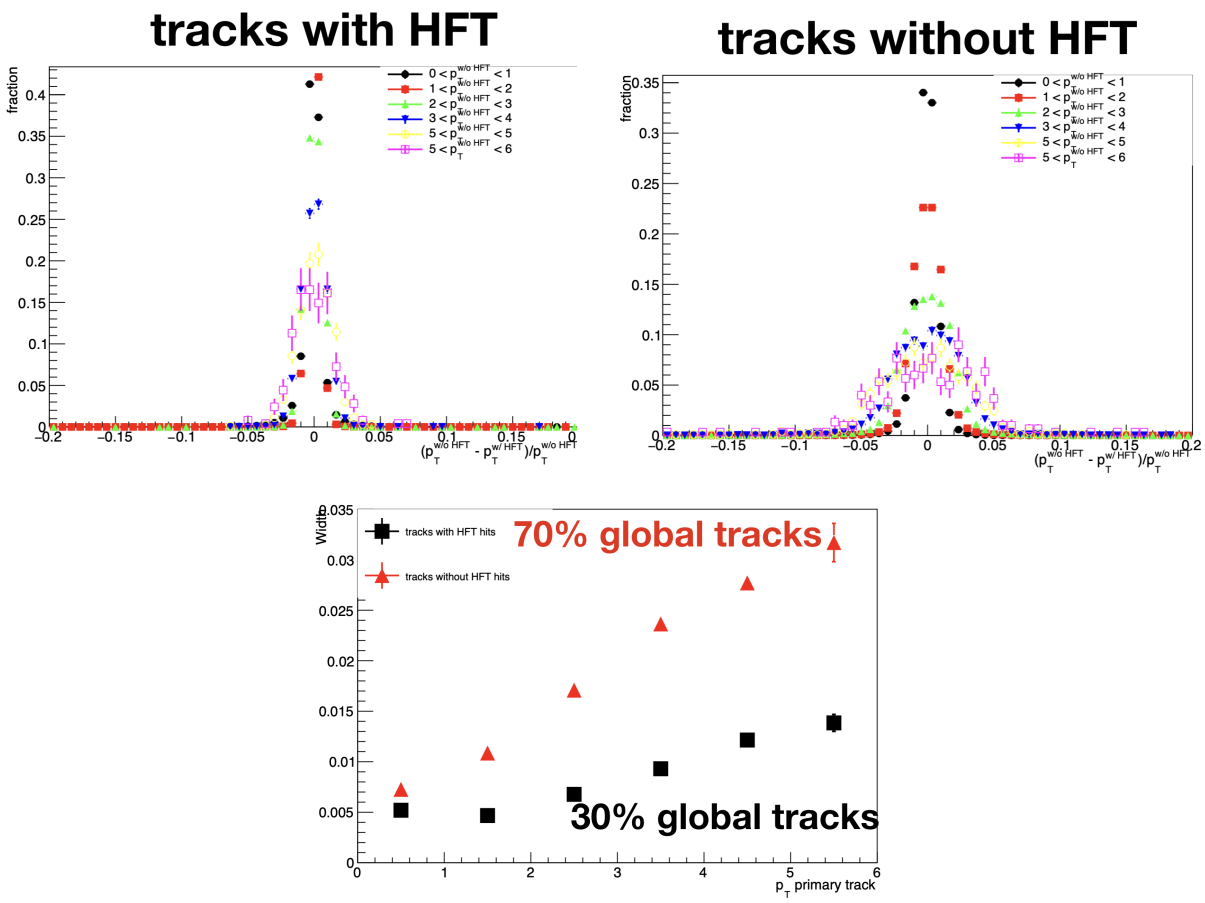

Figure C.2: Comparison of global tracks with and without HFT to estimate the relative effect on tracking efficiency. Top left: the relative difference between the no-HFT production primary track (assumed "true" p_{T}) and its corresponding matched global track that includes an HFT hit. Top right: the relative difference between the no-HFT production primary track (assumed "true" p_{T}) and its corresponding matched global track with no HFT hit. Bottom: a comparison of the widths of the above distributions. A narrower width implies better p_{T} resolution. It is found that global tracks with no HFT hits have significantly worse transverse momentum resolution than those with at least one HFT hit.

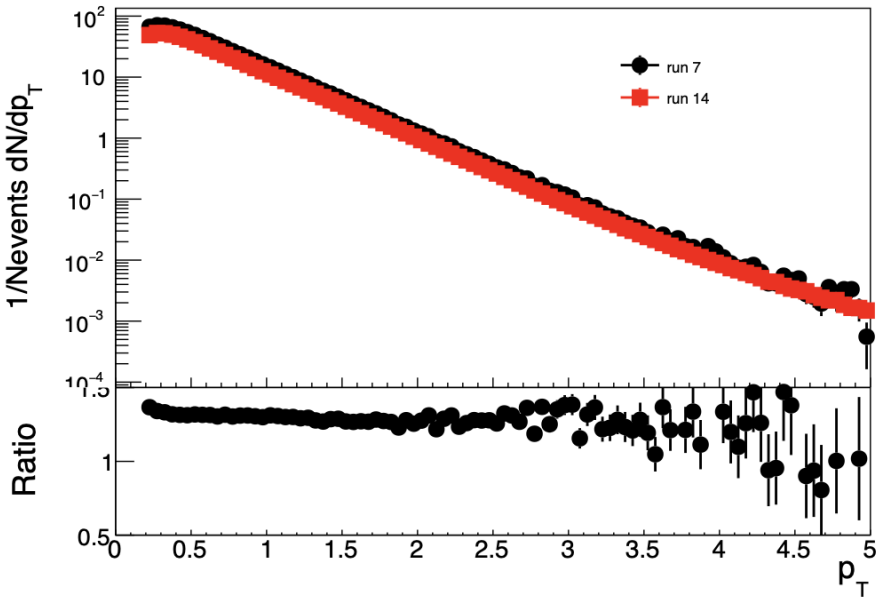

Figure C.3: Efficiency corrected p_{T} spectra comparison between Run 14 and Run 7 for the 5% most central events. Systematic deviation is well beyond what can be explained by the uncertainty on the embedding.

C.2 Production P17id

The Run 14 was reproduced in the P17id production series. However, when doing cross-checks for consistency with older datasets (using Run 4, Run 7, and Run 11), some inconsistencies were found. Original QA, including creation of a hot tower list (as described in Appendix B) and general tracking QA for the TPC appeared good. However, after I created a centrality definition (following the procedure defined in Appendix D) and tracking efficiencies (shown in Appendix E) for the P17id production, comparison of Run 14 and Run 7 efficiency corrected p_{T} spectra for the most central collisions (0-5%), deviated significantly as shown in Figure C.3. Because these are efficiency corrected spectra for the same collision energy, $\sqrt{s_{NN}} = 200$ GeV, comparing similar centralities should give consistent results within the error on the estimation of the efficiency from embedding (quoted as 5% for STAR). It was also found that the number of candidate primary vertices per event was very large (as shown in Figure 5.3).

These issues were brought to the attention of the STAR software and computing group. The issue with the number of candidate primary vertices per event was found to be caused by the use of a $p+p$ optimized vertex finder, and was corrected in the next production. The tracking, however, took longer to find. Eventually, two bugs were tracked down, relating to track reconstruction and embedding. The technical details of the bugs are beyond the scope of this dissertation, but it was found that one bug caused a measurable decrease in the number of reconstructed good tracks in an event; the other bug changed the behavior of the embedding library used to generate the embedding events, causing Monte Carlo tracks to behave differently during reconstruction compared to the data tracks from the event that it is embedded into. An overview of the changes in tracking and embedding as a function of time can be seen in Figure C.4. Because there was a difference in tracking efficiency between embedded Monte Carlo tracks and recorded data, the efficiencies were necessarily not correct, which can explain the incorrect p_{T} spectra showed in Figure C.3. All three of these bugs were fixed, and the data was reproduced again.

C.3 Production P18ih

The P18ih production fixes the major bugs that were introduced in P17id. The QA described above for P16id and P17id productions was performed by myself, but validation and tooling P18ih has become a wider group effort in the heavy-ion jet group in STAR. I am currently working on generating the centrality definition for the new dataset, which can be seen in Appendix D.

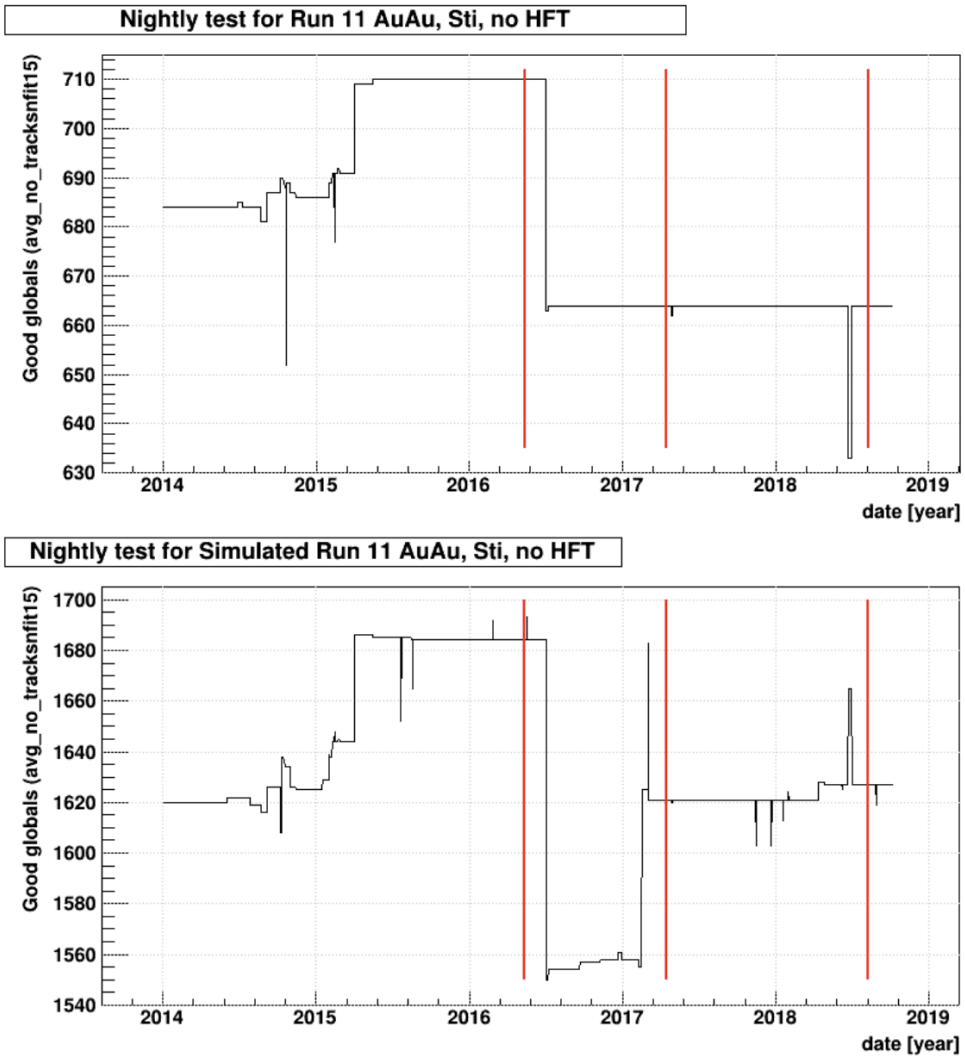

Figure C.4: Nightly test results run by STAR to test reconstruction and embedding. Showing Run 11 instead of Run 14 because Run 14 tests included HFT, and we want to see only changes in TPC efficiency. Red lines show when new STAR library versions are released. First red line is the library used for P16id production, second red line is the library used for P17id production. Top: the number of good global tracks reconstructed nightly for a set of test events recorded during Run 11. Bottom: Number of reconstructed good tracks for a test set of Monte Carlo events. The tracking bug can be seen as the large drop in reconstructed tracks around June 2016. The embedding bug is the large increase in reconstructed Monte Carlo tracks in the bottom panel that is not reproduced in the top panel. Plots taken from Gene Van Buren's STAR internal QA [86].

Appendix D RUN 14 CENTRALITY ESTIMATION

In this appendix we describe the details of the centrality definition for the Run 14 Au+Au P18ih production at STAR. The centrality is estimated using a tool called a Glauber Model. An introduction to Glauber Models is given in Section D.1.

STAR uses reference multiplicity as an estimate of centrality. Reference multiplicity (refmult) is defined as the number of primary tracks within one unit of pseudorapidity ($|\eta| < 0.5$) with some minimal track quality cuts. The reference multiplicity scales monotonically with the centrality of the collision,allowing a one-to-one mapping between refmult and centrality, with the highest refmult events corresponding, on average, to the most central (smallest impact parameter) collisions.

Because the performance of tracking in the TPC depends significantly on the TPC occupancy and primary vertex location, corrections to account for these effects must be applied before final estimation of the centrality definitions. These corrections will be discussed in Section D.2, the fit to the Glauber model will be discussed in Section D.3, and consistency checks for the results are discussed in D.4.

D.1 Glauber Models

As described in Chapter 2, the properties of a collision depend on the physical overlap of the two nuclei, which is quantified by observables such as the impact parameter, b, the number of participating nucleons, N_{part}, or the number of binary nucleon-nucleon collisions N_{binary}. Because the time and length scales involved are too small to probe these quantities directly, theoretical techniques to estimate these quantities from experimental data have been devised, generally referred to as "Glauber Models", named after Roy Glauber. Glauber formalized the use of quantum mechanical scattering theory in complex collision systems in done throughout the 1950s [100]. These early analytical calculations gave good agreement to collisions of small systems [22, 101, 102]. It wasn't until the 1970s, however, when the more recognizably modern versions and definitions of these tools were introduced, such as the use of the "optical limit" to simplify calculations [103]. It was also in the 70s when calculations

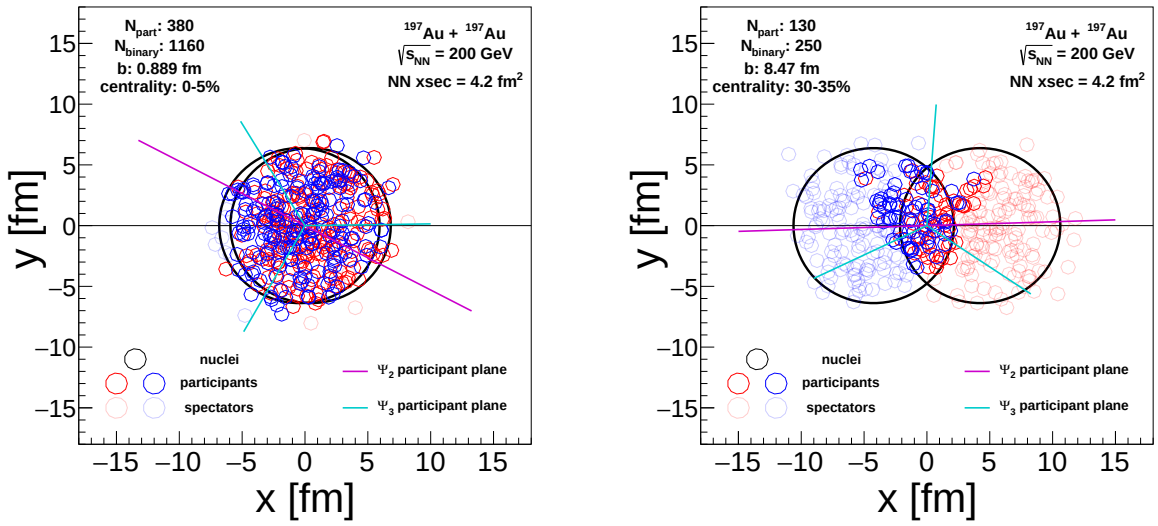

Figure D.1: Individual Glauber events with different impact parameters. Nuclei are shown as the large black circles, participants are shown in the bold colored circles and spectators are shown as translucent circles.

for inelastic nucleus-nucleus collisions were first presented.

In current day calculations for use in experiments, analytical calculations are generally not used, however. Instead, Monte Carlo Glauber Models simulate collisions by generating random distributions of nucleons inside nuclei randomly on an event-by-event basis, overlaying the two nuclei with a randomly sampled impact parameter, and counting the number of nucleon-nucleon collisions given some nucleon interaction cross section. A more in-depth discussion of the history of both analytical and Monte Carlo Glauber models is presented in the references [24].

Because of concerns with the validity and performance of prior Monte Carlo Glauber generators used in STAR, I developed a new library consisting of a Monte Carlo nucleus generator, collision analysis tools and the statistical methods used to fit data refmult distributions to Glauber multiplicity distributions. This library also includes tools for STAR specific corrections that are used to correct refmult distributions for pileup, luminosity dependent efficiency and other TPC inefficiencies. Examples of events generated using this

code can be seen in Figure D.1. Originally, the code was made to accurately recreate the interfaces of the STAR FastGlauberMCMaker utilities. However, the current goal is to break away from the old interface, separate the generator from the analysis tools, and create a more modular system that allows for fast addition of new nuclear PDFs, nucleon-nucleon cross sections and event analysis routines. The code can be found on Github at https://github.com/nickelsey/sct.

D.2 Pre-Glauber refmult corrections

Two corrections for variations in TPC efficiency are applied before the refmult distribution is fit to the Glauber. These are a correction for the degradation in the tracking efficiency due to increased occupancy as a function of luminosity (as estimated by ZDC coincidence rate), and a correction for the variation in tracking efficiency as a function of the primary vertex v_z position due to differences in the east and west portions in the TPC.

D.2.1 Luminosity correction

The effect of increasing luminosity on the tracking efficiency can be seen on the left side of Figure D.2. This slope is approximately linear and is corrected on an event-by-event level by scaling the refmult of the event by the ratio of the linear fit at some fixed normalization point (chosen to be 50 kHz, so that the range of the refmult distribution is approximately unaffected) and the coincidence rate of that collision. The corrected mean refmult is shown on the right side of Figure D.2. We check to see if the correction is consistent across different primary vertex v_z ranges in the bottom plot of Figure D.2.

D.2.2 Primary vertex position correction

Due to differences in tracking efficiency between the east and west side of the TPC, the reference multiplicity can change as a function of the primary vertex position along the beam line. To estimate the effect, the refmult distribution is divided into 3 cm bins in the nominal v_z range ($|v_z| < 30.0$ cm) for a total of 20 bins. In each bin, the high multiplicity tail is fit with an error function, and the midpoint of the error function (parameter labeled h in STAR) is estimated. This h parameter as a function of v_z is fit with a sixth degree polynomial. Like

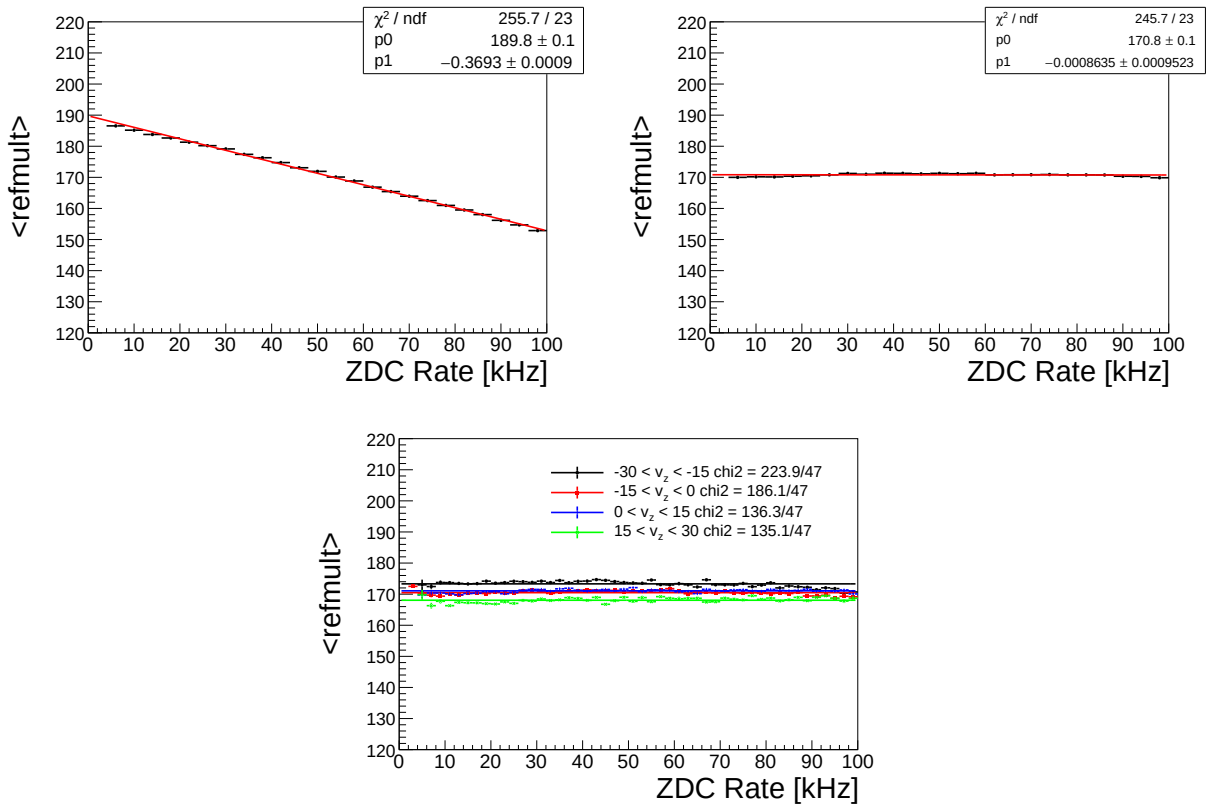

Figure D.2: Left: mean refmult as a function of luminosity (ZDC coincidence rate) shows a significant negative slope. Right: Corrected mean refmult distribution. Corrected distribution is approximately flat, as expected. Bottom: Correction is consistent in different v_z ranges.

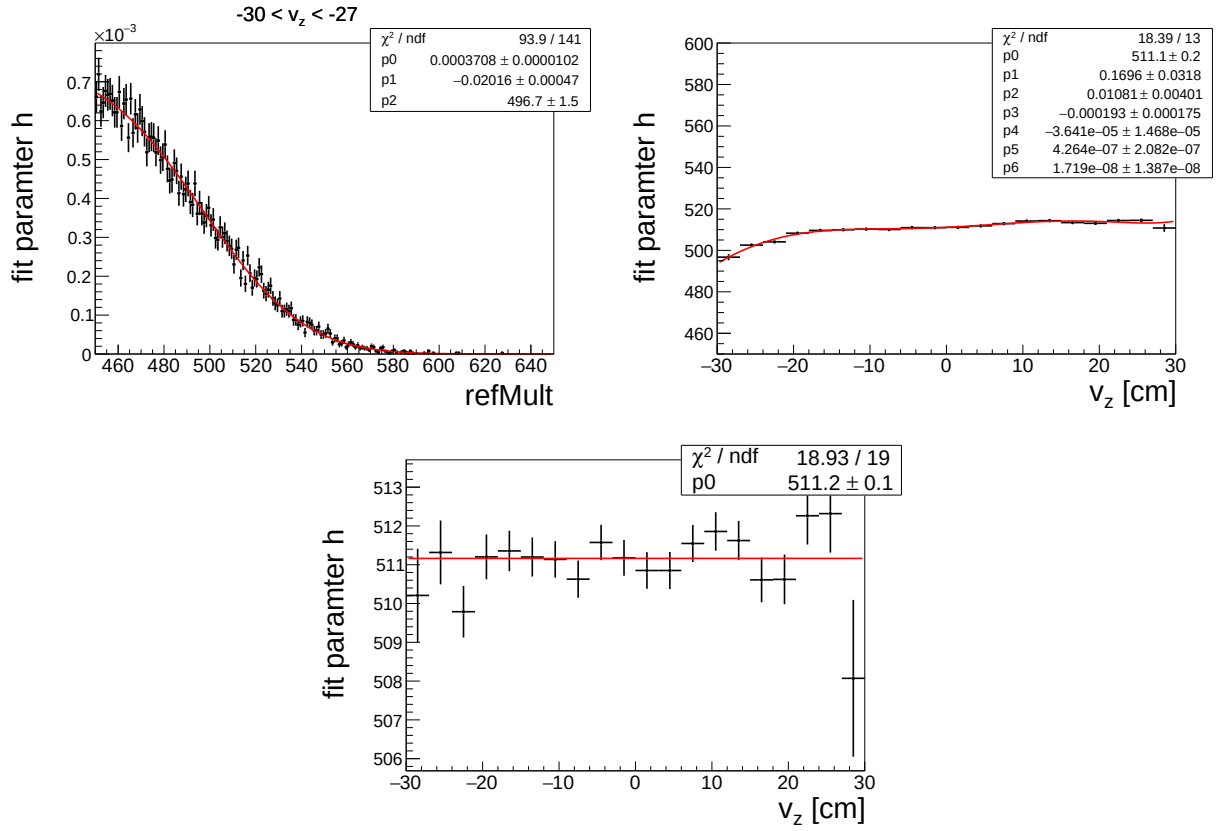

Figure D.3: Left: The error function fit to the refmult distribution in a small v_z range. Right: The fit parameter h as a function of v_z. Bottom: The corrected h parameter distribution. Flat as expected.

the luminosity correction, each event's refmult is corrected by a ratio of some normalization point (in this case, $v_z = 0.0$ cm) to the value of the fit function evaluated at the event's v_z. An example of the h parameter fit is shown in the top left plot of Figure D.3, h as a function of v_z is in the top right plot, and the corrected h distribution is shown in the bottom plot.

D.2.3 Corrected refmult

The final refmult distribution that is fit to the Glauber distribution is corrected event-by-event for both the luminosity and v_z effects discussed above. This event-by-event corrected refmult value is called the corrected reference multiplicity, or refmultcorr. The normalization points for the two corrections are chosen so that there is not a significant difference between the range of the refmult and refmultcorr distributions. A comparison of the uncorrected

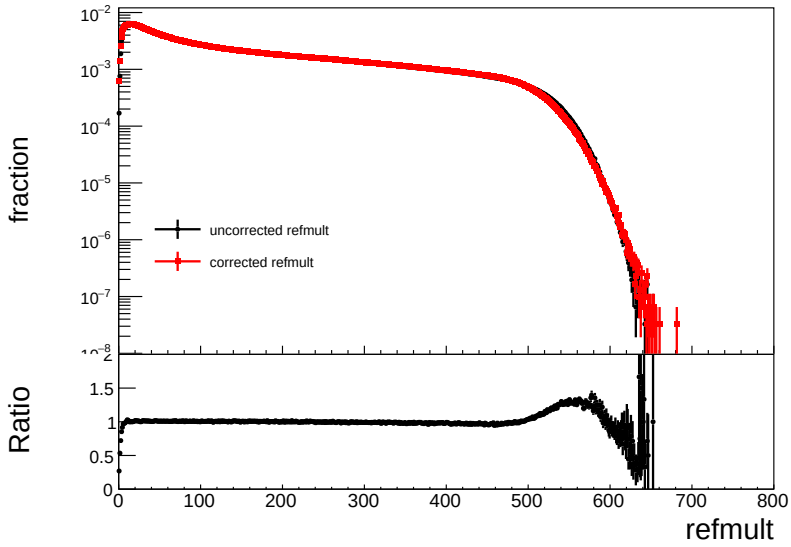

Figure D.4: Comparison of refmult and refmultcorr. Shape is generally similar, except for slight changes in the very high and low refmult ranges.

refmult and refmultcorr distributions are shown in Figure D.4

D.3 Glauber model fit

Because the VPD, our primary minimum-bias trigger, has low efficiency for low multiplicity events, the centrality can not be directly estimated from the reference multiplicity. Instead, the centrality is estimated from a Glauber distribution that is fit to the high multiplicity part of the refmultcorr distribution where the VPD is approximately 100% efficient.

A refmult distribution is simulated from the Glauber Monte Carlo by sampling the ($N_{\rm part}$, $N_{\rm coll}$) distribution of the simulated events. A two-part multiplicity model that depends on $N_{\rm part}$ and $N_{\rm coll}$, with a parameter x, which controls the relative contribution due to binary collisions ($N_{\rm coll}$) and the contribution due to the number of participants, or "wounded nucleons" ($N_{\rm part}$) is used to define an "ancestor multiplicity". This ancestor multiplicity is defined as m $= xN_{\rm coll} + (1-x)N_{\rm part}/2.0$. From experiments, this fraction x is measured to be around 0.14 in heavy-ion collisions at $\sqrt{s_{NN}} = 200$ GeV [104]. A negative binomial is then sampled N times (where N is the ancestor multiplicity) to simulate fluctuations in the multiplicity model. This negative binomial has two parameters. N_{pp}, the mean of the

binomial, can be roughly interpreted as the average refmult from a single $p + p$ collision. The second parameter, defined as k, controls the deviation of the negative binomial from a binomial distribution. As $1/k$ grows large, the negative binomial diverges from a binomial. The sum of the repeated samples from the negative binomial are taken as the multiplicity for the event. To simulate the TPC's efficiency, a multiplicity dependent efficiency is applied - artificially reducing the simulated refmult, with increased reduction at higher refmult. This procedure of sampling (N_{part}, N_{coll}) and generating an event multiplicity is performed many times, producing a simulated multiplicity distribution that can then be fit to the refmultcorr distribution from data.

The three parameters, (x, k, N_{pp}) are optimized by repeatedly generating a new simulated refmult distribution and comparing the simulated distribution to the refmultcorr distribution using a χ^2 test. The set of parameters that generates the smallest χ^2/ndf is chosen as the Glauber distribution which will be used to estimate the centrality definition. The histogram χ^2 is only calculated above a refmult of 100 due to the trigger inefficiencies at low multiplicity. An example of the result of a fit to the refmultcorr can be seen in Figure D.5. The centrality is then calculated by integrating out 5% bins of the Glauber distribution. As an example, if the Glauber multiplicity histogram is normalized to unity, then the 0-5% centrality threshold is defined by summing the high multiplicity tail of the distribution until the total equals 0.05. The refmult where the 0.05 threshold is crossed is taken as the 0-5% refmultcorr threshold. This procedure is repeated in 5% bins from 0-80%. Beyond 80%, this centrality is not used.

The ratio of the Glauber multiplicity and the refmultcorr distributions gives an estimate of the trigger and event reconstruction inefficiency in peripheral events. This ratio is fit with a functional form, and this function is then used to estimate the relative weighting of each recorded event needed to reproduce the Glauber multiplicity distribution. The ratio is shown in the right side of Figure D.5, and the re-weighted refmultcorr compared to the Glauber multiplicity is shown in the bottom plot.

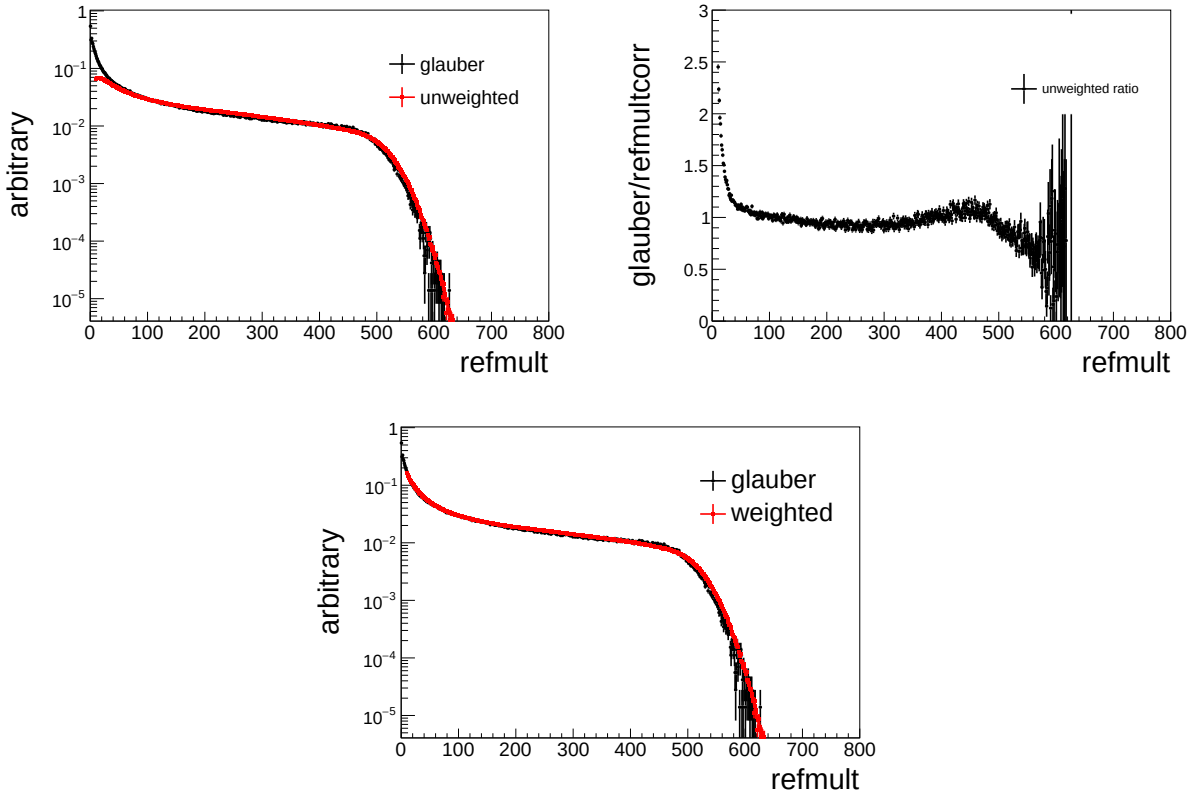

Figure D.5: Left: Glauber multiplicity distribution with minimum χ^2 and the refmultcorr distribution it was fit to. Right: The ratio of Glauber multiplicity to refmultcorr. Bottom: re-weighted refmultcorr compared to Glauber multiplicity.

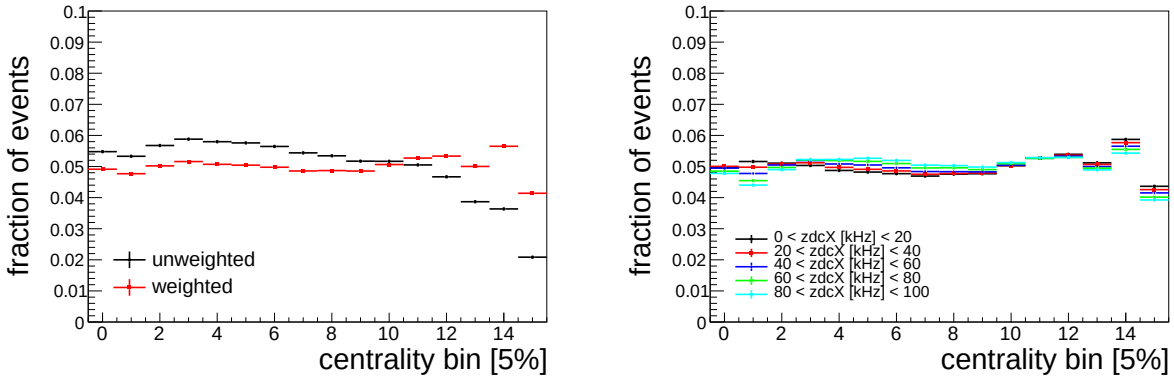

Figure D.6: Left: the number of events per centrality bin with and without re-weighting. Right: the number of events with re-weighting as a function of ZDC coincidence rate.

D.4 Consistency checks

To check that the final centrality definition from the Glauber distribution is consistent, a few consistency checks are performed. The most important is to check that each centrality bin, after re-weighting, has approximately 5% of events. The results are shown on the left side of Figure D.6. On the right side of Figure D.6 is a figure showing the same event fractions as a function of the ZDC coincidence rate. We see that the refmultcorr corrections and Glauber centrality definition is consistent across the full luminosity range.

Appendix E RUN 14 TRACKING EFFICIENCY ESTIMATION

To estimate the efficiency of the TPC in varying conditions (different centralities, increased luminosities, or damaged detector components, for instance), STAR uses a procedure called embedding to estimate both the probability of reconstructing a track given a specific track geometry and momentum (tracking efficiency), as well as the track momentum resolution. In this appendix we will discuss the basic procedure for estimating the efficiency, and will not discuss track momentum resolution.

E.1 Embedding

STAR performs embedding by generating Monte Carlo tracks from an event generator, and running these tracks through a full detector simulation using GEANT [83] which includes interaction with the material of the detector, interactions with the gas in the TPC, and any non-uniformities in the STAR magnetic and electric fields. The simulated track is recorded as a set of TPC space points in the same format as data recorded in the actual detector. These space points are then embedded into a real event that was recorded during data taking. This event with the Monte Carlo generated space points is then run through the full STAR reconstruction chain. If the space charge points that were embedded into the event are successfully reconstructed into a track, that is considered a matched track. The set of all embedded Monte Carlo tracks and all reconstructed matched tracks then allows the calculation of the efficiency of the TPC by taking the ratio of reconstructed/embedded. This is generally done as a function of trackp_{T} and track η.

The general quality of the STAR simulation and embedding can be checked by comparing embedded matched track geometric distributions to real data distributions. Some comparisons using embedded pions are shown in Figure E.1. In general the reconstructed matched tracks match the recorded data (labeled MuDst in the legend) well for η and ϕ, but not as well for the distance of closest approach (DCA) to the primary vertex. The difference in the DCA is thought to be due to two effects. First, DCA gets wider for lower p_{T} tracks. The embedded tracks are sampled from a flat p_{T} distribution, whereas the data distribution is

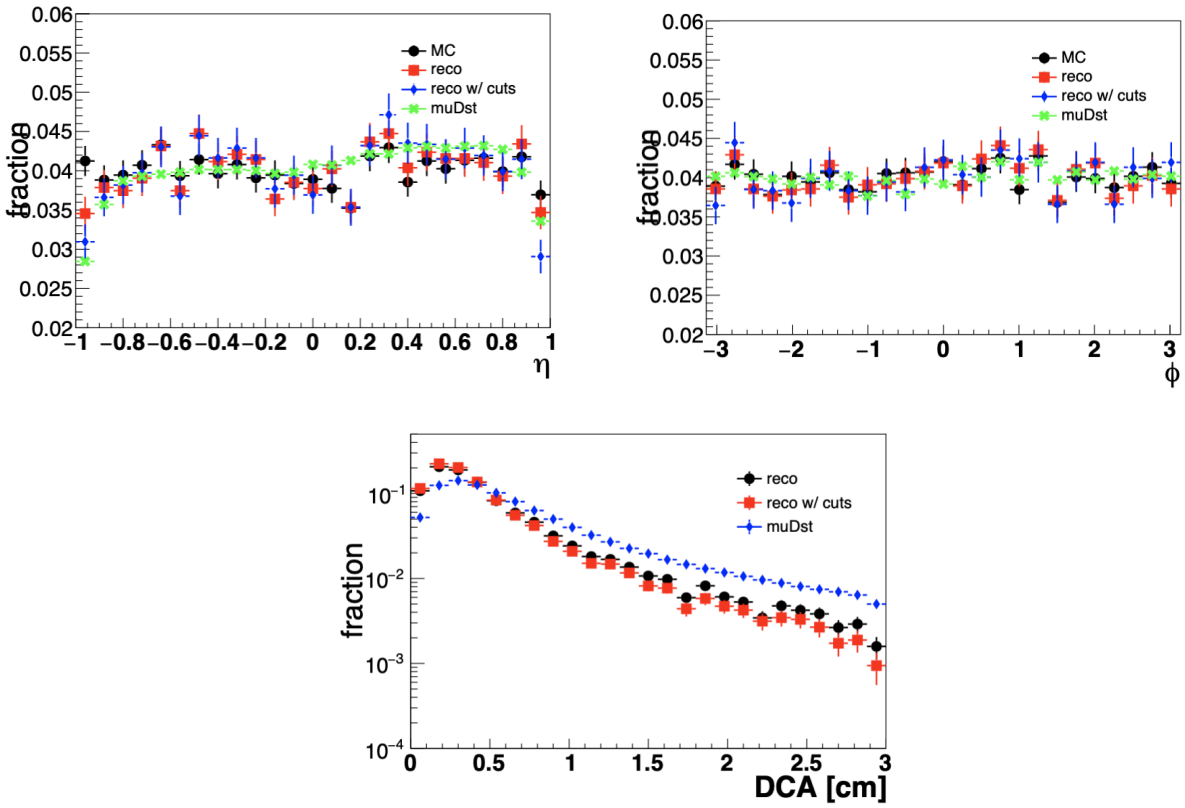

Figure E.1: Quality analysis of the STAR embedding comparing reconstructed matched track, reconstructed matched track with minimal quality cuts, embedded Monte Carlo track, and data track distributions for tracks with $p_{\mathrm{T}} < 1.0$ GeV/c. Left: η distribution. Good agreement between reconstructed tracks and the tracks in data. Right: ϕ distribution. Good agreement between reconstructed tracks and the tracks in data. Bottom: DCA distribution. Data is slightly wider that reconstructed matched tracks. This is probably due to the shape difference in the p_{T} spectra as well as inclusion of secondary vertices in data.

steeply falling. Also, all embedded tracks are embedded such that they point directly to the primary vertex. However, in data secondary vertices naturally occur from decays. These secondary tracks will also widen the DCA distribution. The disagreement in the DCA gets better for higher p_{T} ranges, which is consistent with expectations.

E.2 Efficiencies

The estimation of the efficiency from embedded tracks is done by tacking the ratio of the number of successfully reconstructed tracks to the number of embedded tracks. This is done as a function of track p_{T}, track η and event centrality. Because Run 14 also covers a large

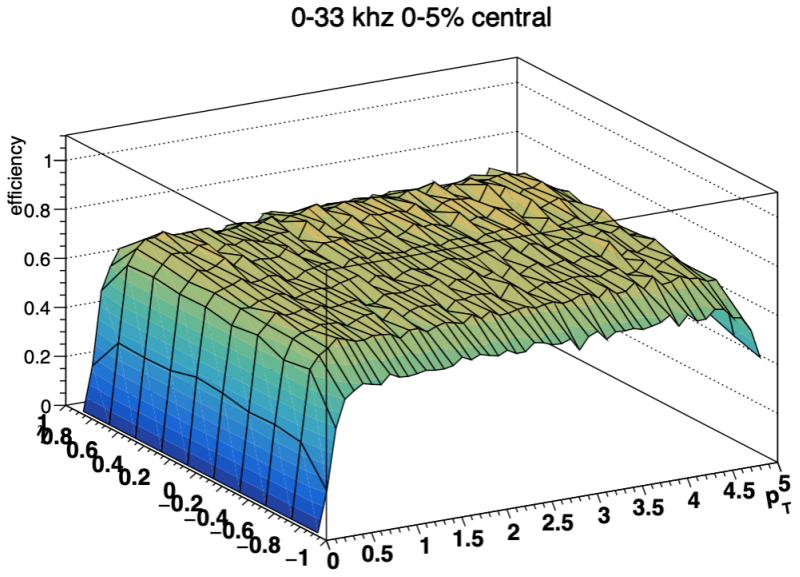

Figure E.2: An example of the 2D tracking efficiency for the most central 5% of collisions with a ZDC coincidence rate less than 33 kHz as a function of track p_{T} and track η. Tracking efficiency is approximately constant above p_{T} of 1 GeV/c, and degrades significantly below 1.0 GeV/c. Tracking efficiency also slightly degrades as η approached ± 1.0.

luminosity range that can have an effect on the tracking efficiency, the efficiency estimation is also done as a function of the ZDC coincidence rate, as an stand-in for the luminosity and TPC occupancy.

An example of the 2D (p_{T} η) efficiency for a single centrality and ZDC coincidence rate bin is shown in Figure E.2.

Projections showing the tracking efficiency only as a function of p_{T} are shown in Figure E.3 for different centralities and luminosities. In general, more central events have lower overall efficiency. We also see that for all centralities and p_{T} ranges, the low luminosity efficiencies are systematically higher than the high luminosity efficiencies. This is consistent with the predicted luminosity dependent efficiency due to increased TPC occupancy.

NOTE: these efficiency curves were produced with the known buggy P17id library and are known to not be correct. These are shown to illustrate the trends and show the work that was performed for this dissertation.

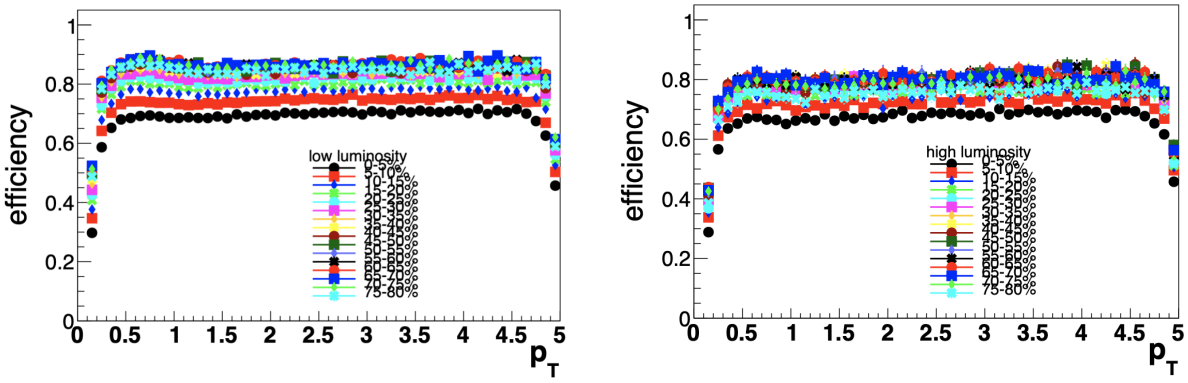

Figure E.3: Examples of the tracking efficiency as a function of the track p_{T} for various centralities. Left: tracking efficiency for a ZDC coincidence rate less than 33 kHz. Right: tracking efficiency for events with a ZDC coincidence rate greater than 66 kHz. The fall off at $p_{\mathrm{T}} > 4.5$ GeV/c is due to the fact that the Monte Carlo tracks are generated with $p_{\mathrm{T}} < 5.0$ GeV/c. Because of the finite p_{T} resolution, tracks can feed out of the p_{T} range shown without compensation from feed in from higher p_{T} ranges. Because of this, these curves are only used out to 4.5 GeV/c, and the efficiencies are assumed to be constant beyond that point.

Appendix F FURTHER ANALYSIS DETAILS AND SYSTEMATIC UNCERTAINTIES

In this appendix we present further details and the systematic uncertainties of the di-jet hadron correlations and differential di-jet imbalance.

F.1 Di-jet hadron correlations

F.1.1 Background subtraction

As described in Chapter 6, background subtraction is performed on the di-jet hadron correlations for both the trigger and recoil jet correlations, as well as in $\Delta\eta$ and $\Delta\phi$. The description of these methods can be seen in Section 6.5. Here we show the fits and projections for each $p_{\mathrm{T}}^{\mathrm{assoc}}$ bin. Because of the lack of background above $p_{\mathrm{T}} = 4$ GeV/c and the difficulty of fitting a single bin with a gaussian, no background subtraction is done for $p_{\mathrm{T}} > 4$ GeV/c for the $\Delta\eta$ projections.

$\Delta\eta$ trigger jet fits

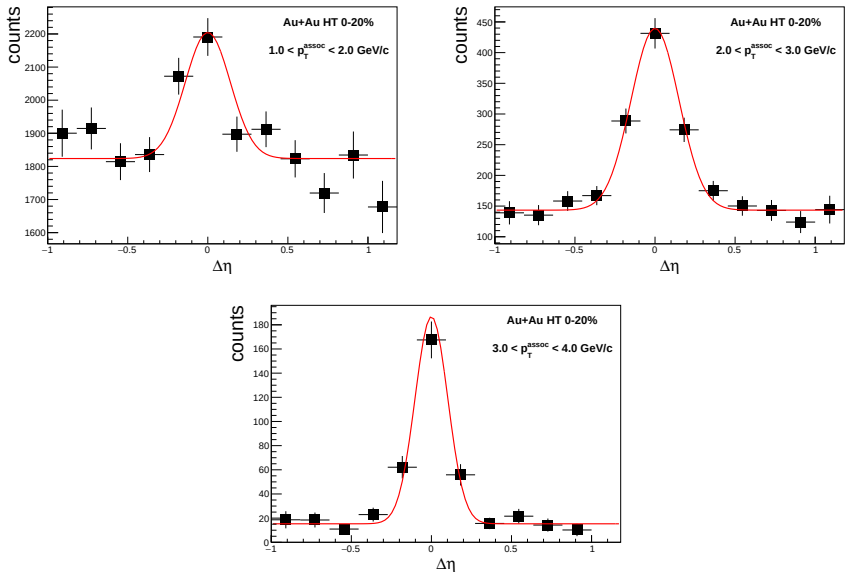

Figure F.1: $\Delta\eta$ fits for the trigger jet hadron correlations in bins of $p_{\mathrm{T}}^{\mathrm{assoc}}$ for Au+Au.

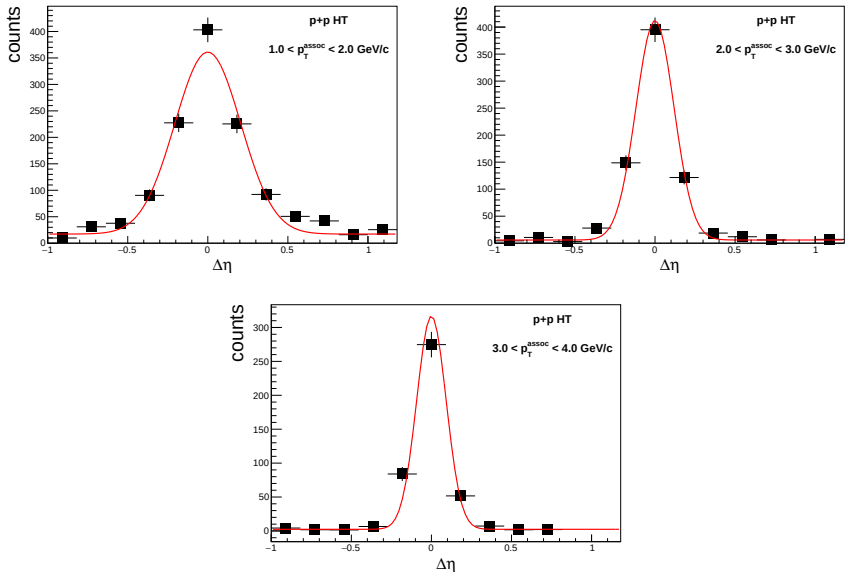

Figure F.2: $\Delta\eta$ fits for the trigger jet hadron correlations in bins of $p_{\mathrm{T}}^{\mathrm{assoc}}$ for $p+p$.

$\Delta\eta$ recoil jet fits

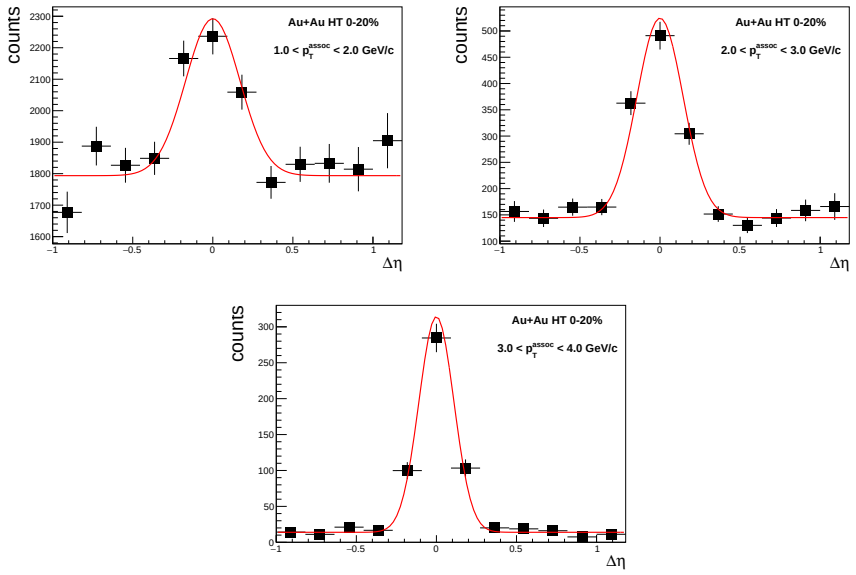

Figure F.3: $\Delta\eta$ fits for the recoil jet hadron correlations in bins of $p_{\mathrm{T}}^{\mathrm{assoc}}$ for Au+Au.

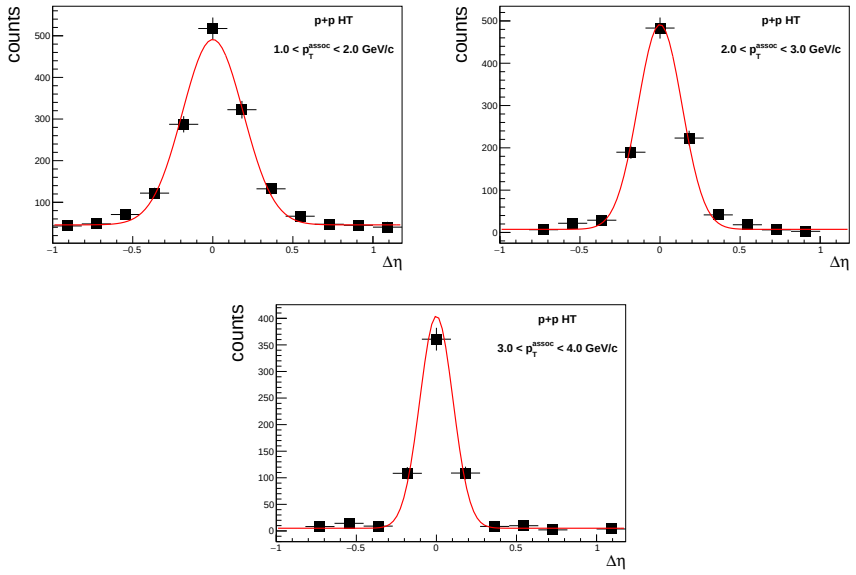

Figure F.4: $\Delta\eta$ fits for the recoil jet hadron correlations in bins of $p_{\mathrm{T}}^{\mathrm{assoc}}$ for $p+p$.

$\Delta\phi$ trigger sideband subtraction

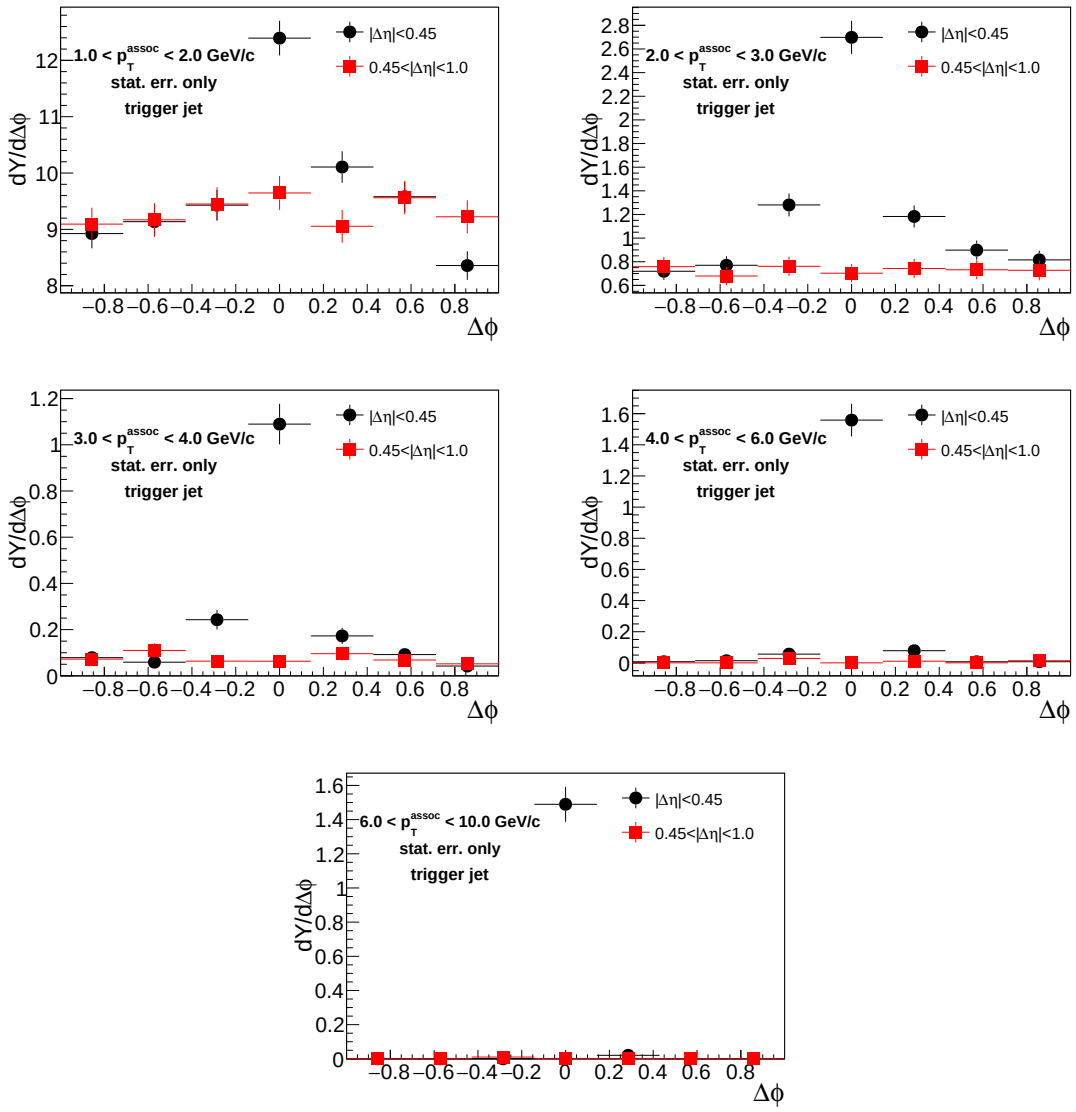

Figure F.5: $\Delta\phi$ signal and sideband for the trigger jet hadron correlations in bins of $p_{\mathrm{T}}^{\mathrm{assoc}}$ for Au+Au.

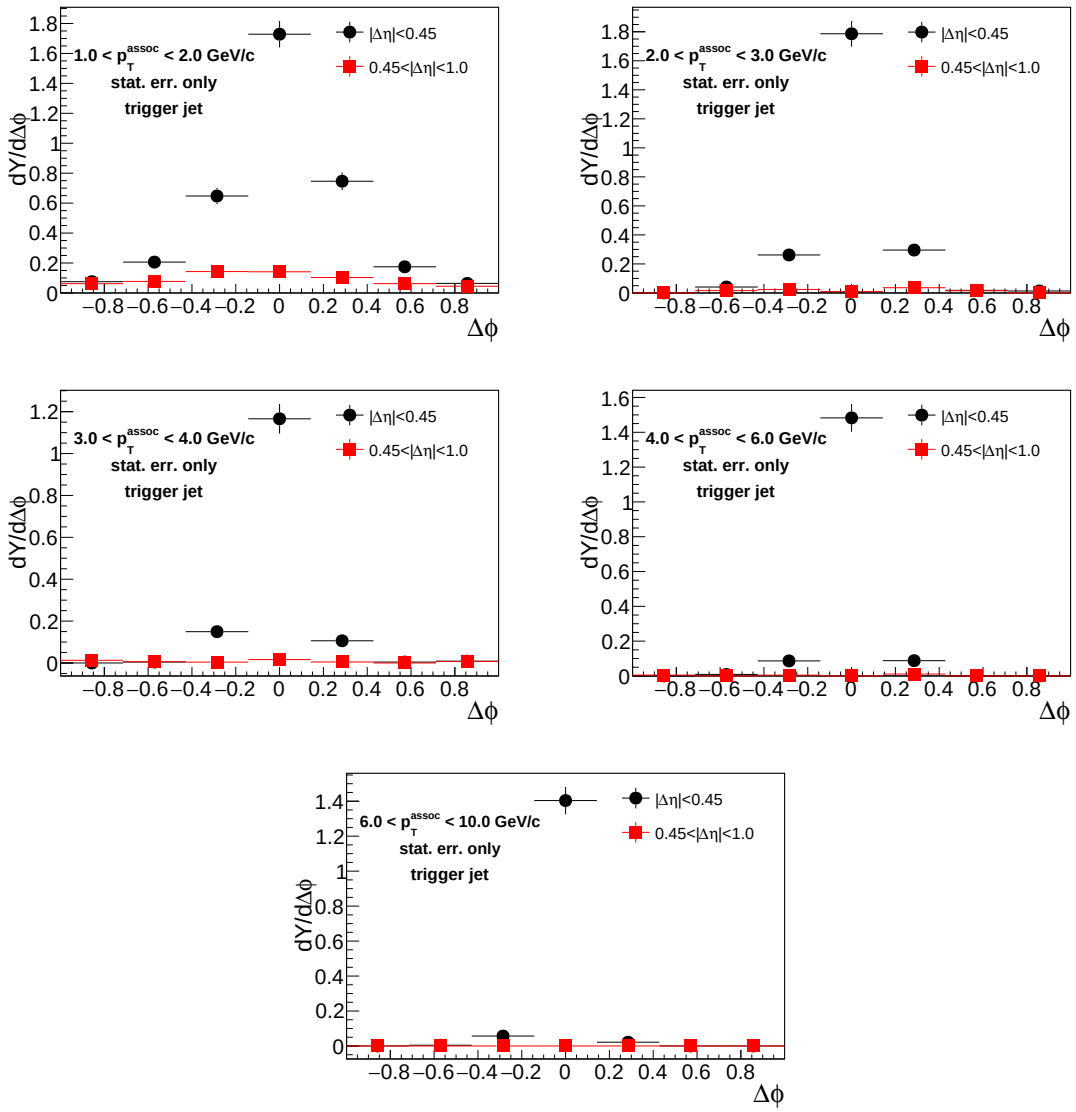

Figure F.6: $\Delta\phi$ signal and sideband for the trigger jet hadron correlations in bins of $p_{\mathrm{T}}^{\mathrm{assoc}}$ for $p+p$.

$\Delta\phi$ recoil jet sideband subtraction

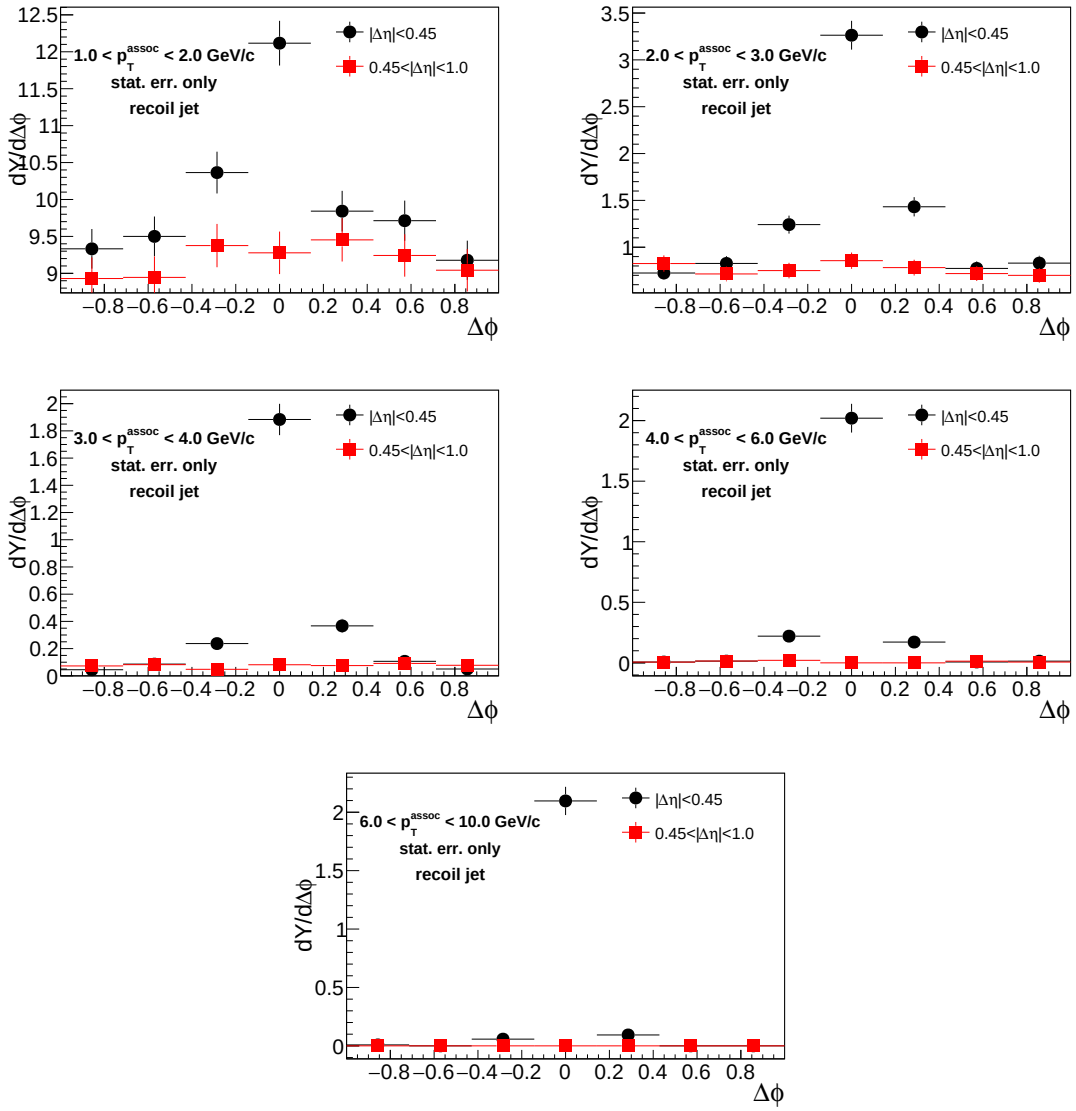

Figure F.7: $\Delta\phi$ signal and sideband for the recoil jet hadron correlations in bins of $p_{\mathrm{T}}^{\mathrm{assoc}}$ for Au+Au.

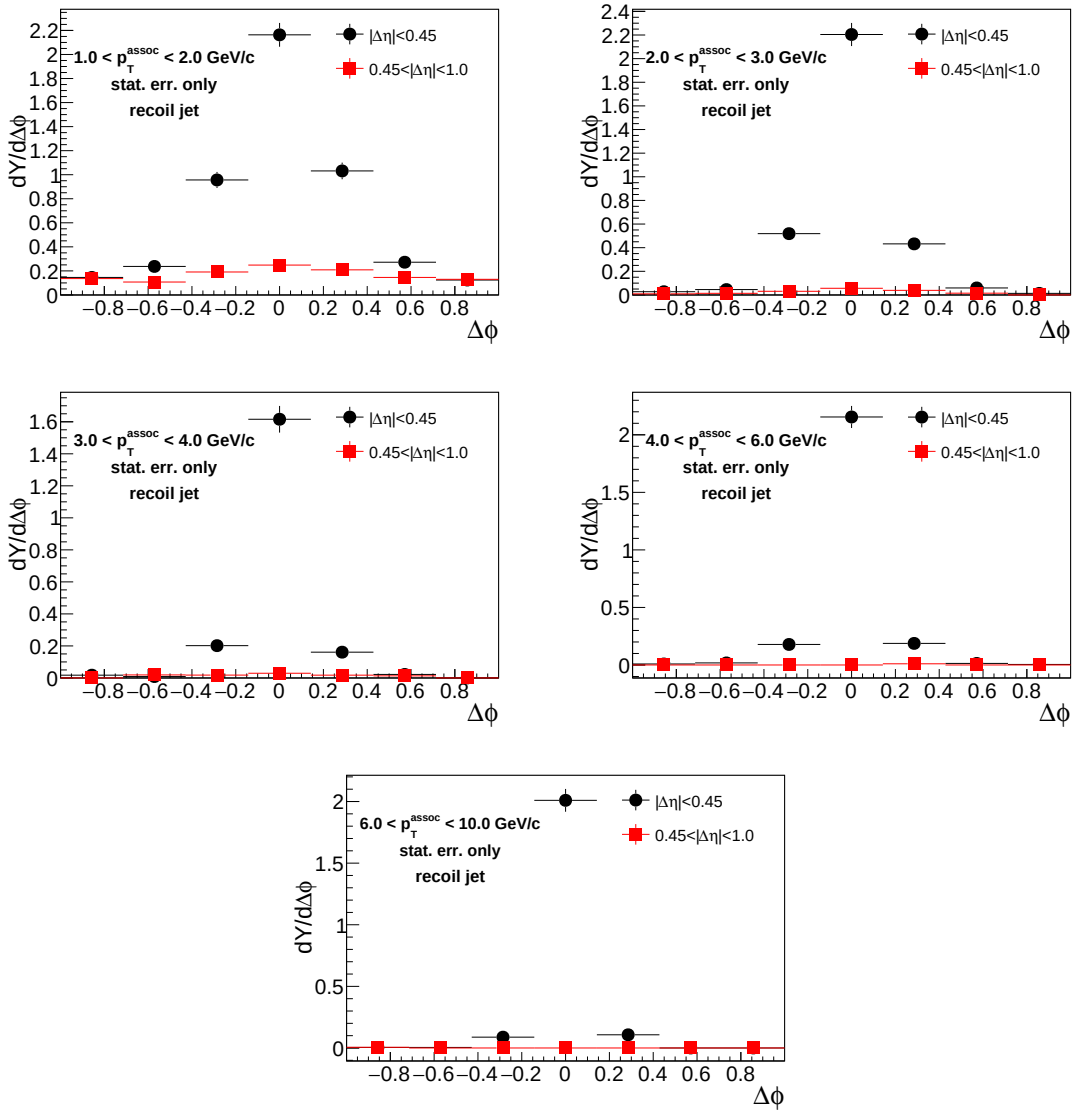

Figure F.8: $\Delta\phi$ signal and sideband for the recoil jet hadron correlations in bins of $p_{\mathrm{T}}^{\mathrm{assoc}}$ for $p+p$.

F.1.2 Systematic uncertainty

As described in Chapter 6, three sources of uncertainty are assessed: the absolute tracking efficiency uncertainty, the relative tower energy scale uncertainty between Run 6 and Run 7 data, and the relative tracking efficiency uncertainty between Run 6 and Run 7 data. The absolute tracking efficiency uncertainty is taken as 5% [58] bin-by-bin. Because it is constant percent of the nominal bin contents, the values are not shown separately here, as they can be inferred from the correlation and yield plots presented earlier. The uncertainty due to the relative tracking efficiency and relative tower energy scale uncertainties (together called the jet energy scale uncertainty) on the correlations and yields are assessed by performing the analysis on the embedded $p+p$ four times: twice by varying the tower energy scale up and down by 2% during jetfinding, and twice by varying the relative tracking efficiency between $p+p$ and Au+Au up and down by 7% during jetfinding. Because these uncertainties are uncorrelated, the cross terms (varying the tower energy scale and tracking efficiency at the same time) are neglected. The correlations and yields are estimated in the four cases, and the uncertainty on each bin due to the tower scale or tracking is taken to be the difference between the positive and negative variations. The jet energy scale uncertainty is then taken as the quadrature sum of the tower energy scale and relative tracking uncertainties.

Relative tracking efficiency uncertainty, trigger jet

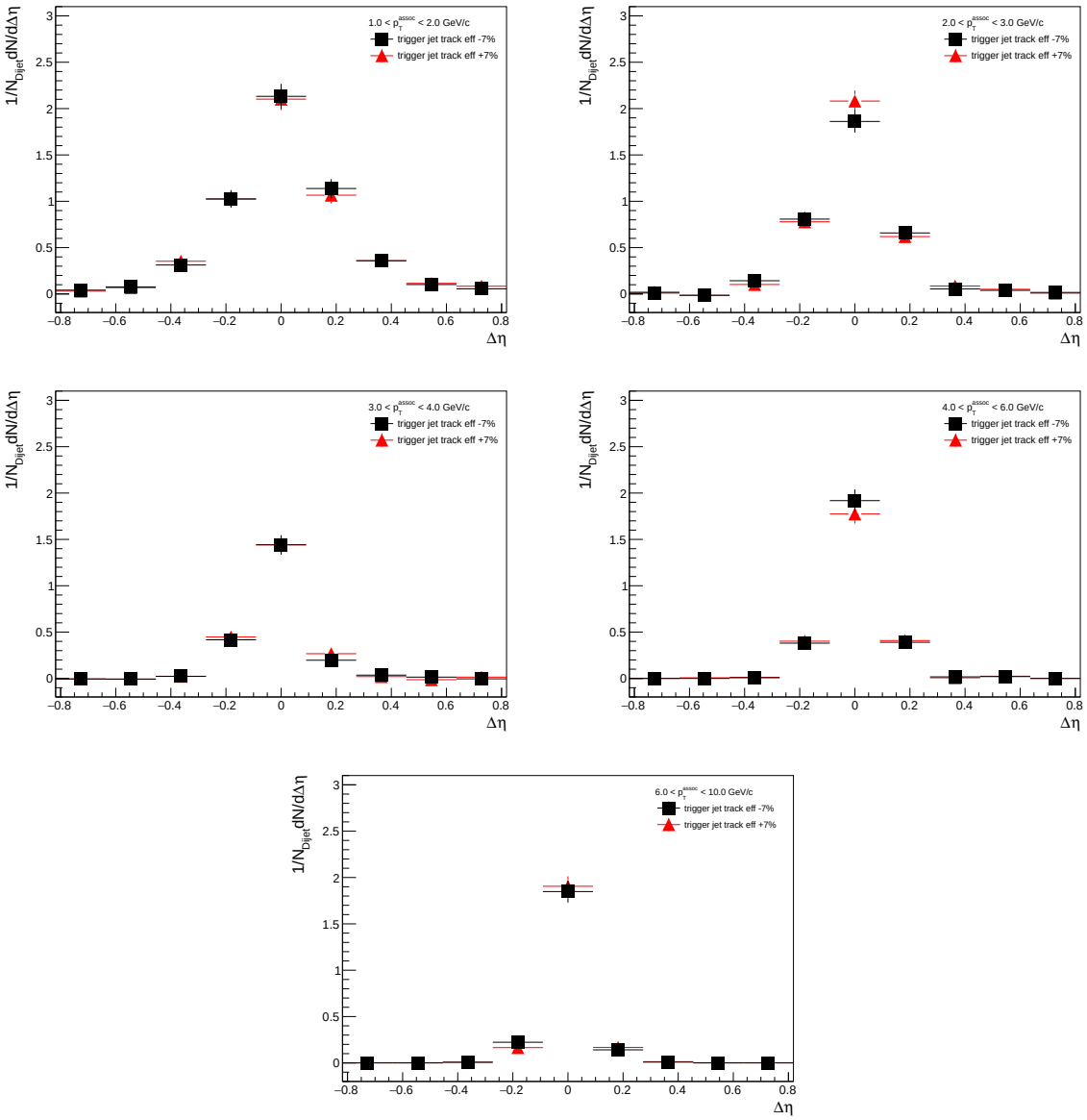

Figure F.9: Jet-hadron correlations in $\Delta\eta$ for the trigger jet and associated hadrons with variations on the tracking efficiency.

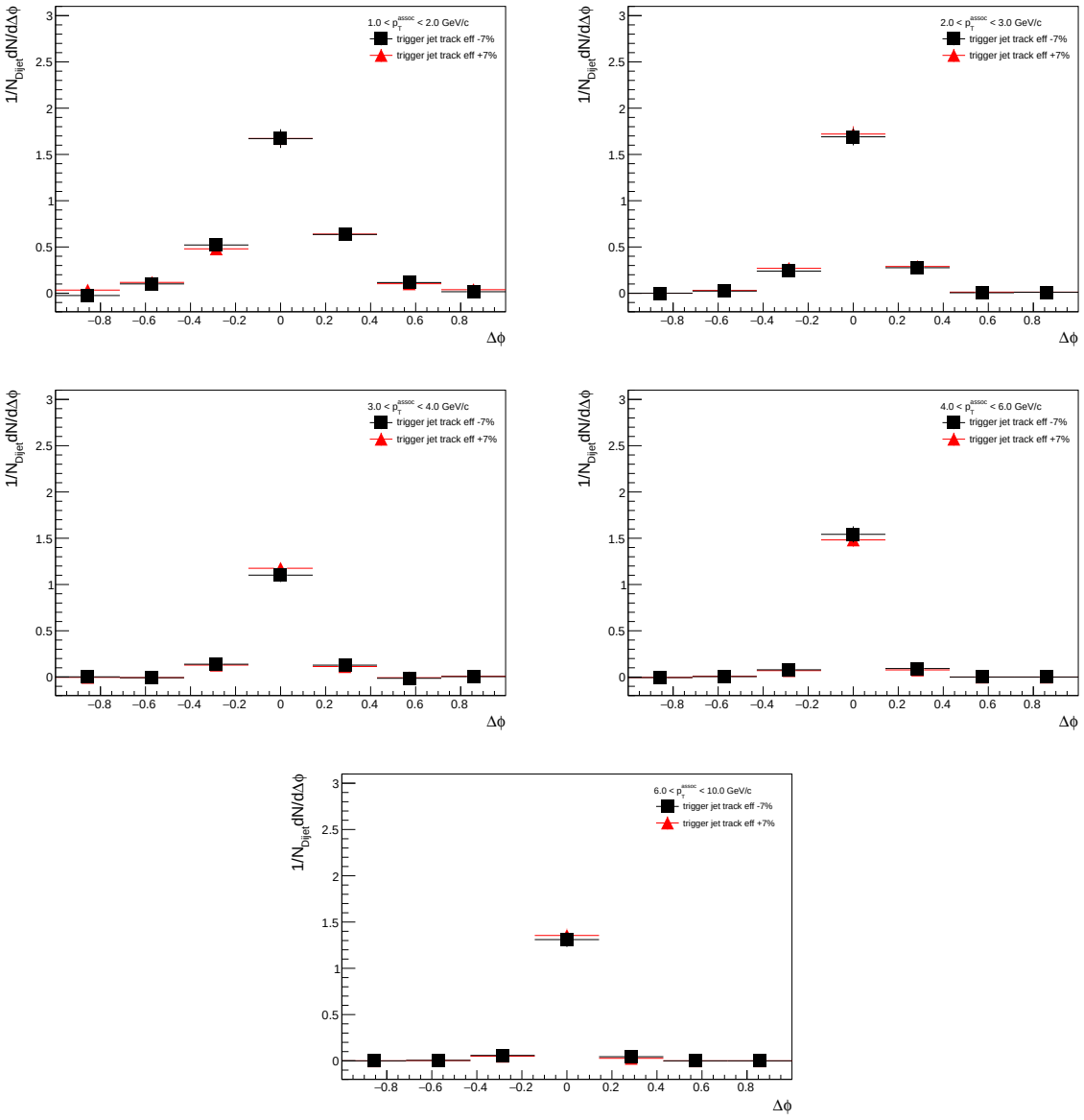

Figure F.10: Jet-hadron correlations in $\Delta\phi$ for the trigger jet and associated hadrons with variations on the tracking efficiency.

Relative tracking efficiency uncertainty, recoil jet

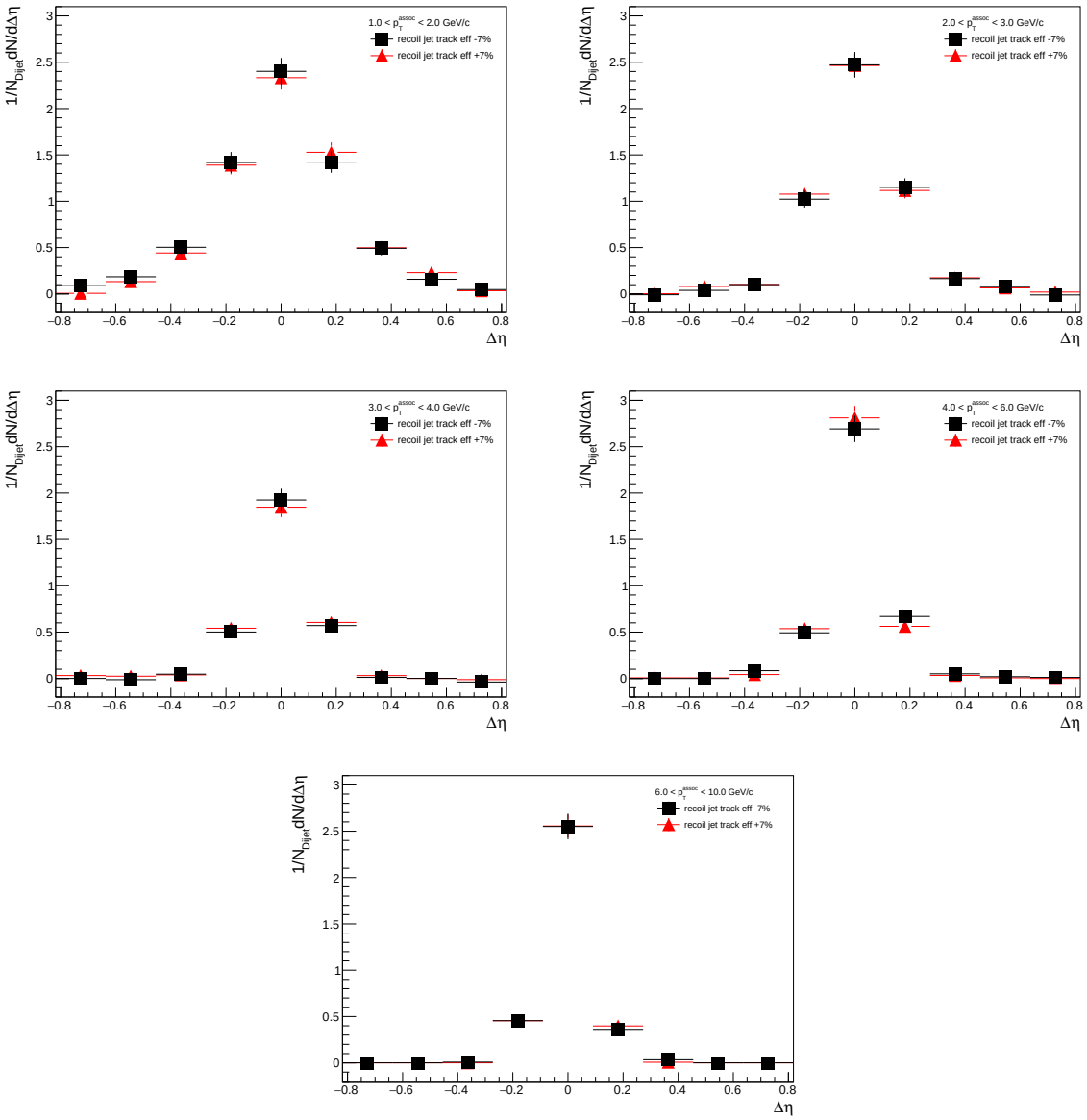

Figure F.11: Jet-hadron correlations in $\Delta\eta$ for the recoil jet and associated hadrons with variations on the tracking efficiency.

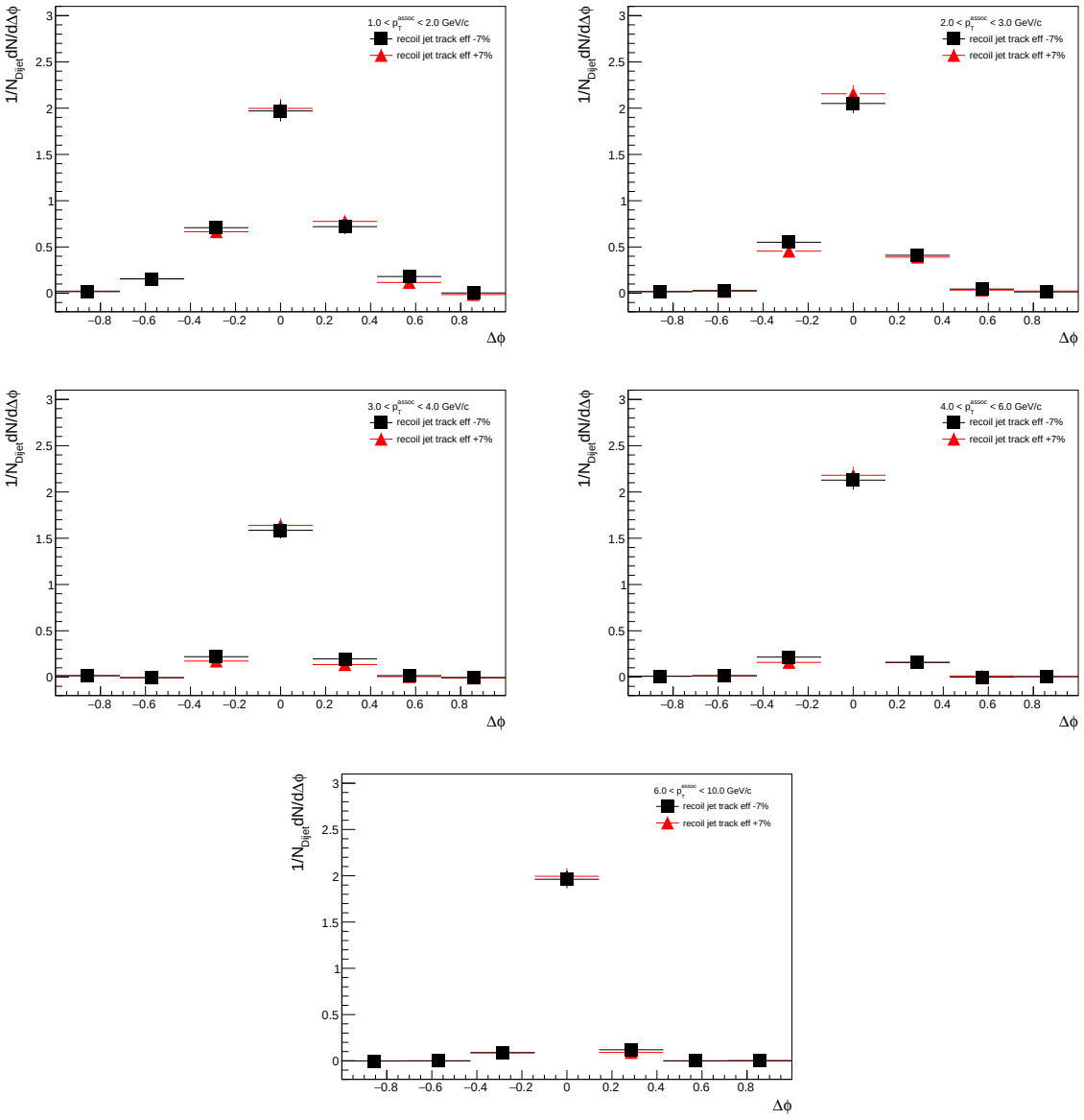

Figure F.12: Jet-hadron correlations in $\Delta\phi$ for the recoil jet and associated hadrons with variations on the tracking efficiency.

Relative tower energy scale uncertainty, trigger jet

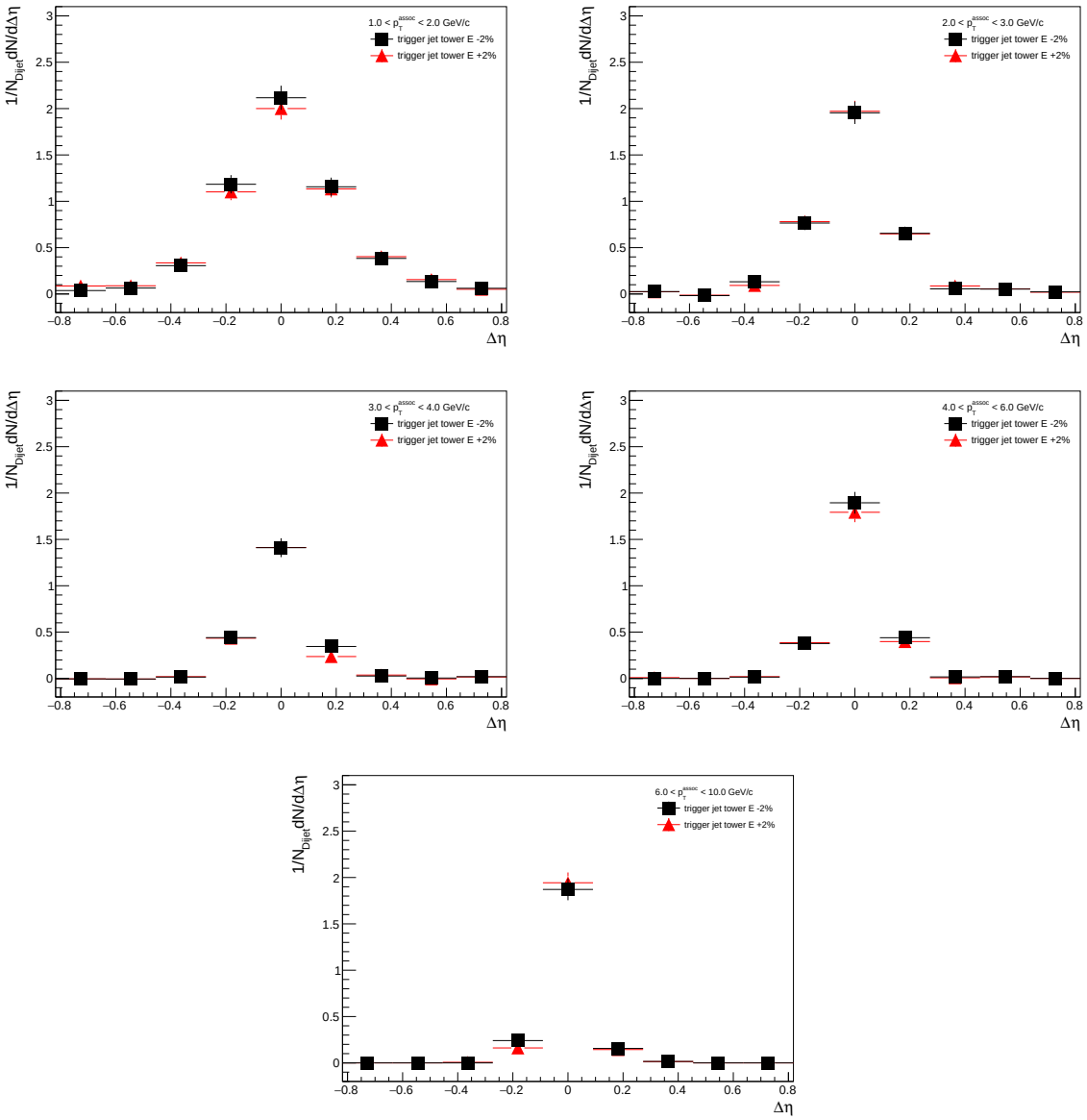

Figure F.13: Jet-hadron correlations in $\Delta\eta$ for the trigger jet and associated hadrons with variations on the tower energy scale.

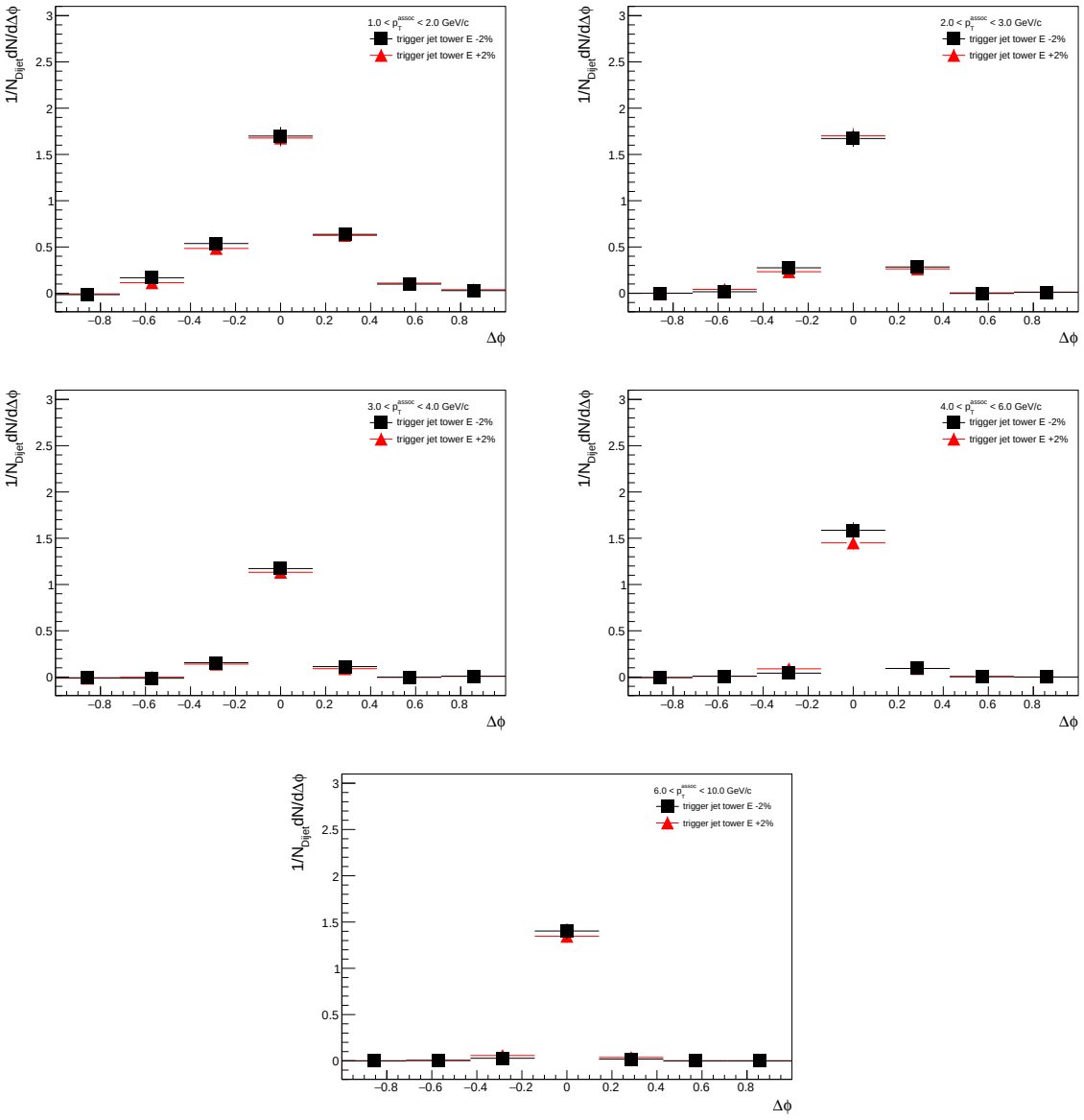

Figure F.14: Jet-hadron correlations in $\Delta\phi$ for the trigger jet and associated hadrons with variations on the tower energy scale.

Relative tower energy scale uncertainty, recoil jet

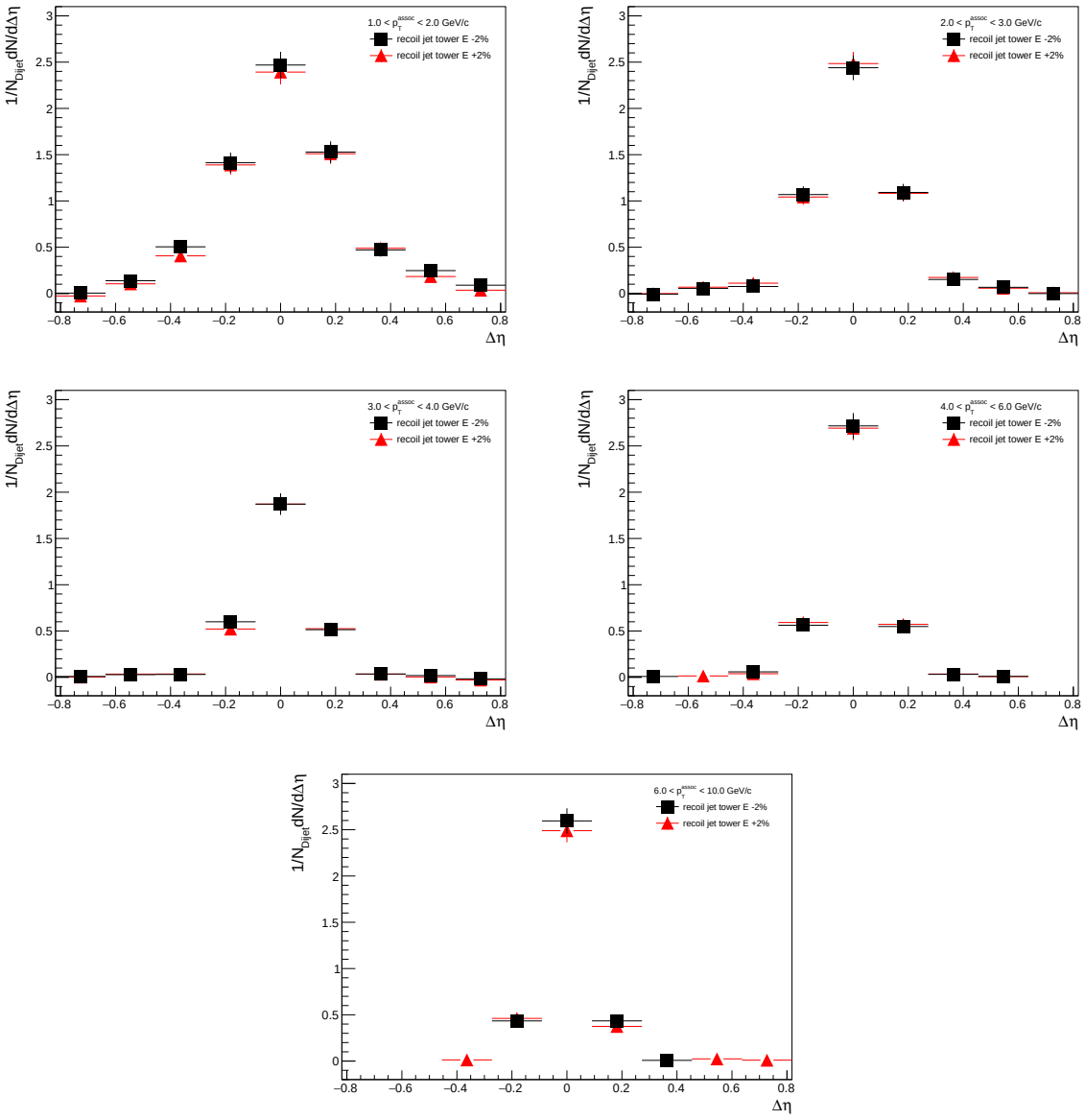

Figure F.15: Jet-hadron correlations in $\Delta\eta$ for the recoil jet and associated hadrons with variations on the tower energy scale.

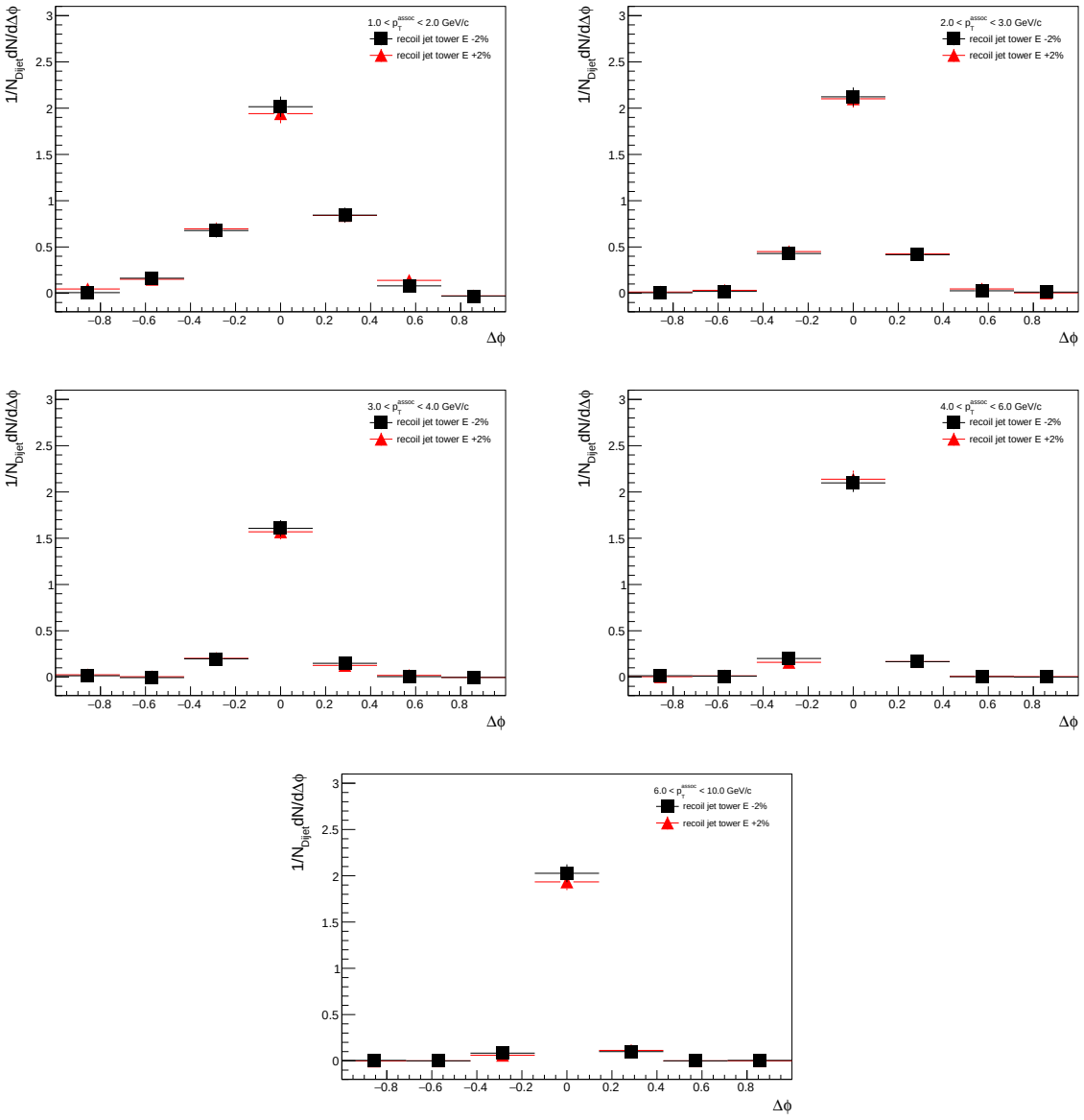

Figure F.16: Jet-hadron correlations in $\Delta\phi$ for the recoil jet and associated hadrons with variations on the tower energy scale.

Total jet energy scale uncertainty

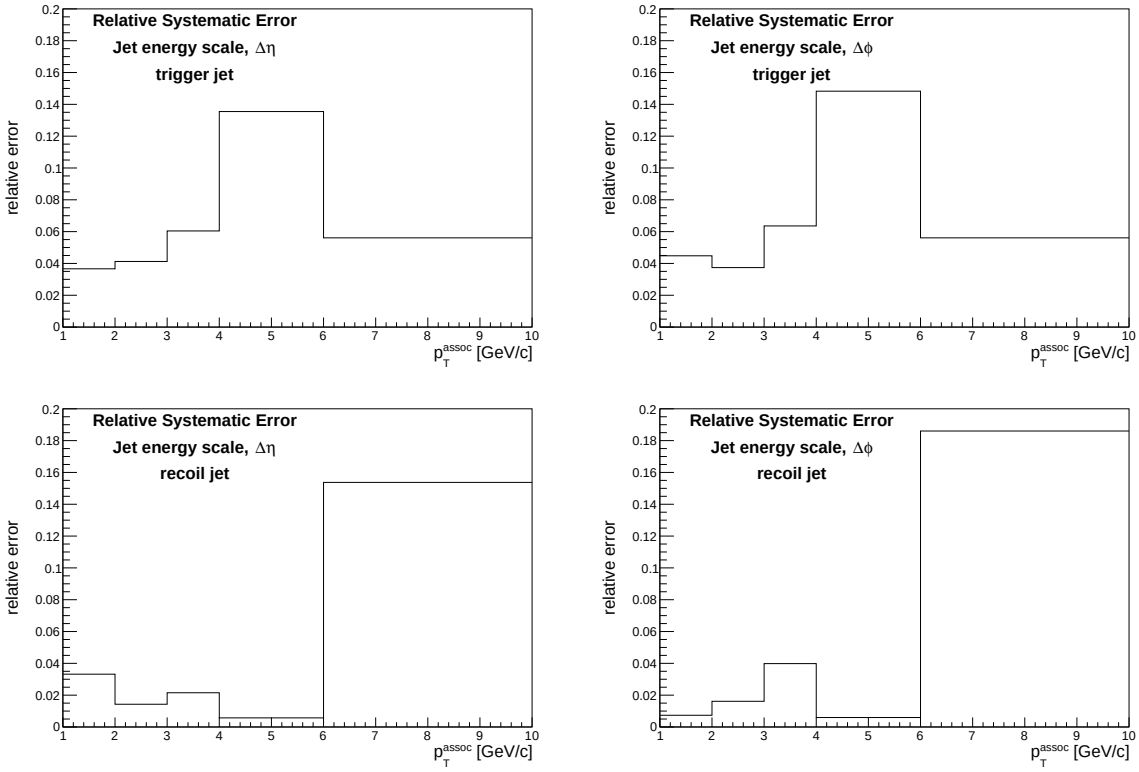

Figure F.17: Total jet energy scale uncertainty shown as a percent of the yield for trigger and recoil jet associated yield, in $\Delta\eta$ and $\Delta\phi$.

F.2 Differential di-jet imbalance

As described in Chapter 7, we analyze two sources of uncertainty: the relative tracking efficiency between Au+Au and $p + p$, and the relative tower energy scale. The effect of these uncertainties is estimated by varying the relative tracking efficiency and tower energy scale by $\pm 7\%$ and $\pm 2\%$ respectively in the embedded $p + p$ and re-running the analysis with the modified value. The uncertainty on each A_J bin due to one of the uncertainties is then taken as the maximum absolute difference between the nominal bin content and the two variations (increased or decreased tracking efficiency, for instance). Since the two sources are uncorrelated, they are varied independently and the final systematic uncertainty is taken as the quadrature sum of the two.

F.2.1 Hard-core di-jets

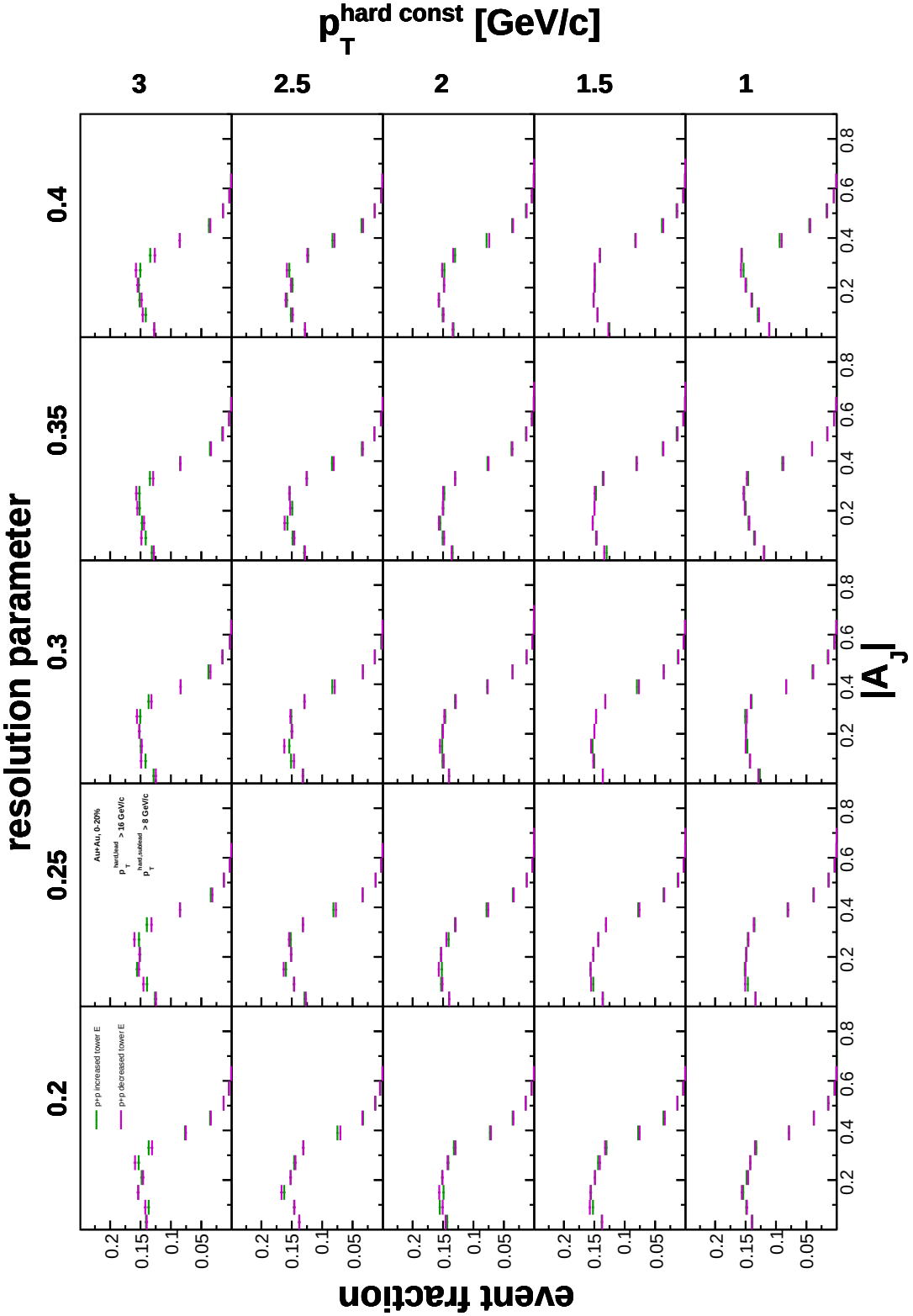

Figure F.18: $|A_J|$ distributions for all di-jet definitions varying $p_{\mathrm{T}}^{\mathrm{const}}$ and R for embedded $p+p$ hard-core di-jets while varying the tower energy scale by $\pm 2\%$.

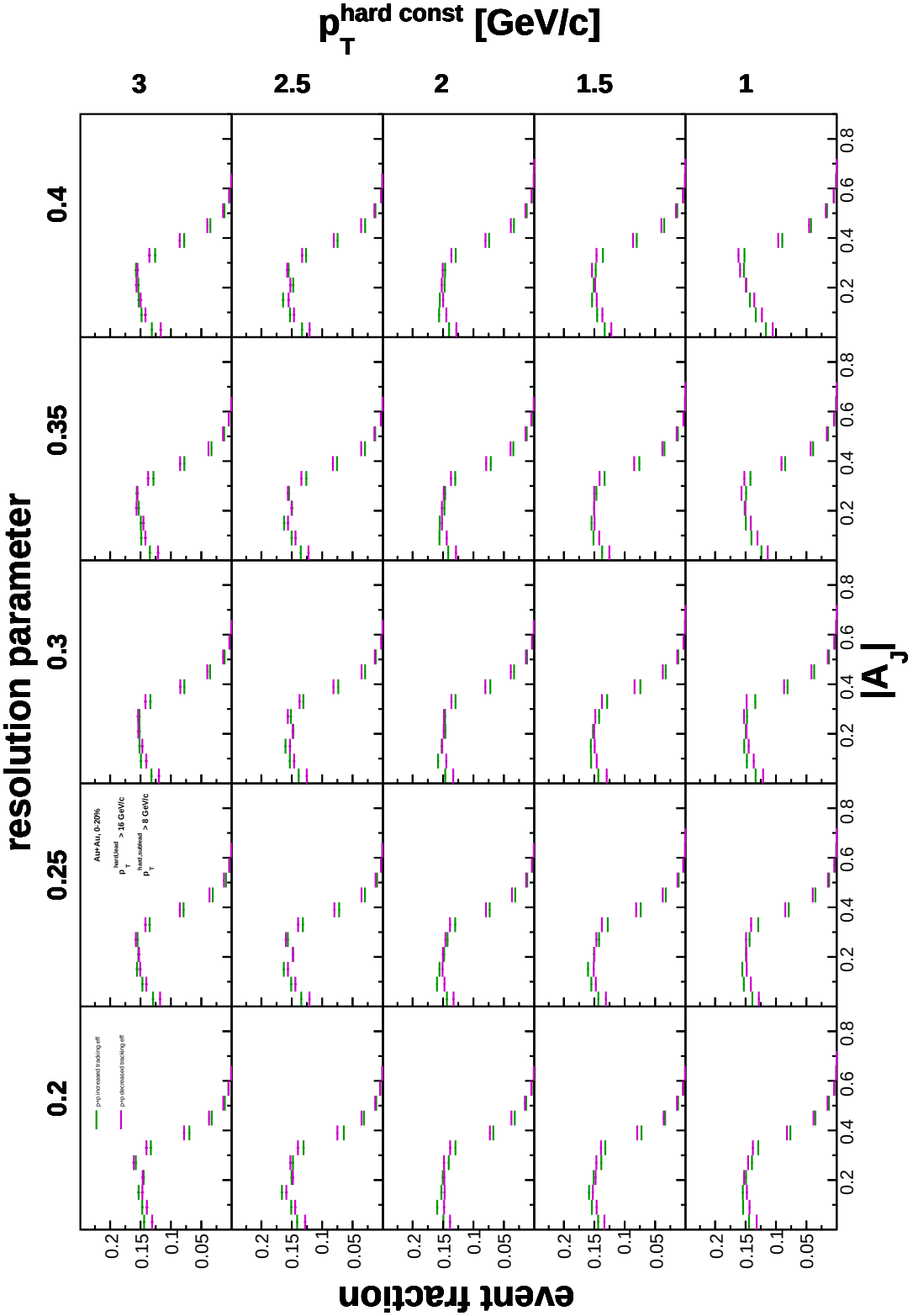

Figure F.19: $|A_J|$ distributions for all di-jet definitions varying $p_{\mathrm{T}}^{\mathrm{const}}$ and R for embedded $p+p$ hard-core di-jets while varying the relative tracking efficiency by $\pm 7\%$.

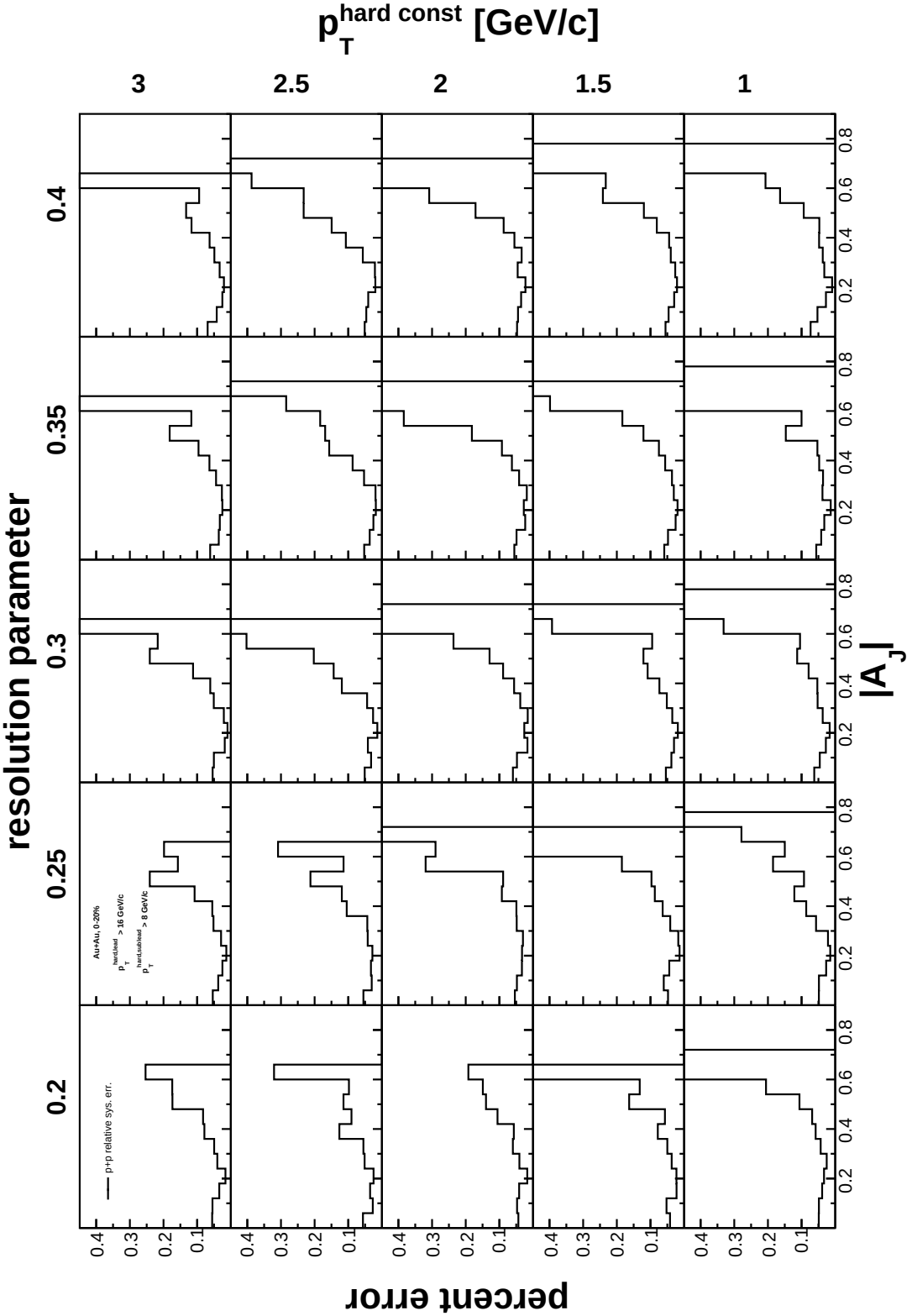

Figure F.20: Relative systematic errors for all di-jet definitions varying $p_{\mathrm{T}}^{\mathrm{const}}$ and R for embedded $p+p$ hard-core di-jets.

F.2.2 Matched di-jets

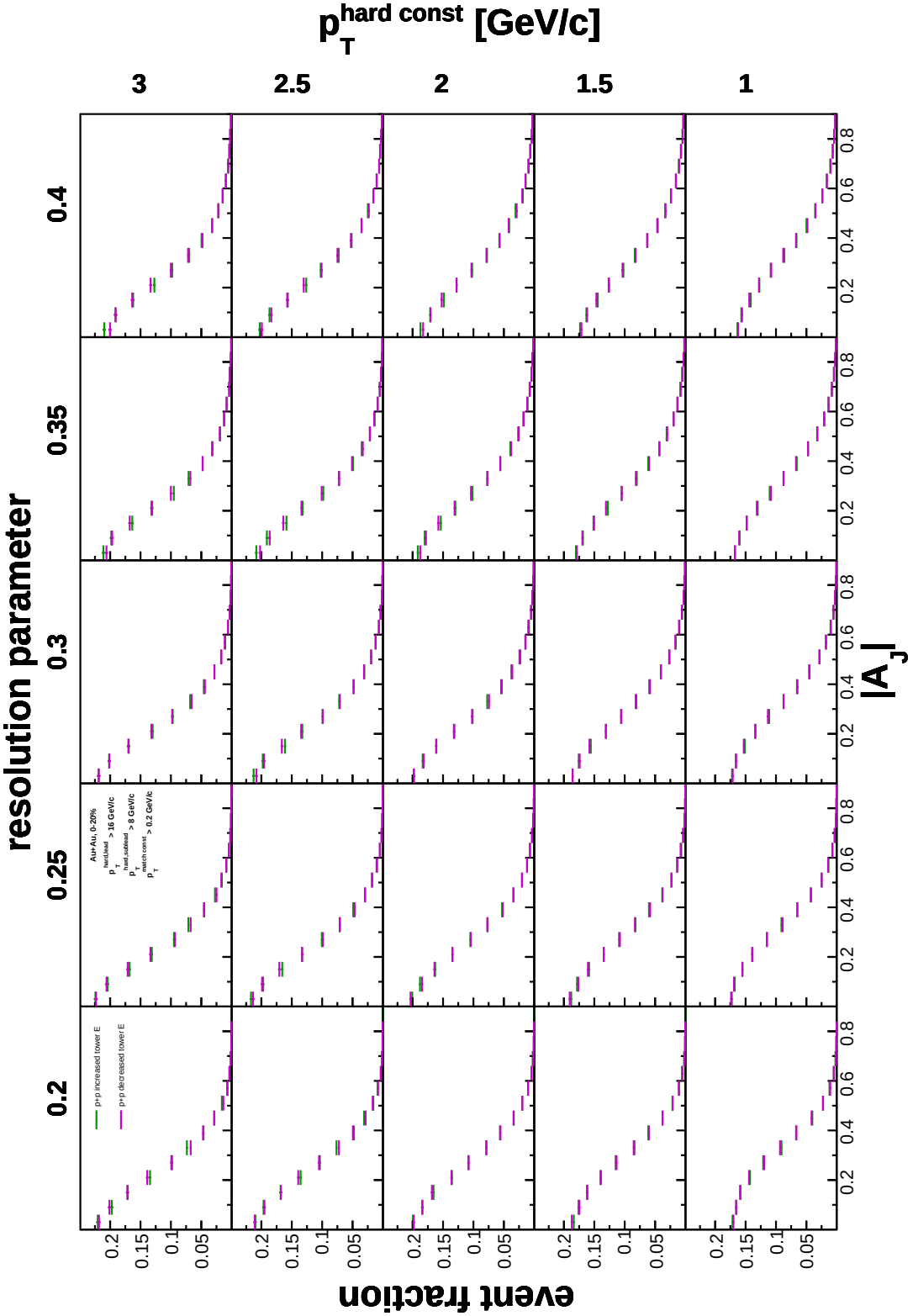

Figure F.21: $|A_J|$ distributions for all di-jet definitions varying $p_{\mathrm{T}}^{\mathrm{const}}$ and R for embedded $p+p$ matched di-jets while varying the tower energy scale by $\pm 2\%$.

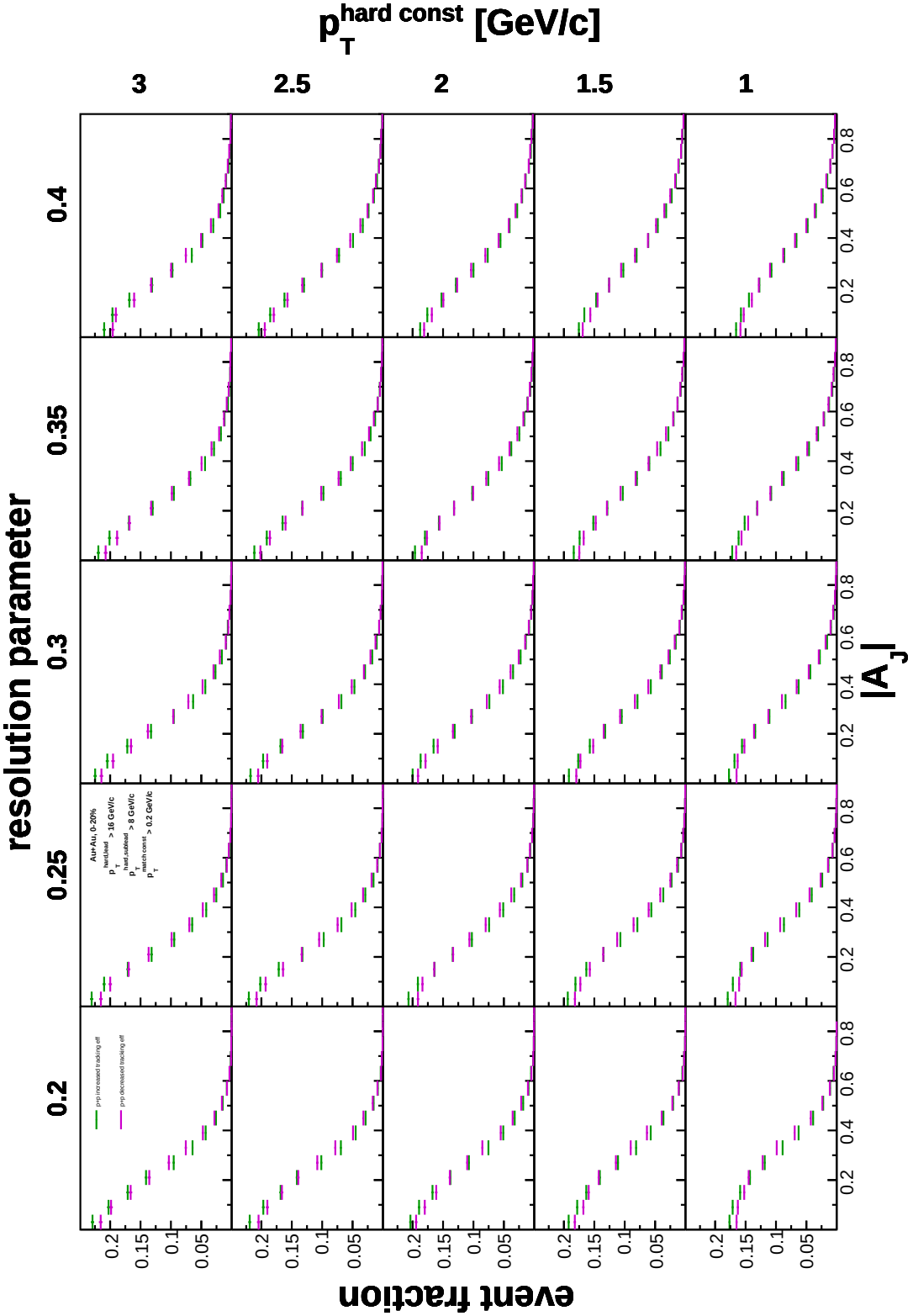

Figure F.22: $|A_J|$ distributions for all di-jet definitions varying $p_{\mathrm{T}}^{\mathrm{const}}$ and R for embedded $p+p$ matched di-jets while varying the relative tracking efficiency by $\pm 7\%$.

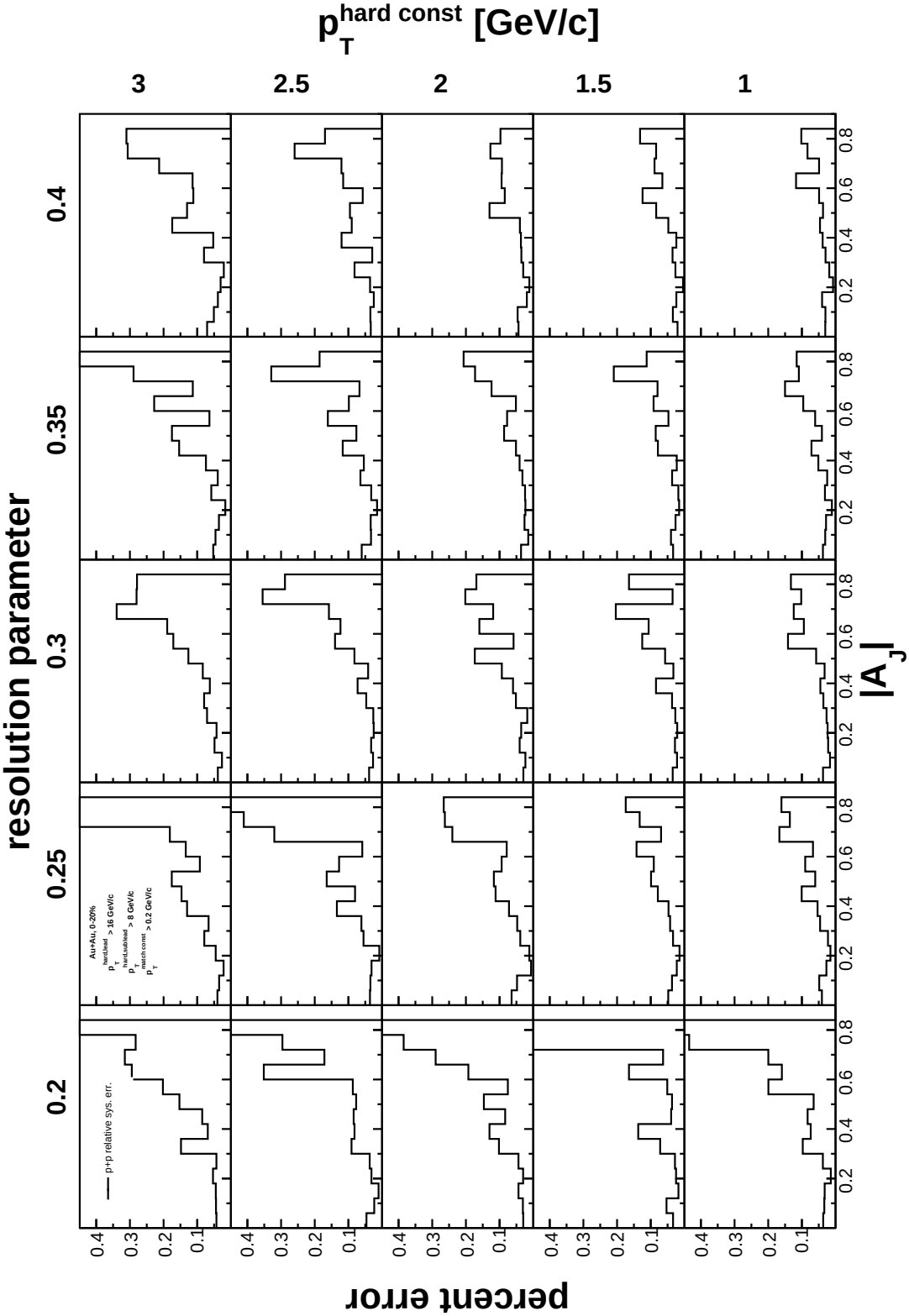

Figure F.23: Relative systematic errors for all di-jet definitions varying $p_{\mathrm{T}}^{\mathrm{const}}$ and R for embedded $p+p$ matched di-jets.

F.2.3 Radial scan matched di-jets

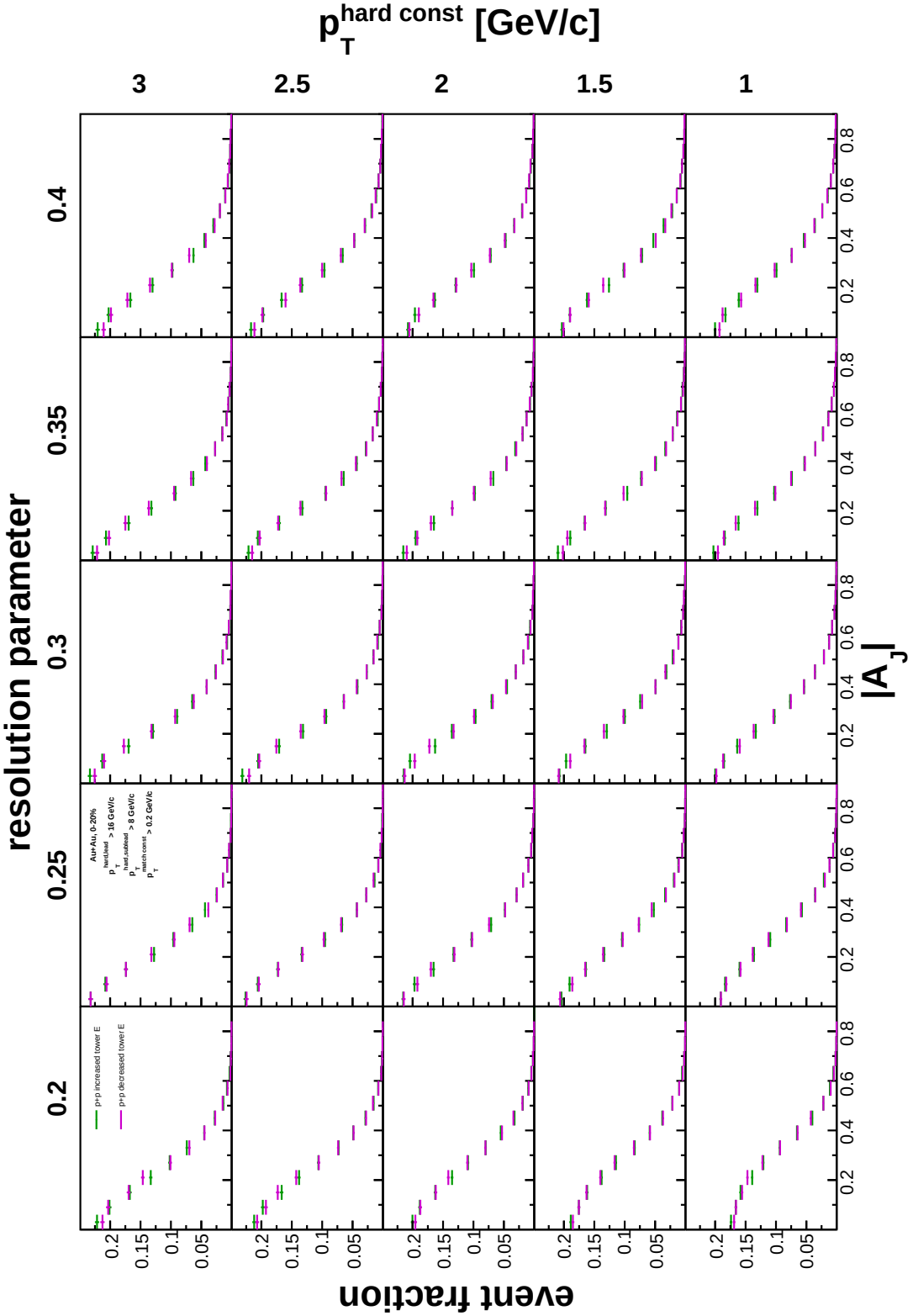

Figure F.24: $|A_J|$ distributions for all di-jet definitions varying $p_{\mathrm{T}}^{\mathrm{const}}$ and R for embedded $p+p$ matched di-jets in the radial scan while varying the tower energy scale by $\pm 2\%$.

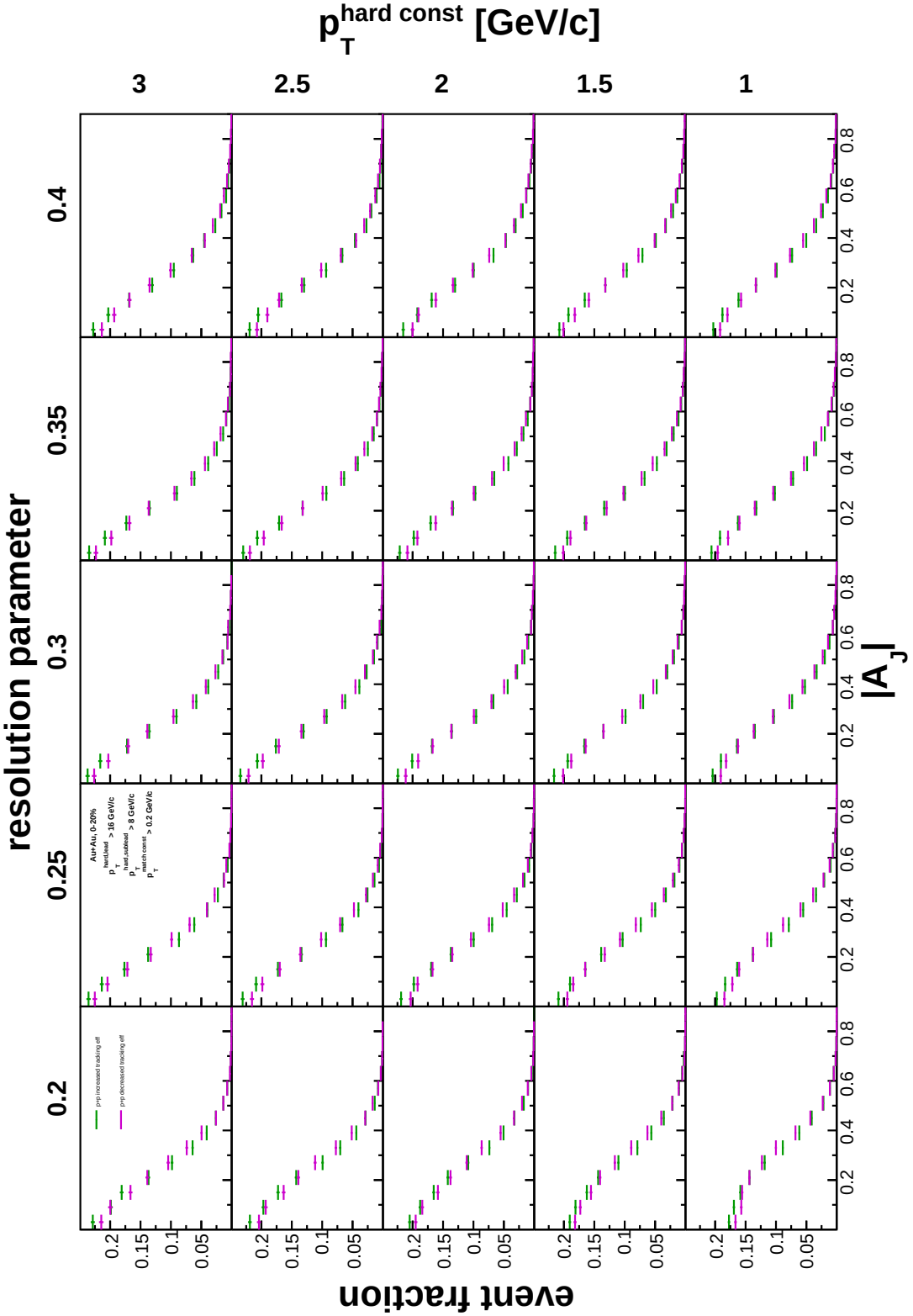

Figure F.25: $|A_J|$ distributions for all di-jet definitions varying $p_{\mathrm{T}}^{\mathrm{const}}$ and R for embedded $p+p$ matched di-jets in the radial scan while varying the relative tracking efficiency by $\pm 7\%$.

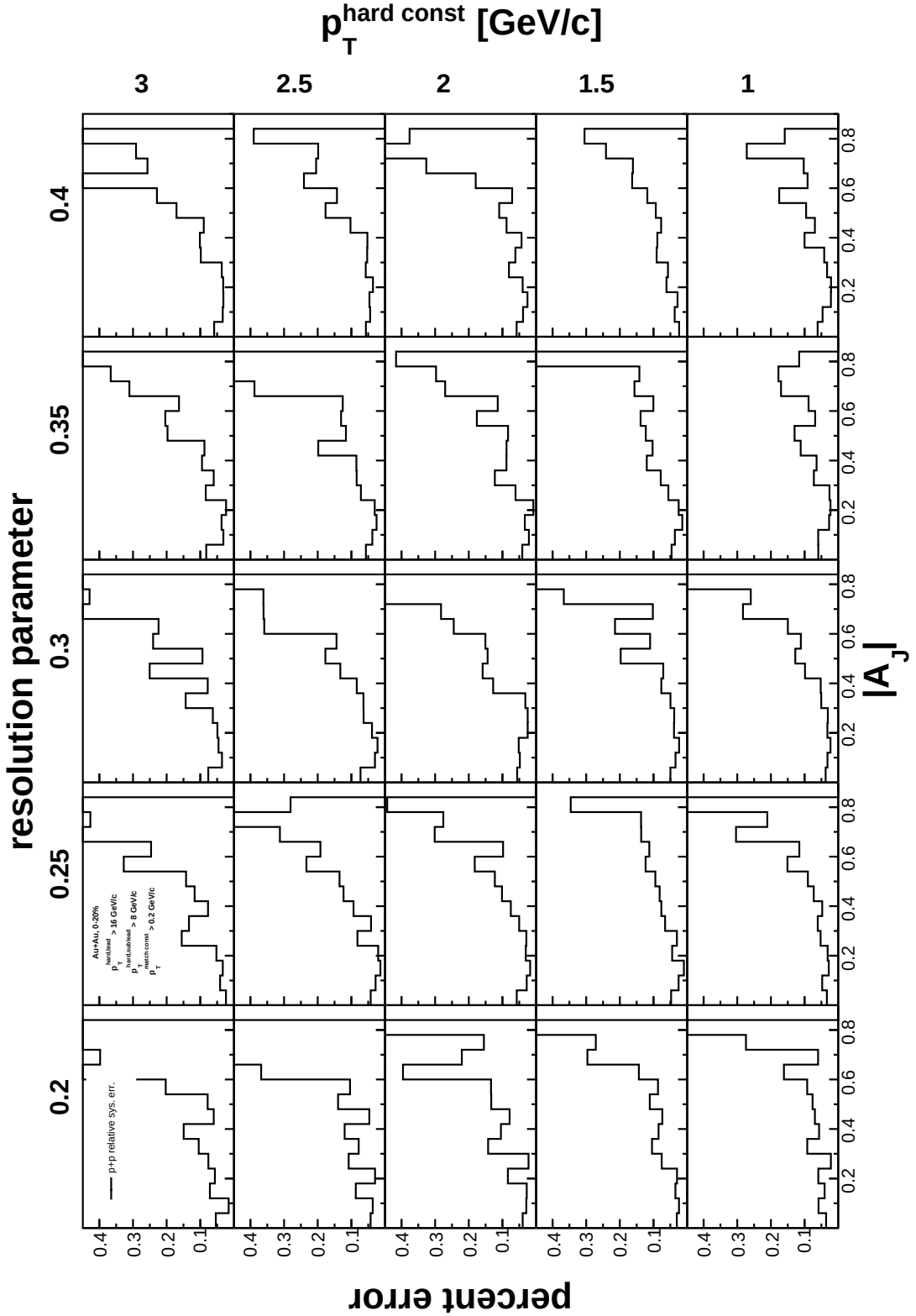

Figure F.26: Relative systematic errors for all di-jet definitions varying $p_{\mathrm{T}}^{\mathrm{const}}$ and R for embedded $p+p$ matched di-jets in the radial scan.

BIBLIOGRAPHY

[1] S. Bethke. Experimental tests of asymptotic freedom. *Prog. Part. Nucl. Phys.*, 58:351–386, 2007.

[2] D. J. Gross and F. Wilczek. Ultraviolet Behavior of Nonabelian Gauge Theories. *Phys. Rev. Lett.*, 30:1343–1346, 1973. [,271(1973)].

[3] H. D. Politzer. Reliable Perturbative Results for Strong Interactions? *Phys. Rev. Lett.*, 30:1346–1349, 1973. [,274(1973)].

[4] M. Breidenbach, J. I. Friedman, H. W. Kendall, E. D. Bloom, D. H. Coward, H. C. DeStaebler, J. Drees, L. W. Mo, and R. E. Taylor. Observed Behavior of Highly Inelastic electron-Proton Scattering. *Phys. Rev. Lett.*, 23:935–939, 1969.

[5] S. Durr et al. Ab-Initio Determination of Light Hadron Masses. *Science*, 322:1224–1227, 2008.

[6] P. Petreczky. Lattice QCD at non-zero temperature. *J. Phys.*, G39:093002, 2012.

[7] STAR Collaboration. Studying the phase diagram of qcd matter at rhic. https://drupal.star.bnl.gov/STAR/system/files/BES_WPII_ver6.9_Cover.pdf, 2014. Accessed June 2019.

[8] A. Bazavov et al. Equation of state and QCD transition at finite temperature. *Phys. Rev.*, D80:014504, 2009.

[9] B. I. Abelev et al. Longitudinal double-spin asymmetry and cross section for inclusive jet production in polarized proton collisions at s**(1/2) = 200-GeV. *Phys. Rev. Lett.*, 97:252001, 2006.

[10] V. N. Gribov and L. N. Lipatov. Deep inelastic e p scattering in perturbation theory. *Sov. J. Nucl. Phys.*, 15:438–450, 1972. [Yad. Fiz.15,781(1972)].

[11] G. Altarelli and G. Parisi. Asymptotic Freedom in Parton Language. *Nucl. Phys.*, B126:298–318, 1977.

[12] Y. L. Dokshitzer. Calculation of the Structure Functions for Deep Inelastic Scattering and e+ e- Annihilation by Perturbation Theory in Quantum Chromodynamics. *Sov. Phys. JETP*, 46:641–653, 1977. [Zh. Eksp. Teor. Fiz.73,1216(1977)].

[13] F. Karsch, E. Laermann, and A. Peikert. Quark mass and flavor dependence of the QCD phase transition. *Nucl. Phys.*, B605:579–599, 2001.

[14] U. W. Heinz and M. Jacob. Evidence for a new state of matter: An Assessment of the results from the CERN lead beam program. 2000. nucl-th/0002042.

[15] B. B. Back et al. The PHOBOS perspective on discoveries at RHIC. *Nucl. Phys.*, A757:28–101, 2005.

[16] I. Arsene et al. Quark gluon plasma and color glass condensate at RHIC? The Perspective from the BRAHMS experiment. *Nucl. Phys.*, A757:1–27, 2005.

[17] K. Adcox et al. Formation of dense partonic matter in relativistic nucleus-nucleus collisions at RHIC: Experimental evaluation by the PHENIX collaboration. *Nucl. Phys.*, A757:184–283, 2005.

[18] J. Adams et al. Experimental and theoretical challenges in the search for the quark gluon plasma: The STAR Collaboration's critical assessment of the evidence from RHIC collisions. *Nucl. Phys.*, A757:102–183, 2005.

[19] R. Snellings. Elliptic Flow: A Brief Review. *New J. Phys.*, 13:055008, 2011.

[20] A. Bialas, M. Bleszynski, and W. Czyz. Multiplicity Distributions in Nucleus-Nucleus Collisions at High-Energies. *Nucl. Phys.*, B111:461–476, 1976.

[21] B. Alver, M. Baker, C. Loizides, and P. Steinberg. The PHOBOS Glauber Monte Carlo. 2008. arXiv:0805.4411 [nucl-ex].

[22] R. J. Glauber. Cross sections in deuterium at high energies. *Phys. Rev.*, 100:242–248, Oct 1955.

[23] V. Franco and R. J. Glauber. High-energy deuteron cross sections. *Phys. Rev.*, 142:1195–1214, Feb 1966.

[24] M. L. Miller, K. Reygers, S. J. Sanders, and P. Steinberg. Glauber modeling in high energy nuclear collisions. *Ann. Rev. Nucl. Part. Sci.*, 57:205–243, 2007.

[25] W. Broniowski, P. Bozek, and M. Rybczynski. Fluctuating initial conditions in heavy-ion collisions from the Glauber approach. *Phys. Rev.*, C76:054905, 2007.

[26] B. Alver et al. System size, energy, pseudorapidity, and centrality dependence of elliptic flow. *Phys. Rev. Lett.*, 98:242302, 2007.

[27] G. Qin, H. Petersen, S. A. Bass, and B. Muller. Translation of collision geometry fluctuations into momentum anisotropies in relativistic heavy-ion collisions. *Phys. Rev.*, C82:064903, 2010.

[28] I. G. Bearden et al. Nuclear stopping in Au + Au collisions at s(NN)**(1/2) = 200-GeV. *Phys. Rev. Lett.*, 93:102301, 2004.

[29] J. D. Bjorken. Highly relativistic nucleus-nucleus collisions: The central rapidity region. *Phys. Rev. D*, 27:140–151, Jan 1983.

[30] S. S. Adler et al. Systematic studies of the centrality and s(NN)**(1/2) dependence of the d E(T) / d eta and d (N(ch) / d eta in heavy ion collisions at mid-rapidity. *Phys. Rev.*, C71:034908, 2005. [Erratum: Phys. Rev.C71,049901(2005)].

[31] F. Karsch. Lattice results on qcd thermodynamics. *Nuclear Physics A*, 698(1):199 – 208, 2002. 15th Int. Conf. on Ultra-Relativistic Nucleus-Nucleus Collisions (Quark Matter 2001).

[32] P. F. Kolb and U. W. Heinz. Hydrodynamic description of ultrarelativistic heavy ion collisions. pages 634–714, 2003.

[33] D. A. Teaney. Viscous Hydrodynamics and the Quark Gluon Plasma. In Rudolph C. Hwa and Xin-Nian Wang, editors, *Quark-gluon plasma 4*, pages 207–266. 2010.

[34] M. Luzum and P. Romatschke. Conformal relativistic viscous hydrodynamics: Applications to rhic results at $\sqrt{s_{NN}} = 200$ gev. *Phys. Rev. C*, 78:034915, Sep 2008.

[35] J. Adams et al. Identified particle distributions in pp and Au+Au collisions at s(NN)**(1/2) = 200 GeV. *Phys. Rev. Lett.*, 92:112301, 2004.

[36] S. A. Voloshin, A. M. Poskanzer, and R. Snellings. Collective phenomena in non-central nuclear collisions. *Landolt-Bornstein*, 23:293–333, 2010.

[37] A. M. Poskanzer and S. A. Voloshin. Methods for analyzing anisotropic flow in relativistic nuclear collisions. *Phys. Rev. C*, 58:1671–1678, Sep 1998.

[38] L. Adamczyk et al. Azimuthal anisotropy in U+U and Au+Au collisions at RHIC. *Phys. Rev. Lett.*, 115(22):222301, 2015.

[39] J. Adams et al. Azimuthal anisotropy in Au+Au collisions at s(NN)**(1/2) = 200-GeV. *Phys. Rev.*, C72:014904, 2005.

[40] E. Levin. Landau-Pomeranchuk-Migdal effect for nuclear matter in QCD. *Phys. Lett.*, B380:399–408, 1996.

[41] S. Sarkar, H. Satz, and B. Sinha. The physics of the quark-gluon plasma. *Lect. Notes Phys.*, 785:pp.1–369, 2010.

[42] G. Sterman and S. Weinberg. Jets from quantum chromodynamics. *Phys. Rev. Lett.*, 39:1436–1439, Dec 1977.

[43] M. Cacciari, G. P. Salam, and G. Soyez. The Catchment Area of Jets. *JHEP*, 04:005, 2008.

[44] S. S. Adler et al. Common suppression pattern of η and π^0 mesons at high transverse momentum in Au + Au collisions at $\sqrt{s_{NN}} = 200$ GeV. *Phys. Rev. Lett.*, 96:202301, May 2006.

[45] J. Adams et al. Evidence from d + Au measurements for final-state suppression of high-p_T hadrons in Au + Au collisions at rhic. *Phys. Rev. Lett.*, 91:072304, Aug 2003.

[46] D. G. d'Enterria. QCD hard scattering results from PHENIX at RHIC. In *Structure and dynamics of elementary matter. Proceedings, NATO Advanced Study Institute, Camyuva-Kemer, Turkey, September 22-October 2, 2003*, pages 61–69, 2004.

[47] B. B. Back et al. Centrality dependence of charged-hadron transverse-momentum spectra in $d+$Au collisions at $\sqrt{s_{NN}} = 200$ GeV. *Phys. Rev. Lett.*, 91:072302, Aug 2003.

[48] J. Adams et al. Transverse momentum and collision energy dependence of high p(T) hadron suppression in Au+Au collisions at ultrarelativistic energies. *Phys. Rev. Lett.*, 91:172302, 2003.

[49] S. S. Adler et al. Absence of suppression in particle production at large transverse momentum in S(NN)**(1/2) = 200-GeV d + Au collisions. *Phys. Rev. Lett.*, 91:072303, 2003.

[50] Artistic render of a parton shower. https://i.stack.imgur.com/MBzaD.png. Accessed: 2019-10-09.

[51] S. Catani, Y. L. Dokshitzer, M. H. Seymour, and B. R. Webber. Longitudinally invariant K_t clustering algorithms for hadron hadron collisions. *Nucl. Phys.*, B406:187–224, 1993.

[52] S. D. Ellis and D. E. Soper. Successive combination jet algorithm for hadron collisions. *Phys. Rev.*, D48:3160–3166, 1993.

[53] Y. L. Dokshitzer, G. D. Leder, S. Moretti, and B. R. Webber. Better jet clustering algorithms. *JHEP*, 08:001, 1997.

[54] M. Wobisch and T. Wengler. Hadronization corrections to jet cross-sections in deep inelastic scattering. In *Monte Carlo generators for HERA physics. Proceedings, Workshop, Hamburg, Germany, 1998-1999*, pages 270–279, 1998.

[55] M. Cacciari, G. P. Salam, and G. Soyez. The anti-k_t jet clustering algorithm. *JHEP*, 04:063, 2008.

[56] M. Cacciari and G. P. Salam. Dispelling the N^3 myth for the k_t jet-finder. *Phys. Lett.*, B641:57–61, 2006.

[57] M. Cacciari, G. P. Salam, and G. Soyez. FastJet User Manual. *Eur. Phys. J.*, C72:1896, 2012.

[58] L. Adamczyk et al. Jet-Hadron Correlations in $\sqrt{s_{NN}} = 200$ GeV $p + p$ and Central $Au + Au$ Collisions. *Phys. Rev. Lett.*, 112(12):122301, 2014.

[59] S. Chatrchyan et al. Observation and studies of jet quenching in PbPb collisions at nucleon-nucleon center-of-mass energy = 2.76 TeV. *Phys. Rev.*, C84:024906, 2011.

[60] G. Aad et al. Observation of a Centrality-Dependent Dijet Asymmetry in Lead-Lead Collisions at $\sqrt{s_{NN}} = 2.77$ TeV with the ATLAS Detector at the LHC. *Phys. Rev. Lett.*, 105:252303, 2010.

[61] L. Adamczyk et al. Dijet imbalance measurements in $Au + Au$ and pp collisions at $\sqrt{s_{NN}} = 200$ GeV at STAR. *Phys. Rev. Lett.*, 119(6):062301, 2017.

[62] H. Hahn et al. The RHIC design overview. *Nucl. Instrum. Meth.*, A499:245–263, 2003.

[63] RHIC Collider-Accelerator Department. Configuration manual. https://www.bnl.gov/cad/accelerator/docs/pdf/RHICConfManual.pdf, 2006.

[64] A. Pikin et al. RHIC EBIS: basics of design and status of commissioning. *Journal of Instrumentation*, 5(09):C09003–C09003, sep 2010.

[65] K. H. Ackermann et al. STAR detector overview. *Nucl. Instrum. Meth.*, A499:624–632, 2003.

[66] F. Bergsma et al. The star detector magnet subsystem. *Nuclear Instruments and Methods in Physics Research Section A: Accelerators, Spectrometers, Detectors and Associated Equipment*, 499(2):633 – 639, 2003. The Relativistic Heavy Ion Collider Project: RHIC and its Detectors.

[67] M. Anderson et al. The Star time projection chamber: A Unique tool for studying high multiplicity events at RHIC. *Nucl. Instrum. Meth.*, A499:659–678, 2003.

[68] H. Bichsel. A method to improve tracking and particle identification in TPCs and silicon detectors. *Nucl. Instrum. Meth.*, A562:154–197, 2006.

[69] M. Anderson et al. A Readout system for the STAR time projection chamber. *Nucl. Instrum. Meth.*, A499:679–691, 2003.

[70] L. Kotchenda et al. STAR TPC gas system. *Nucl. Instrum. Meth.*, A499:703–712, 2003.

[71] F. Shen et al. MWPC prototyping and performance test for the STAR inner TPC upgrade. *Nucl. Instrum. Meth.*, A896:90–95, 2018.

[72] M. Beddo et al. The STAR barrel electromagnetic calorimeter. *Nucl. Instrum. Meth.*, A499:725–739, 2003.

[73] C. Adler et al. The RHIC zero degree calorimeter. *Nucl. Instrum. Meth.*, A470:488–499, 2001.

[74] W. J. Llope et al. The STAR Vertex Position Detector. *Nucl. Instrum. Meth.*, A759:23–28, 2014.

[75] J. Kiryluk. Local polarimetry for proton beams with the STAR beam beam counters. In *Spin physics. Polarized electron sources and polarimeters. Proceedings, 16th International Symposium, SPIN 2004, Trieste, Italy, October 10-16, 2004, and Workshop, PESP 2004, Mainz, Germany, October 7-9, 2004*, pages 718–721, 2005.

[76] R. Bellwied et al. The star silicon vertex tracker: A large area silicon drift detector. *Nuclear Instruments and Methods in Physics Research Section A: Accelerators, Spectrometers, Detectors and Associated Equipment*, 499(2):640 – 651, 2003. The Relativistic Heavy Ion Collider Project: RHIC and its Detectors.

[77] Y. Zhang, J. Bouchet, X. Dong, Margetis S., and H. G. Ritter. Study of bottom production with the STAR heavy flavor tracker. *Journal of Physics G: Nuclear and Particle Physics*, 41(2):025103, jan 2014.

[78] W. J. Llope et al. The tofp/pvpd time-of-flight system for star. *Nuclear Instruments and Methods in Physics Research Section A: Accelerators, Spectrometers, Detectors and Associated Equipment*, 522(3):252 – 273, 2004.

[79] C. Yang et al. Calibration and performance of the STAR Muon Telescope Detector using cosmic rays. *Nucl. Instrum. Meth.*, A762:1–6, 2014.

[80] K. H. Ackermann et al. The Forward time projection chamber (FTPC) in STAR. *Nucl. Instrum. Meth.*, A499:713–719, 2003.

[81] J. Dunlop. 2007 run 7 trigger faq. https://www.star.bnl.gov/protected/common/common2007/trigger2007/triggers2007.html, 2007.

[82] J. Dunlop. 2006 run 6 trigger faq. https://www.star.bnl.gov/protected/common/common2006/trigger2006/triggers2006.html, 2006.

[83] R. Brun et al. Geant 3 user's guide. https://cds.cern.ch/record/1119728?ln=en, 1987.

[84] A. Ohlson. Investigating parton energy loss in the quark-gluon plasma with jet-hadron correlations and jet azimuthal anisotropy at star. https://drupal.star.bnl.gov/STAR/files/aohlson_thesis.pdf, 2013.

[85] L. Adamczyk et al. Precision measurement of the longitudinal double-spin asymmetry for inclusive jet production in polarized proton collisions at $\sqrt{s} = 200$ GeV. *Phys. Rev. Lett.*, 115:092002, Aug 2015.

[86] STAR Collaboration internal documentation. Digging for production changes after sl16d. https://drupal.star.bnl.gov/STAR/blog/genevb/digging-production-changes-after-sl16d, 2018. Accessed September 2019.

[87] C. Adler et al. Elliptic flow from two and four particle correlations in Au+Au collisions at s(NN)**(1/2) = 130-GeV. *Phys. Rev.*, C66:034904, 2002.

[88] ROOT Authors. Root kolmogorov-smirnov test. https://root.cern.ch/doc/master/classTH1.html#aeadcf087afe6ba203bcde124cfabbee4. Accessed September 2019.

[89] NIST. Kolmogorov-smirnov test. https://www.itl.nist.gov/div898/handbook/eda/section3/eda35g.htm. Accessed September 2019.

[90] T. Renk. Biased showers: A common conceptual framework for the interpretation of high-P_T observables in heavy-ion collisions. *Phys. Rev.*, C88(5):054902, 2013.

[91] L. Adamczyk et al. Measurements of jet quenching with semi-inclusive hadron+jet distributions in Au+Au collisions at $\sqrt{s_{NN}}$ = 200 GeV. *Phys. Rev.*, C96(2):024905, 2017.

[92] H. Agakishiev et al. Studies of di-jet survival and surface emission bias in Au+Au collisions via angular correlations with respect to back-to-back leading hadrons. *Phys. Rev.*, C83:061901, 2011.

[93] L. Adamczyk et al. Experimental studies of di-jets in Au + Au collisions using angular correlations with respect to back-to-back leading hadrons. *Phys. Rev.*, C87(4):044903, 2013.

[94] K. C. Zapp. JEWEL 2.0.0: directions for use. *Eur. Phys. J.*, C74(2):2762, 2014.

[95] J. H. Putschke et al. The JETSCAPE framework. 2019. arXiv:1903.07706 [nucl-th].

[96] M. Verweij. Novel tools and jet observables for jet physics in heavy-ion collisions. Hard Probes 2018, 2018.

[97] A. J. Larkoski, S. Marzani, G. Soyez, and J. Thaler. Soft Drop. *JHEP*, 05:146, 2014.

[98] R. Kunnawalkam Elayavalli. Jet sub-structure and parton shower evolution in p+p and Au+Au collisions at STAR. In *13th International Workshop on High-pT Physics in the RHIC/LHC Era (HPT 2019) Knoxville, TN, USA, March 19-22, 2019*, 2019.

[99] M. Verweij. Medium modification of jet structure (rhic + lhc). https://indico.cern.ch/event/433345/contributions/2321612/, 2017. Quark Matter 2017.

[100] R. J. Glauber. *Lectures in Theoretical Physics*, 1:315, 1959.

[101] W. Czyż and L. Leśniak. Elastic scattering of very high energy particles from nuclei. *Physics Letters B*, 24(5):227 – 229, 1967.

[102] V. Franco and R. J. Glauber. High-energy deuteron cross sections. *Phys. Rev.*, 142:1195–1214, Feb 1966.

[103] A. Białłas, M. Bleszyński, and W. Czyż. Multiplicity distributions in nucleus-nucleus collisions at high energies. *Nuclear Physics B*, 111(3):461 – 476, 1976.

[104] B. B. Back et al. Collision geometry scaling of Au+Au pseudorapidity density from s(NN)**(1/2) = 19.6-GeV to 200-GeV. *Phys. Rev.*, C70:021902, 2004.

ABSTRACT

JET GEOMETRY ENGINEERING VIA DI-JET IMBALANCE MEASUREMENTS AT RHIC IN STAR

by

NICHOLAS ELSEY

December 2019

Advisor: Dr. Joern Putschke

Major: Physics

Degree: Doctor of Philosophy

Ultra-relativistic heavy ion collisions produced at the Relativistic Heavy Ion Collider (RHIC) and the Large Hadron Collider (LHC) produce a new state of matter of deconfined quarks and gluons (partons) called the quark-gluon plasma (QGP). This plasma of deconfined but strongly coupled partons is believed to have been the primary state of matter in the universe up to a few milliseconds after the Big Bang. High energy partons produced in hard scatterings early in the collision can be used to probe the entire lifetime of the QGP. These partons propagate through and interact with the QGP before fragmenting into collimated sprays of hadrons called jets. Modification of these jets due to interaction with the QGP, also known as jet quenching, can provide insight into the interactions between the colored probe and the strongly interacting medium.

Two analyses utilizing specific "hard-core" di-jet events identified at the STAR detector at RHIC are presented, using Au+Au and $p+p$ collisions at $\sqrt{s_{NN}} = 200$ GeV.

In the di-jet hadron correlations, charged hadron yield with respect to the reconstructed jet axes allow for measurement of the redistribution of energy within the constituents of a jet due to interactions with the medium. It is shown that these "hard-core" di-jets are significantly less modified by the medium than what is seen in the inclusive jet population, with relatively vacuum-like widths and constituent yields.

In the differential di-jet imbalance measurement, the di-jet definition used to identify

hard-core di-jets is systematically varied in two parameters: the jet resolution parameter, R, and the hard constituent transverse momentum threshold, $p_{\mathrm{T}}^{\mathrm{const}}$, which controls the selection of jets with harder or softer fragmentation patterns. It is found that the amount of modification experienced by the di-jet population is sensitive to the selection of these two parameters. The ability to control the amount of modification in a jet sample in a systematic manner suggests the possibility of *Jet Geometry Engineering*, the ability to control the path length of a jet in the QGP, which would allow for more direct study of the path length dependence of partonic energy loss.

AUTOBIOGRAPHICAL STATEMENT

Name: Nick Elsey

Education:
B.S. Physics, Wayne State University, Detroit, MI, 2014

Teaching:
TA, Introductory Physics Laboratory, Wayne State University, 2015
TA, Computational Physics, Wayne State University, 2016-2017

Publications:
Elsey, N.: Systematic Studies of Di-jet Imbalance Measurements in STAR, *Hard Probes 2018: International Conference on Hard & Electromagnetic Probes of High-Energy Nuclear Collisions*, PoS Hard Probes 2018, (2018) 087

(For a full list, see https://inspirehep.net/search?p=exactauthor%3AN.Elsey.1)

Presented Talks:

Di-jet Hadron Correlations in Central Au+Au Collisions at $\sqrt{s_{NN}} = 200$ *GeV at STAR*, Fall Meeting of the APS Division of Nuclear Physics, Pittsburgh, Pennsylvania.

Systematic Studies of Di-jet Imbalance Measurements in STAR, Hard Probes, Aix-Les-Bains, Savoie, France, 2018. (PoS Hard Probes 2018, (2018) 087).

Systematic Studies of Di-jet Imbalance Measurements in STAR, High-p_{T} Workshop, Knoxville, TN, 2019.

Presented Posters:

Di-jet Hadron Correlations in Central Au+Au Collisions at $\sqrt{s_{NN}} = 200$ *GeV at STAR*, Quark Matter, Chicago, Il, 2017.